

**AD-A244 050**



①

AFIT/GA/ENY/91D-13

**EFFECT OF NONUNIFORM ENTRANCE FLOW PROFILE  
ON HYPERSONIC NOZZLE PITCHING MOMENT**

**THESIS**

**Sandra L. Snelling**

**Captain, USAF**

**AFIT/GA/ENY/91D-13**

**DTIC  
ELECTE  
JAN 8 1992  
S B D**

**92-00037**



Approved for public release; distribution unlimited

**92 1 009**

AFIT/GA/ENY/91D-13

EFFECT OF NONUNIFORM ENTRANCE FLOW PROFILE  
ON HYPERSONIC NOZZLE PITCHING MOMENT

THESIS

Presented to the Faculty of the School of Engineering  
of the Air Force Institute of Technology

Air University

In Partial Fulfillment of the  
Requirements for the Degree of  
Master of Science in Aeronautical Engineering

Sandra L. Snelling, B.A.E.

Captain, USAF

December, 1991

Approved for public release; distribution unlimited

### Acknowledgements

I would like to thank my advisor, Lt Col Gerald Hasen, for his patience and guidance during all my troubles. Also, many thanks to Capt John Doty for being a "second advisor" in many respects, including the long office lectures on nonuniformities. I would also like to thank the members of Young Adults at Zion for their support and encouragement even though they think I'm a geek just because they have no idea what I'm talking about. Finally, I would like to thank the members of Wednesday Night Star Trek and Pinochle Group (WNSTPG) for all their love and support and the continuing sanity checks. It's been real!



Accession For	
NTIS GDA&I	<input checked="checked" type="checkbox"/>
DTIC TAB	<input type="checkbox"/>
Unannounced	<input type="checkbox"/>
Justification	
By	
Distribution/	
Availability Codes	
Dist	Avail and/or Special
A-1	

## Table of Contents

Acknowledgements . . . . .	ii
List of Figures . . . . .	v
List of Tables . . . . .	x
List of Symbols . . . . .	xi
Abstract . . . . .	xv
I. Introduction . . . . .	1-1
1.1 Purpose . . . . .	1-1
1.2 Approach . . . . .	1-2
II. Theory . . . . .	2-1
2.1 Mean Flow Equations . . . . .	2-1
2.2 Turbulence Model . . . . .	2-2
2.3 Supplemental Equations . . . . .	2-4
2.4 Chemical Kinetics . . . . .	2-6
2.5 Nonuniform Flow Averaging . . . . .	2-9
III. Methodology . . . . .	3-1
3.1 PNS Code Description . . . . .	3-1
3.2 Hypersonic Nozzle . . . . .	3-4
3.3 Freestream Conditions . . . . .	3-5
3.4 External Flow Conditions . . . . .	3-6
3.5 Nozzle Inlet Conditions . . . . .	3-7
IV. Results . . . . .	4-1
4.1 Case Summary . . . . .	4-1
4.2 Grid Refinement . . . . .	4-1
4.3 Frozen Versus Finite Rate . . . . .	4-3
4.4 Isolated Nozzle Results . . . . .	4-4
4.5 Isolated Versus Combined Nozzle Plots . . . . .	4-6
4.6 Combined Nozzle . . . . .	4-6
4.7 Thrust and Moment . . . . .	4-8
V. Conclusions/Recommendations . . . . .	5-1
5.1 Conclusions . . . . .	5-1
5.2 Recommendations . . . . .	5-5
Bibliography . . . . .	BIB-1
Appendix A. Line Plots . . . . .	A-1
A.1 Frozen vs. Finite Rate Plots . . . . .	A-1
A.1.1 Isolated Nozzle . . . . .	A-1
A.1.2 Combined Nozzle . . . . .	A-4
A.2 Isolated Nozzle vs. Combined Nozzle Plots . . . . .	A-7
A.2.1 Uniform, Finite Rate Flow . . . . .	A-7

A.2.2	Nonuniform, Finite Rate Flow . . . . .	A-10
A.3	Uniform vs. Nonuniform Plots . . . . .	A-13
A.3.1	Finite Rate, Isolated Nozzle . . . . .	A-13
A.3.2	Finite Rate, Combined Nozzle . . . . .	A-16
A.4	Grid Resolution Plots . . . . .	A-19
A.4.1	Uniform Flow Plots . . . . .	A-19
A.4.2	Nonuniform Flow Plots . . . . .	A-21
Appendix B.	Contour Plots . . . . .	B-1
B.1	Isolated Nozzle Plots . . . . .	B-1
B.2	Combined Nozzle Plots . . . . .	B-3
Appendix C.	Input Data . . . . .	C-1
Vita	. . . . .	BIB-3

## *List of Figures*

Figure	Page
1.1. Typical Hypersonic Vehicle . . . . .	1-4
1.2. Expanded View of Nozzle and Cowl Section . . . . .	1-4
2.1. Compressibility Correction Factor for $k\epsilon$ Turbulence Models . . . . .	2-12
3.1. Nozzle Geometry for all Cases . . . . .	3-10
3.2. Pressure Profile Improvements in Vicinity of Captured Shock Using Harten-Zwas Self-Adjusting Damping Correction (13:25) . . . . .	3-11
3.3. Nonuniform Mach Number Profile . . . . .	3-12
3.4. Nonuniform Static Temperature Profile . . . . .	3-12
3.5. Nonuniform Stagnation Pressure Profile . . . . .	3-13
3.6. Nonuniform Stagnation Temperature Profile . . . . .	3-13
3.7. Nonuniform Velocity Entrance Profile . . . . .	3-14
4.1. Nozzle Wall Temperatures for Grid and $(Y/h)_{\max}$ Changes for Uniform, Finite Rate Flow in the Combined Nozzle . . . . .	4-12
4.2. Nozzle Wall Temperatures for Grid and $(Y/h)_{\max}$ Changes for Nonuniform, Finite Rate Flow in the Combined Nozzle . . . . .	4-13
4.3. Nozzle Wall Pressures for Frozen and Finite Rate Flow in the Isolated Nozzle . . . . .	4-13
4.4. Nozzle Wall Pressures for Frozen and Finite Rate Flow in the Combined Nozzle . . . . .	4-14
4.5. Nozzle Wall Pressures for Uniform and Nonuniform Flow for the Finite Rate, Isolated Nozzle . . . . .	4-14
4.6. Cowl Wall Pressures for Uniform and Nonuniform Flow for the Finite Rate, Isolated Nozzle . . . . .	4-15
4.7. Pressure Contour Plot (atm) for Uniform, Finite Rate Flow in an Isolated Nozzle . . . . .	4-15

4.8.	Pressure Contour Plot (atm) for Nonuniform, Finite Rate Flow in an Isolated Nozzle . . . . .	4-16
4.9.	Nozzle Wall Temperature for Finite Rate, Uniform Flow for the Isolated and Combined Nozzles . . . . .	4-16
4.10.	Nozzle Wall X-Component Velocities for Finite Rate, Uniform Flow for the Isolated and Combined Nozzles . . . . .	4-17
4.11.	Nozzle Wall Temperatures for Finite Rate, Nonuniform Flow for the Isolated and Combined Nozzles . . . . .	4-17
4.12.	Nozzle Wall X-Component Velocities for Finite Rate, Nonuniform Flow for the Isolated and Combined Nozzles . . . . .	4-18
4.13.	Nozzle Wall Pressures for Uniform and Nonuniform Flow for the Finite Rate, Combined Nozzle . . . . .	4-18
4.14.	Cowl Wall Pressures for Uniform and Nonuniform Flow for the Finite Rate, Combined Nozzle . . . . .	4-19
4.15.	Pressure Contour Plot (atm) for Uniform, Finite Rate Flow in a Combined Nozzle . . . . .	4-19
4.16.	Pressure Contour Plot (atm) for Nonuniform, Finite Rate Flow in a Combined Nozzle . . . . .	4-20
4.17.	Cumulative Thrust Produced in the Finite Rate Isolated Nozzle for Uniform and Nonuniform Flow . . . . .	4-20
4.18.	Cumulative Moment Produced in the Finite Rate, Isolated Nozzle for Uniform and Nonuniform Flow . . . . .	4-21
4.19.	Cumulative Thrust for the Finite Rate, Combined Nozzle for Uniform and Nonuniform Flow . . . . .	4-21
4.20.	Cumulative Thrust for Nonuniform Finite Rate Flow for the Isolated and Combined Nozzles . . . . .	4-22
4.21.	Cumulative Moment for the Finite Rate, Combined Nozzle for Uniform and Nonuniform Flow . . . . .	4-22
4.22.	Cumulative Moment for Nonuniform, Finite Rate Flow for the Isolated and Combined Nozzle . . . . .	4-23
A.1.	Nozzle Wall Pressures for Frozen and Finite Rate, Uniform Flow in the Isolated Nozzle . . . . .	A-1
A.2.	Cowl Wall Pressures for Frozen and Finite Rate, Uniform Flow in an Isolated Nozzle . . . . .	A-1
A.3.	Nozzle Wall Temperatures for Frozen and Finite Rate, Uniform Flow in the Isolated Nozzle . . . . .	A-2

A.4.	Nozzle Wall X-Component Velocities for Frozen and Finite Rate, Uniform Flow in the Isolated Nozzle . . .	A-2
A.5.	Nozzle Wall Y-Component Velocities for Frozen and Finite Rate, Uniform Flow in the Isolated Nozzle . . .	A-3
A.6.	Nozzle Wall Mach Numbers for Frozen and Finite Rate, Uniform Flow in the Isolated Nozzle . . . . .	A-3
A.7.	Nozzle Wall Pressures for Frozen and Finite Rate, Nonuniform Flow in the Combined Nozzle . . . . .	A-4
A.8.	Cowl Wall Pressures for Frozen and Finite Rate, Nonuniform Flow in the Combined Nozzle . . . . .	A-4
A.9.	Nozzle Wall Temperatures for Frozen and Finite Rate, Nonuniform Flow in the Combined Nozzle . . . . .	A-5
A.10.	Nozzle Wall X-Component Velocities for Frozen and Finite Rate, Nonuniform Flow in the Combined Nozzle . .	A-5
A.11.	Nozzle Wall Y-Component Velocities for Frozen and Finite Rate, Nonuniform Flow in the Combined Nozzle . .	A-6
A.12.	Nozzle Wall Mach Numbers for Frozen and Finite Rate, Nonuniform Flow in the Combined Nozzle . . . . .	A-6
A.13.	Nozzle Wall Pressures for Nonuniform, Finite Rate Flow for the Isolated and Combined Nozzles . . . . .	A-7
A.14.	Cowl Wall Pressures for Finite Rate, Uniform Flow for the Isolated and Combined Nozzles . . . . .	A-7
A.15.	Nozzle Wall Temperatures for Finite Rate, Uniform Flow for the Isolated and Combined Nozzles . . . . .	A-8
A.16.	Nozzle Wall X-Component Velocities for Finite Rate, Uniform Flow for the Isolated and Combined Nozzles . .	A-8
A.17.	Nozzle Wall Y-Component Velocities for Finite Rate, Uniform Flow for the Isolated and Combined Nozzles . .	A-9
A.18.	Nozzle Wall Mach Numbers for Finite Rate, Uniform Flow for the Isolated and Combined Nozzles . . . . .	A-9
A.19.	Nozzle Wall Pressures for Finite Rate, Nonuniform Flow for the Isolated and Combined Nozzles . . . . .	A-10
A.20.	Cowl Wall Pressures for Finite Rate, Nonuniform Flow for the Isolated and Combined Nozzles . . . . .	A-10
A.21.	Nozzle Wall Temperatures for Finite Rate, Nonuniform Flow for the Isolated and Combined Nozzles . . . . .	A-11



A.22.	Nozzle Wall X-Component Velocities for Finite Rate, Nonuniform Flow for the Isolated and Combined Nozzles .	A-11
A.23.	Nozzle Wall Y-Component Velocities for Finite Rate, Nonuniform Flow for the Isolated and Combined Nozzles .	A-12
A.24.	Nozzle Wall Mach Numbers for Finite Rate, Nonuniform Flow for the Isolated and Combined Nozzles . . . . .	A-12
A.25.	Nozzle Wall Pressures for Uniform and Nonuniform Flow for the Finite Rate, Isolated Nozzle . . . . .	A-13
A.26.	Cowl Wall Pressures for Uniform and Nonuniform Flow for the Finite Rate, Isolated Nozzle . . . . .	A-13
A.27.	Nozzle Wall Temperatures for Uniform and Nonuniform Flow for the Finite Rate Isolated Nozzle . . . . .	A-14
A.28.	Nozzle Wall X-Component Velocities for Uniform and Nonuniform Flow for the Finite Rate, Isolated Nozzle .	A-14
A.29.	Nozzle Wall Y-Component Velocities for Uniform and Nonuniform Flow for the Finite Rate, Isolated Nozzle .	A-15
A.30.	Nozzle Wall Mach Numbers for Uniform and Nonuniform Flow for the Finite Rate, Isolated Nozzle . . . . .	A-15
A.31.	Nozzle Wall Pressures for Uniform and Nonuniform Flow for the Finite Rate, Combined Nozzle . . . . .	A-16
A.32.	Cowl Wall Pressures for Uniform and Nonuniform Flow for the Finite Rate, Combined Nozzle . . . . .	A-16
A.33.	Nozzle Wall Temperatures for Uniform and Nonuniform Flow for the Finite Rate, Combined Nozzle . . . . .	A-17
A.34.	Nozzle Wall X-Component Velocities for Uniform and Nonuniform Flow for the Finite Rate, Combined Nozzle .	A-17
A.35.	Nozzle Wall Y-Component Velocities for Uniform and Nonuniform Flow for the Finite Rate, Combined Nozzle .	A-18
A.36.	Nozzle Wall Mach Numbers for Uniform and Nonuniform Flow for the Finite Rate, Combined Nozzle . . . . .	A-18
A.37.	Nozzle Wall Temperatures for Grid Changes for Uniform, Finite Rate Flow in the Combined Nozzle . . . . .	A-19
A.38.	Nozzle Wall Pressure for Grid Changes for Uniform, Finite Rate Flow in the Combined Nozzle . . . . .	A-19
A.39.	Nozzle Wall X-Component Velocity for Grid Changes for Uniform, Finite Rate Flow in the Combined Nozzle . . .	A-20

A.40.	Nozzle Wall Y-Component Velocity for Grid Changes for Uniform Flow, Finite Rate Flow in the Combined Nozzle . . . . .	A-20
A.41.	Nozzle Wall Mach Number for Grid Changes for Uniform, Finite Rate Flow in the Combined Nozzle . . . . .	A-21
A.42.	Nozzle Wall Temperature for Grid Changes for Nonuniform, Finite Rate Flow in the Combined Nozzle . . . . .	A-21
A.43.	Nozzle Wall Pressure for Grid Changes for Nonuniform, Finite Rate Flow in the Combined Nozzle . . . . .	A-22
A.44.	Nozzle Wall X-Component Velocity for Grid Changes for Nonuniform, Finite Rate Flow in the Combined Nozzle . . . . .	A-22
A.45.	Nozzle Wall Y-Component Velocity for Grid Changes for Nonuniform, Finite Rate Flow in the Combined Nozzle . . . . .	A-23
A.46.	Nozzle Wall Mach Number for Grid Changes for Nonuniform, Finite Rate Flow in the Combined Nozzle . . . . .	A-23
B.1.	Pressure Contour Plot (atm) for Uniform, Frozen Flow in an Isolated Nozzle . . . . .	B-1
B.2.	Pressure Contour Plot (atm) for Nonuniform, Frozen Flow in an Isolated Nozzle . . . . .	B-1
B.3.	Pressure Contour Plot (atm) for Uniform, Finite Rate Flow in an Isolated Nozzle . . . . .	B-2
B.4.	Pressure Contour Plot (atm) for Nonuniform, Finite Rate Flow in an Isolated Nozzle . . . . .	B-2
B.5.	Pressure Contour Plot (atm) for Uniform, Frozen Flow in a Combined Nozzle . . . . .	B-3
B.6.	Pressure Contour Plot (atm) for Nonuniform, Frozen Flow in a Combined Nozzle . . . . .	B-3
B.7.	Pressure Contour Plot (atm) for Uniform, Finite Rate Flow in a Combined Nozzle . . . . .	B-4
B.8.	Pressure Contour Plot (atm) for Nonuniform, Finite Rate Flow in a Combined Nozzle . . . . .	B-4

## *List of Tables*

Table	Page
1.1. Cases Used in Study . . . . .	1-3
3.1. Nozzle and Cowl Geometry Specifications . . . . .	3-5
3.2. Freestream Conditions . . . . .	3-6
3.3. External Flow Conditions . . . . .	3-7
3.4. Chemical Composition for External Flow . . . . .	3-7
3.5. Equivalent Uniform Flow Properties . . . . .	3-9
4.1. Cases Used in Study . . . . .	4-1
4.2. Total Thrust and Moment for All Cases . . . . .	4-12
C.1. SCHNOZ Variables which Change with Each Case and the Values Used for Each Case . . . . .	C-1
C.2. SCHNOZ Program Variables Which Remain Constant for This Study . . . . .	C-2
C.3. Property Profiles for Nonuniform Inlet . . . . .	C-3
C.4. Equilibrium Chemical Composition for Nonuniform Entrance Profile . . . . .	C-4

### List of Symbols

Symbol	Definition	Units
$a_f$	Frozen sound speed	ft/sec
$a_{\max}$	Local speed of sound at location of maximum value of turbulent kinetic energy	ft/sec
$A$	Inlet area	ft <sup>2</sup>
$B$	Activation energy per mole	cal/mole
$c_1$	Constant in forward rate coefficient equation	
$C_1$	Constant in turbulence equations	
$C_2$	Constant in turbulence equations	
$C_{pf}$	Frozen specific heat per unit mass	lbm <sup>-1</sup>
$C_{pi}$	Specific heat of species $i$ per unit mass	lbm <sup>-1</sup>
$C_\mu$	Constant in turbulent viscosity relation	
$\mathcal{E}$	Energy flow rate	lbm·ft <sup>2</sup> /sec <sup>3</sup>
$f$	Any flow property	
$\bar{f}$	w-averaged property	
$F_i$	Mass fraction of species $i$ divided by its molecular weight	lbm <sup>-1</sup>
$F_m$	Reciprocal of molecular weight	lbm <sup>-1</sup>
$h$	Static enthalpy of mixture; Nozzle inlet height	Btu/lbm in
$h_i$	Static enthalpy of species $i$	Btu/lbm
$H$	Total enthalpy	Btu/lbm
$i$	Species enumerator	

$k$	Turbulent kinetic energy; Boltzmann's constant	ft·lbf cal/°R
$k_b$	Reverse reaction rate constant	
$k_f$	Forward reaction rate constant	
$k_{max}$	Maximum value of turbulent kinetic energy at each axial station	ft·lbf
$K$	Correction factor in turbulent viscosity relation	
$K_c$	Equilibrium constant based on concentration	
$K_p$	Equilibrium constant based on partial pressure	
$l$	Turbulent length scale	ft
$m$	Mass of mixture	lbm
$\dot{m}$	Mass flow rate	lbm/sec
$m_i$	Molecular weight of species $i$	lbm/lb·mole
$M$	Mach number	
$\bar{M}$	Mass-averaged Mach number	
$M_r$	Characteristic Mach number of turbulence	
$n$	Number of species	
$p$	Static pressure	psia
$p'$	Corrected pressure	psia
$p_t$	Stagnation pressure	psia
$\bar{Pr}$	Sum of laminar Prandtl number and turbulent Prandtl number	
$Pr_l$	Laminar Prandtl number	
$Pr_t$	Turbulent Prandtl number	
$q_\infty$	Dynamic pressure	lbf/ft <sup>2</sup>
$R$	Gas constant of mixture	ft·lbf/lbm·°R

$R_o$	Universal gas constant	ft·lbf/mole·°R
$T$	Temperature	°R
$T_t$	Stagnation Temperature	°R
$u$	Axial component of velocity	ft/sec
$v$	Transverse component of velocity	ft/sec
$w$	Weighting function	
$W$	Mixture molecular weight	lbm/lb·mole
$x$	Streamwise spatial coordinate	ft
$X$	Streamwise spatial coordinate	ft
$X_i$	General species designator ( $X_i = O_2$ for oxygen)	
$[X_i]$	Concentration of species $X_i$	mole/ft <sup>3</sup>
$y$	Spatial coordinate normal to $x$	ft
$Y$	Spatial coordinate normal to $x$	ft
$y_L$	$y$ location of lower computational boundary	ft
$y_U$	$y$ location of upper computational boundary	ft
<i>Greek</i>		
$\alpha$	Constant in forward rate coefficient equation	
$\alpha_i$	Mass fraction of species $i$	
$\gamma$	Specific heat ratio	
$\gamma_f$	Frozen specific heat ratio	
$\Delta G^{P=1}$	Gibbs free energy of products minus the Gibbs free energy of the reactants	Btu/lbm
$\epsilon$	Turbulence energy dissipation rate	ft·lbf/sec
$\epsilon_o$	Activation energy per molecule	cal

$\eta$	Transformed y-direction coordinate	ft
$\theta$	Flow angle	deg
$\theta_B$	Attachment angle for nozzle parabolic wall section	deg
$\bar{\mu}$	Sum of laminar viscosity and turbulent viscosity	lbm/ft·sec
$\mu_l$	Laminar viscosity	lbm/ft·sec
$\mu_t$	Turbulent viscosity	lbm/ft·sec
$\nu_i'$	Stoichiometric mole numbers of reactants i	
$\nu_i''$	Stoichiometric mole numbers of products i	
$\xi$	Transformed x-direction coordinate	ft
$\rho$	Density	lbm/ft <sup>3</sup>
$\sigma_k$	Constant in turbulence equations	
$\sigma_\epsilon$	Constant in turbulence equations	
$\dot{\omega}_i$	Net rate of production of species i	lbm/sec

*Abstract*

The Scramjet Hypersonic Nozzle (SCHNOZ) parabolized Navier-Stokes computer code was used to model turbulent, chemically reacting flow present in a hypersonic nozzle. Two nozzle configurations were considered, an isolated nozzle (no external flow) and a nozzle with a finite length cowl. A single nonuniform entrance flow profile was generated and an equivalent uniform flow profile calculated for input into the nozzle code. Uniform and nonuniform cases for each nozzle were run using both frozen and finite rate chemistry. An increased grid resolution in the computer code was necessary to eliminate numerically induced anomalies in the results of the nonuniform cases for both nozzle configurations. Comparisons between the finite rate and frozen flow cases showed that chemistry was essentially frozen for the finite rate cases, indicating that for the nozzle inlet conditions and geometry used in this study, the extra computational time spent on finite rate kinetics was unnecessary. The effects of the nonuniform flowfield used in this study included an increase in the overall vehicle thrust and a decrease in the overall vehicle moment.



# Effect of Nonuniform Entrance Flow Profile on Hypersonic Nozzle Pitching Moment

## *I. Introduction*

### *1.1 Purpose*

To date, most nozzle thrust analyses for hypersonic scramjet-powered flight vehicles, such as the National Aerospace Plane, commonly assume that the flow properties leaving the combustor and entering the nozzle are uniform. Although this assumption greatly simplifies the analysis, there are many "real-life" factors which contribute to the generation of nonuniform combustor exit profiles which may in turn influence nozzle performance (6:4). Doty et al. (6), showed that moderate nonuniformities in the nozzle inlet profile had little effect on thrust produced by the nozzle. Doty et al. (5) also studied nonuniform profiles which were more severe and consequently had more influence on nozzle performance. These studies centered on the effects of nonuniform profiles on thrust; neither evaluated the effect of nonuniformities on pitching moment. If the pitching moment is altered, trim tabs in the exterior flow would be required to balance the overall vehicle moment. This would lead to a considerable increase in vehicle drag, reducing the net thrust and thus the flight performance of the hypersonic vehicle. The purpose of this study is therefore to determine the effects of nonuniform nozzle entrance flow profiles on the pitching moment of the hypersonic nozzle.

A typical hypersonic vehicle is shown in Figure 1.1. In this

configuration, the vehicle undersurface itself provides the main expansion surface of the nozzle and a short cowl comprises the initial portion of the lower nozzle surface. The remainder of the lower flowfield consists of a plume extending from the vehicle undersurface to a bounding shock wave (13:1, 4:1,5). Figure 1.2 is an enlarged view of a typical nozzle and cowl (not to scale).

## 1.2 Approach

The Scramjet Hypersonic Nozzle (SCHNOZ) parabolized Navier-Stokes computer code was used to model the turbulent, chemically reacting flow present in the hypersonic nozzle. This code was developed by Science Applications International Corporation (SAIC) for the National Aerospace Plane Program (NASP). It provides the capability of incorporating finite rate chemistry into the solution as well as frozen and perfect gas flow. SCHNOZ approximates the boundary layer with a slip condition at the nozzle wall; this eliminates subsonic viscous flow regions which would require an implicit solution procedure over the entire nozzle and thus allows the code to march through the nozzle flowfield explicitly. This approximation is allowable because pressure does not alter significantly through the boundary layer and because heat transfer and skin friction are not of interest for this study.

Typically, the cowl of a hypersonic nozzle is much shorter than the length of the vehicle undersurface, so that the external flow influences the nozzle flowfield for most of the length of the nozzle. A nozzle for which the cowl is the same length as or longer than the vehicle undersurface is called an isolated nozzle because the external flow has no influence over the nozzle flowfield. In order to isolate the effects of

the nonuniform nozzle inlet profile from those of the external flow, isolated nozzle cases were run for each of the regular nozzle cases (hereafter referred to as combined nozzle cases).

Eight cases were computed and analyzed for this study. The first four used chemically frozen flow, whereas the second four used flow with finite rate chemistry. The first two cases of each set used uniform flow entrance profiles, while the second two used nonuniform flow entrance profiles. Finally, all odd-numbered cases used the isolated nozzle. These cases are tabulated in Table 1.1. In addition to these cases, some grid comparison runs were made after problems were encountered with the grid size suggested by the SCHNOZ user's manual (13:98,108).

Table 1.1. Cases Used in Study

CASE 1	Frozen	Uniform	Isolated
CASE 2	Frozen	Uniform	Combined
CASE 3	Frozen	Nonuniform	Isolated
CASE 4	Frozen	Nonuniform	Combined
CASE 5	Finite Rate	Uniform	Isolated
CASE 6	Finite Rate	Uniform	Combined
CASE 7	Finite Rate	Nonuniform	Isolated
CASE 8	Finite Rate	Nonuniform	Combined

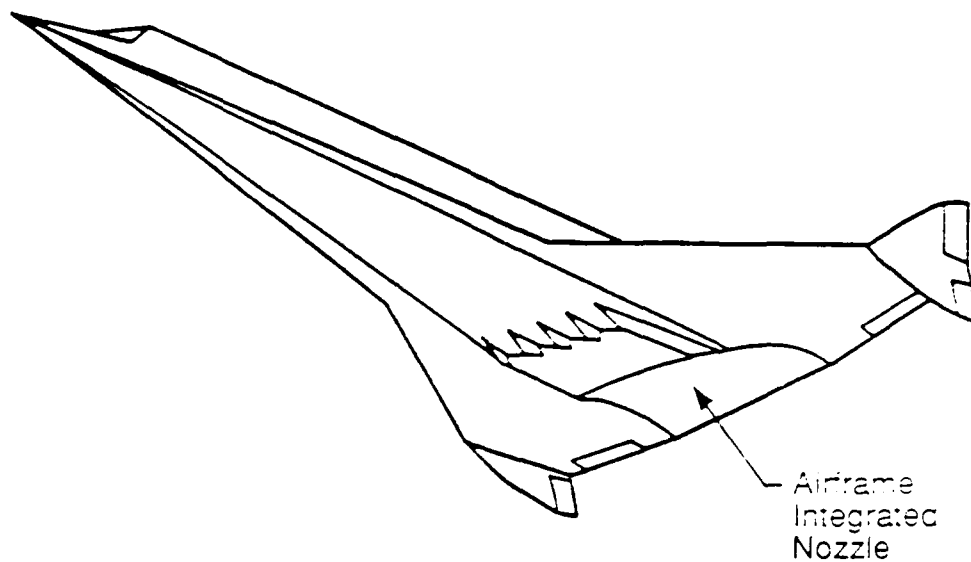


Figure 1.1. Typical Hypersonic Vehicle

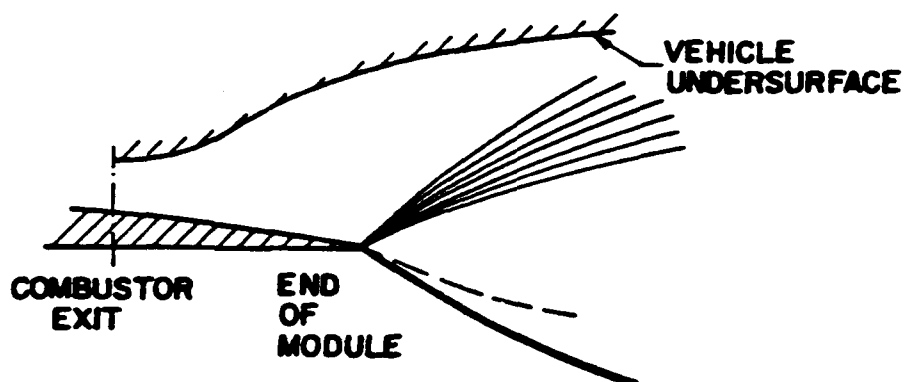


Figure 1.2. Expanded View of Nozzle and Cowl Section

## II. Theory

### 2.1 Mean Flow Equations

The equations used by SCHNOZ are simplified from the full Navier-Stokes equations for chemically reacting viscous flows and will be presented only briefly here since this study is not an algorithm development effort. The full Navier-Stokes equations are discussed in detail in Anderson (2). The turbulent flow equations were derived from the Navier-Stokes equations by Sislian (11) by mass-averaging the instantaneous variables except for density, pressure, and viscous stresses; these three variables were time averaged. Reynolds rules of averaging were then applied (11:2-9) and the resulting turbulent flow equations were parabolized by neglecting all stress terms containing streamwise derivatives and all unsteady terms (3:14-17). The transport of mass by diffusion and energy by thermal conduction was taken to be the same, resulting in a Lewis number of unity and the elimination of diffusion terms from the energy equation (11:5). The turbulent stress terms in the normal momentum equation were also neglected (13:8). The resulting planar parabolized Navier-Stokes (PNS) equations are listed below:

*Continuity:*

$$\frac{\partial(\rho u)}{\partial x} + \frac{\partial(\rho v)}{\partial y} = 0 \quad (2.1)$$

*X-Momentum:*

$$\frac{\partial(p + \rho u^2)}{\partial x} + \frac{\partial(\rho uv)}{\partial y} = \frac{\partial}{\partial y} \left( \bar{\mu} \frac{\partial u}{\partial y} \right) \quad (2.2)$$

Y-Momentum:

$$\frac{\partial(\rho uv)}{\partial x} + \frac{\partial(p + \rho v^2)}{\partial y} = \frac{\partial}{\partial y} \left( \tilde{\mu} \frac{\partial v}{\partial y} \right) \quad (2.3)$$

Total Enthalpy:

$$\frac{\partial(\rho uH)}{\partial x} + \frac{\partial(\rho vH)}{\partial y} - \frac{\partial}{\partial y} \left[ \frac{(\tilde{P}_T - 1)}{\tilde{P}_T} \tilde{\mu} \frac{\partial}{\partial y} \left( \frac{u^2}{2} \right) \right] = \frac{\partial}{\partial y} \left( \frac{\tilde{\mu}}{\tilde{P}_T} \frac{\partial H}{\partial y} \right) \quad (2.4)$$

Species Continuity:

$$\frac{\partial(\rho u \alpha_i)}{\partial x} + \frac{\partial(\rho v \alpha_i)}{\partial y} - \dot{\omega}_i = \frac{\partial}{\partial y} \left( \frac{\tilde{\mu}}{\tilde{P}_T} \frac{\partial \alpha_i}{\partial y} \right) \quad (2.5)$$

## 2.2 Turbulence Model

The turbulence model used for this study is the two equation  $k\epsilon$  eddy viscosity model. It is explained in detail by Launder et al. (10) and Dash et al. (3) and is summarized below. This model uses the turbulence energy dissipation rate,  $\epsilon$ , as the length scale parameter which is related to the turbulent kinetic energy,  $k$ , and the turbulent length scale,  $\ell$ , by the equation:

$$\epsilon = \frac{k^{3/2}}{\ell} \quad (2.6)$$

The turbulent viscosity,  $\mu_t$ , is then determined from the relation:

$$\mu_t = C_\mu \rho k^{\frac{1}{2}} \ell = C_\mu \rho \frac{k^2}{\epsilon} \quad (2.7)$$

Partial differential equations for the production, dissipation, and transport of  $k$  and  $\epsilon$  for planar flow are developed from the Navier-Stokes equations and parabolized by eliminating all diffusive terms containing streamwise derivatives (10:74-77,95-97; 3:17-18). These equations are then used in the form shown below:

$$\frac{\partial}{\partial x}(\rho u k) + \frac{\partial}{\partial y}(\rho v k) = \frac{\partial}{\partial y} \left( \frac{\mu_t}{\sigma_k} \frac{\partial k}{\partial y} \right) + \left[ \mu_t \left( \frac{\partial u}{\partial y} \right)^2 - \rho \epsilon \right] \quad (2.8)$$

$$\frac{\partial}{\partial x}(\rho u \epsilon) + \frac{\partial}{\partial y}(\rho v \epsilon) = \frac{\partial}{\partial y} \left( \frac{\mu_t}{\sigma_\epsilon} \frac{\partial \epsilon}{\partial y} \right) + \left[ C_1 \mu_t \left( \frac{\partial u}{\partial y} \right)^2 - C_2 \rho \epsilon \right] \frac{\epsilon}{k} \quad (2.9)$$

The constants used in equations (2.8) and (2.9) are as follows (13:10):

$$\begin{aligned} C_1 &= 1.43 & \sigma_k &= 1.0 \\ C_2 &= 1.92 & \sigma_\epsilon &= 1.3 \\ C_\mu &= .09 \end{aligned}$$

The basic  $k\epsilon$  model is based on incompressible assumptions and overestimates the rate of mixing for high Mach number free shear flows. Therefore, a compressibility-corrected turbulent viscosity (13:10) is used which is given by:

$$\mu_t = K(M_r) C_\mu \rho \frac{k^2}{\epsilon} \quad (2.10)$$

where  $K(M_r)$  is the correction factor. The characteristic Mach number,  $M_r$ , of the turbulence is given by:

$$M_r = \frac{k_{\max}}{a_{\max}} \quad (2.11)$$

where  $k_{\max}$  is the maximum value of  $k$  at each axial station and  $a_{\max}$  is the local sound speed at the location of  $k_{\max}$ . The functional form of  $K(M_r)$  is determined from comparison with experimental data and is shown in Figure 2.1 (13:10-11).

### 2.3 Supplemental Equations

An equation of state is needed to complement the above equations (13:12) and is given by:

$$p = \rho R_o T / W \quad (2.12)$$

This is the thermally perfect equation of state where  $R_o$  is the universal gas constant and  $W$  is the mixture molecular weight, given by

$$W = \sum_{i=1}^n (\alpha_i / m_i)^{-1} \quad (2.13)$$

and  $m_i$  is the molecular weight of the individual species  $i$  (13:12).

The static enthalpy,  $h$ , is given by the equations

$$h = \sum_{i=1}^n \alpha_i h_i(T) \quad (2.14)$$

and the total enthalpy,  $H$ , is defined as



$$H = h + \frac{(u^2 + v^2)}{2} \quad (2.15)$$

The frozen specific heat at constant pressure,  $C_{pf}$ , of the mixture is found by combining equation (2.14) with the definition of specific heat:

$$C_p = \left( \frac{\partial h}{\partial T} \right)_p \quad (2.16)$$

to get, for a chemically reacting mixture:

$$C_p = \left[ \frac{\partial}{\partial T} \left( \sum_i^n \alpha_i h_i \right) \right]_p = \sum_i \alpha_i \left( \frac{\partial h_i}{\partial T} \right)_p + \sum_i h_i \left( \frac{\partial \alpha_i}{\partial T} \right)_p \quad (2.17)$$

For frozen flow, the term  $(\partial \alpha_i / \partial T)_p = 0$ . Thus, the equation for specific heat at constant pressure becomes:

$$C_{pf} = \sum_{i=1}^n \alpha_i C_{pi}(T) \quad (2.18)$$

where the specific heat at constant pressure per unit mass for the pure species  $i$ ,  $C_{pi}$ , is given by:

$$C_{pi} = \left( \frac{\partial h_i}{\partial T} \right)_p \quad (2.19)$$

The static enthalpy for each species,  $h_i(T)$ , and the specific heat at constant pressure for each species,  $C_{pi}$ , are determined from a thermodynamic databank in the computer code (13:12-13; 2:530-531).

The frozen specific heat ratio,  $\gamma_f$ , and the frozen sound speed,

$a_f$ , are given by the equations

$$\gamma_f = \frac{C_p W / R_o}{(C_p W / R_o) - 1} \quad (2.20)$$

and

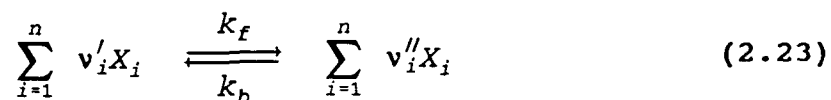
$$a_f = [\gamma_f R_o T / W]^{1/2} = [\gamma_f p / \rho]^{1/2} \quad (2.21)$$

The Mach number for frozen flow is then defined as

$$M = \frac{(u^2 + v^2)^{1/2}}{a_f} \quad (2.22)$$

#### 2.4 Chemical Kinetics

For a reacting mixture of  $n$  different species,  $X_i$ , the general chemical reaction equation is as follows:



where  $\nu_i'$  and  $\nu_i''$  are the stoichiometric mole numbers of the reactants and products, respectively, and  $k_f$  and  $k_b$  are the forward and reverse reaction rate constants. The stoichiometric mole numbers are positive for products and negative for reactants. The net rate of production of species  $i$  is then given by the equation:

$$\frac{d[X_i]}{dt} = (v''_i - v'_i) \left\{ k_f \prod_i [X_i]^{v'_i} - k_b \prod_i [X_i]^{v''_i} \right\} \quad (2.24)$$

where the notation  $[X_i]$  denotes the concentration of species  $i$  in moles per unit volume. The rate constants,  $k_f$  and  $k_b$ , are related by the equilibrium constant based on concentrations,  $K_c$ , such that:

$$\frac{k_f}{k_b} = K_c \quad (2.25)$$

where  $K_c$  can be found from the equilibrium constant based on partial pressures,  $K_p$ , using the equation:

$$K_c = \left( \frac{1}{R_o T} \right)^{\sum_i v_i} K_p \quad (2.26)$$

In practice, values for  $k_f$  are found from experiment and then  $k_b$  is determined from equations (2.25) and (2.26). The forward rate coefficient,  $k_f$ , is generally given by the equation:

$$k_f = c_1 T^\alpha e^{-\epsilon_o/kT} \quad (2.27)$$

where  $c_1$ ,  $\alpha$ , and  $\epsilon_o$  are all found from experimental data. The variable  $\epsilon_o$  is the energy required per molecule for the chemical reaction to take place (activation energy) and  $k$  is Boltzmann's constant. Equation (2.27) can also be written as

$$k_f = C_1 T^\alpha e^{-B/R_o T} \quad (2.28)$$

where B is the energy required per mole for reaction (2:491-494,501). The equilibrium constant based on partial pressures,  $K_p$ , is determined from the Gibbs free energy and temperature via the equation:

$$K_p(T) = e^{-\Delta G^{P=1}/R_o T} \quad (2.29)$$

In this equation  $\Delta G^{P=1}$  is the Gibbs free energy of the products minus the Gibbs free energy of the reactants for a given chemical equation with all species evaluated at a pressure of one atmosphere and a specified temperature (2:402-406). Values of  $G^{P=1}$  are determined from a thermodynamic databank in the computer code. The species concentration,  $[X_i]$ , in equation (2.24) can also be written as

$$[X_i] = \rho F_i \quad (2.30)$$

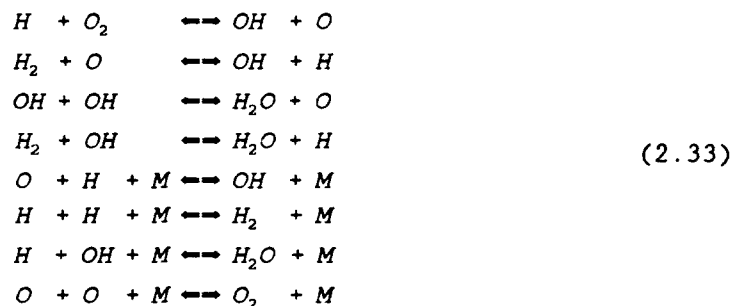
where  $\rho$  is the density of the mixture and  $F_i$  is the mass fraction of species i divided by its molecular weight:

$$F_i = \frac{\alpha_i}{m_i} \quad (2.31)$$

Equation (2.24) can then be written as

$$\dot{\omega}_i \equiv \frac{d[X_i]}{dt} = k_f(v_i'' - v_i') \left\{ \prod_i (\rho_{F_i})^{v_i'} - \frac{(R_o T)^{\sum_i v_i}}{K_p} \prod_i (\rho_{F_i})^{v_i''} \right\} \quad (2.32)$$

The chemical reactions considered for this study are as follows:



In these equations M is a third body which can be a molecule of any species present. For this system, all third bodies are assumed to have equal efficiencies in contributing to reactions so that when  $\dot{\omega}_i$  is evaluated,  $F_M = (W)^{-1}$  (13:15-17). The rate of production of a species i for the system is then the sum of the rates for the individual reactions (2:496-497).

## 2.5 Nonuniform Flow Averaging (12:18-31)

The nonuniform flow averaging procedure used in this study was that used by Thompson and Hoffman (12) and is briefly described below. When a nonuniform flow profile is used for the nozzle inlet condition, an equivalent uniform flow profile can be obtained such that the extensive flow properties (mass, momentum, total energy, stream thrust, and kinetic energy) are the same for both flows. The results obtained from this equivalent profile can then be compared to the results of the nonuniform profile to determine the effects of the nonuniformities on

the nozzle flowfield. The uniform profile is obtained by averaging the intensive flow properties (pressure, density, enthalpy, temperature, entropy, velocity, stagnation temperature, and stagnation pressure) of the nonuniform flow in such a way that the values obtained are representative of the nonuniform flow and self-consistent with the governing equations for uniform flow.

To average the flow properties of a nonuniform profile, a weighting function,  $w$ , is defined such that

$$\bar{f} = \frac{1}{W} \int f dw \quad (2.34)$$

where  $f$  is any flow property,  $\bar{f}$  is the  $w$ -averaged property, and  $W$  is given by the equation:

$$W = \int dw \quad (2.35)$$

For this study, the weighting function chosen was mass, so that

$$\bar{f} = \frac{1}{m} \int f dm = \frac{1}{m} \int f \rho dV \quad (2.36)$$

Note, this weighting function is not the only weighting function put forth by Thompson and Hoffman (12), but it was chosen as a realistic representative function for determining the profile properties since mass is a basic conserved property. When the nonuniform averaging is performed on the intensive properties, the set of uniform averaged properties obtained are not consistent with the mean flow equations, Eqs (2.1) through (2.5). To obtain a consistent set, three base properties

are chosen to represent the properties of the flow and the remaining properties are calculated using the perfect gas uniform flow equations. The three base properties chosen can be any independent combination of extensive properties and uniform averaged intensive properties. The three properties used in this study are those used by Thompson and Hoffman (12) for their mass-averaged case and are mass flow rate,  $\dot{m}$ , the extensive energy flow rate,  $\mathcal{E}$ , and the mass-averaged Mach number,  $\bar{M}$ . The remaining properties are then found from the following uniform flow equations for inviscid, isentropic flow in a perfect gas:

$$\begin{aligned}
 T_t &= \frac{\mathcal{E}}{\dot{m}c_p} \\
 P &= \frac{\dot{m}}{A M \sqrt{\gamma R T_t} \left(1 + \frac{\gamma-1}{2} M^2\right)^{1/2}} \\
 T &= \frac{T_t}{1 + \frac{\gamma-1}{2} M^2} \\
 u &= M \sqrt{\gamma R T} \quad (v = 0) \\
 P_t &= P \left(1 + \frac{\gamma-1}{2} M^2\right)^{\frac{\gamma}{\gamma-1}}
 \end{aligned} \tag{2.37}$$

The uniform flow properties obtained from the above equations will not be exactly equal to the corresponding uniform averaged properties and the extensive properties of the nonuniform flow will also not be equal to those obtained from the uniform flow intensive properties. The difference between a uniform averaged property and its equivalent uniform flow property can be used as a measure of adequacy of the uniform property set in representing the nonuniform flow.

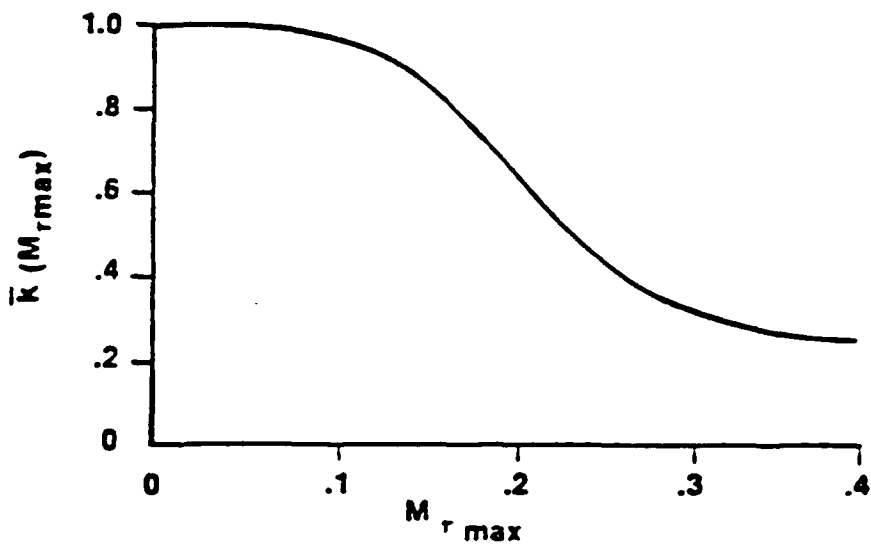


Figure 2.1. Compressibility Correction Factor for  $k\epsilon$  Turbulence Models



### III. Methodology

#### 3.1 PNS Code Description

The following transformation of physical space to the rectangular computational coordinates,  $\xi$  and  $\eta$ , is employed by SCHNOZ:

$$\begin{aligned}\xi &= x \\ \eta &= [y - y_L(x)] / [y_U(x) - y_L(x)]\end{aligned}\quad (3.1)$$

SCHNOZ solves the following conservative form of the PNS equations:

$$\frac{\partial \vec{E}}{\partial x} + \frac{\partial \vec{F}}{\partial y} + \vec{G} = \frac{\partial}{\partial y} \left( \frac{\mu}{\sigma_r} \frac{\partial \vec{f}}{\partial y} \right) \quad (3.2)$$

where

$$\vec{E} = \begin{bmatrix} \rho u \\ p + \rho u^2 \\ \rho uv \\ \rho uH \\ \rho u\alpha_i \end{bmatrix}, \quad \vec{F} = \begin{bmatrix} \rho v \\ \rho uv \\ p + \rho v^2 \\ \rho vH \\ \rho v\alpha_i \end{bmatrix}, \quad \vec{G} = \begin{bmatrix} 0 \\ 0 \\ 0 \\ -\frac{\partial}{\partial y} \left[ \frac{\bar{p}_r - 1}{\bar{p}_r} \bar{\mu} \frac{\partial}{\partial y} \left( \frac{u^2}{2} \right) \right] \\ -\dot{\omega}_i \end{bmatrix}, \quad \vec{f} = \begin{bmatrix} 0 \\ u \\ v \\ H \\ \alpha_i \end{bmatrix} \quad (3.3)$$

and for  $f = u, v, H$ , and  $\alpha_i$ ,

$$\sigma_u = \sigma_v = 1, \quad \sigma_H = \sigma_{\alpha_i} = \bar{p}_r \quad (3.4)$$

These equations are transformed into the computational coordinates and then used in the explicit MacCormack algorithm. This algorithm uses the following predictor and corrector steps to advance the flow from  $\xi$  to  $\xi + \Delta\xi$  at interior grid point I:

*Predictor Step:*

$$\begin{aligned}\tilde{E}_I = E_I^K - \frac{\Delta\xi}{\Delta\eta} \{ (1-e)F_{I+1} - (1-2e)F_I - eF_{I-1} - G_I\Delta\xi \} \\ + \frac{\Delta\xi b^2}{\Delta\eta^2} \{ A^* f_{I+1} - f_I - A^- (f_I - f_{I-1}) \}\end{aligned}\quad (3.5)$$

*Corrector Step:*

$$\begin{aligned}E_I^{K+1} = \frac{1}{2} [ E_I^K + \tilde{E}_I - \frac{\Delta\xi}{\Delta\eta} \{ \tilde{e}F_{I+1} + (1-2e)\tilde{F}_I + (e-1)\tilde{F}_{I-1} \} \\ - \tilde{G}_I\Delta\xi + \frac{\Delta\xi b^2}{\Delta\eta^2} \{ \tilde{A}^* (\tilde{F}_{I+1} - \tilde{F}_I) - \tilde{A}^- (\tilde{F}_I - \tilde{F}_{I-1}) \} ]\end{aligned}\quad (3.6)$$

where:

$$A^* = \frac{1}{2} \left[ \left( \frac{\tilde{u}}{\sigma_f} \right)_I + \left( \frac{\tilde{u}}{\sigma_f} \right)_{I+1} \right] \quad (3.7)$$

and  $e$  is an alternating difference switch ( $e = 0$  at even steps;  $e = 1$  at odd steps). The index in the axial direction,  $\xi$ , is  $K$  and the index in the transverse direction,  $\eta$ , is  $I$ . The transverse grid intervals,  $\Delta\eta$ , used in SCHNOZ are equally spaced (13:23).

There are several boundary conditions available in SCHNOZ. The lower computational boundary is restricted to being either a solid surface or a plane of symmetry. The upper boundary can be a solid surface, fitted shock, or a stream surface. Therefore, to run the cases for this study, the computational nozzle geometry is flipped with respect to the real world geometry (13:18). The nozzle geometry is shown in Figure 3.1.

The dual boundary conditions on the upper computational boundary (cowl wall then plumed flow) require the code to switch boundary conditions at the end of the cowl. SCHNOZ accomplishes this by running

the internal and external flow as two separate domains until a shear layer is formed (the position of the shear layer start past the cowl is specified by the user). At this point SCHNOZ combines the two grids by dividing the entire domain into equally spaced intervals,  $\Delta\eta$ , with the total number of grid points from both domains minus any points deleted in creating the shear layer. The viscous coupling of the two domains is accomplished using overlapping grid procedures (13:21-22). More details are given by Wolf et al. (13:33-34).

The wall boundary points are solved by the MacCormack algorithm and an Abbett correction procedure (13:31). In general, the MacCormack algorithm may not exactly satisfy the surface tangency condition for flow at the wall, so the correction must account for the influence of the wall on the interior flow. The changes in surface slope can locally be considered to result in a sequence of infinitesimal simple expansion or compression waves. Thus, the correction involves a simple wave expression for a change in slope,  $\Delta\theta$ , (1:160-161) which is used to satisfy the surface tangency condition, resulting in a corrected pressure,  $p'$ :

$$p' = p - \frac{\gamma p M^2}{\sqrt{M^2 - 1}} \Delta\theta \quad (3.8)$$

The total energy and total velocity magnitude are left unchanged from the predictor step and the velocity components,  $u$  and  $v$ , are then calculated based on the actual wall angle. The corrected pressure is used to also correct the density. SCHNOZ also contains an option to calculate the flow conditions at the wall points via characteristic relations instead of the above predictor/corrector steps (13:31).

In regions of strong shocks, SCHNOZ employs a self-adjusting

hybrid scheme developed by Harten and Zwas (13:23-24) to correct nonphysical pressure oscillations introduced by the basic MacCormack scheme. This procedure adds an extra dissipative term to the conservation equations which changes the second order MacCormack scheme to a first order scheme near shock waves. The dissipative term is triggered by dimensionless switches, which vary from 0 to 1, and are based on the pressure gradient on either side of the grid point under consideration. Figure 3.2 shows before and after results for a pressure profile using the Harten-Zwas approach (13:23-24). Note that the oscillations present at the pressure discontinuity in the no-damping case are smoothed out by the self-adjusting hybrid correction. Additional details concerning this procedure are given by Harten and Zwas (8).

The chemical source term,  $\dot{\omega}_i$ , in the species continuity equation is dealt with by estimating predictor-level and corrector-level values of  $\dot{\omega}$  and then performing point-implicit integration of the chemical kinetic equation:

$$\rho \frac{d\alpha_i}{dt} = \dot{\omega}_i(\alpha_i, \rho, T) \quad (3.9)$$

where  $\rho$ ,  $T$ , and  $\alpha_i$  are the appropriate predictor or corrector values. The point-implicit integration of equation (3.9) uses a species linearization of the  $\dot{\omega}_i$  term which is discussed in detail by Wolf et al. (13:24-30).

### 3.2 Hypersonic Nozzle

The nozzle contour used for this study is an optimized contour obtained from Doty (4) which consists of two sections. Referring to

Figure 3.1, the first section, A-B, is a circular arc of radius  $r$  which attaches to a parabolic section, B-C, with an attachment angle,  $\theta_B$ . The cowl consists of three sections: a straight section, O-D-E, a short circular arc, and another straight section, E-F. Table 3.1 lists the pertinent nozzle geometric parameters.

Table 3.1. Nozzle and Cowl Geometry Specifications

Inlet height, $h$ (inches)	1.0
Nozzle wall start, $x/h$	0.0
Nozzle wall start, $y/h$	0.0
Nozzle circular arc radius (inches)	1.0
Nozzle circular arc end, $x/h$	0.6142
Attachment angle, $\theta_B$ (deg)	-38.0
Nozzle wall end, $x/h$	100.0
Nozzle wall end, $y/h$	-24.0
Nozzle wall end angle (deg)	-8.04
Cowl start, $x/h$	0.0
Cowl start, $y/h$	1.0
First cowl section angle (deg)	0.0
Cowl circular arc start, $x/h$	8.496
Cowl circular arc radius (inches)	1.0
Third cowl section start, $x/h$	8.669
Third cowl section angle (deg)	10.0
Cowl end, $x/h$	10.0
Cowl end, $y/h$	1.25

### 3.3 Freestream Conditions

The freestream conditions used for this study are those for a typical hypersonic vehicle flying through air at a Mach number of 15, an

altitude of 130,000 feet and a dynamic pressure,  $q_\infty$ , of 1000 psf where

$$q_\infty = \frac{1}{2} \rho_\infty |\vec{V}_\infty|^2 \quad (3.10)$$

The remaining freestream parameters were calculated by Herring (9) using the 1962 standard atmosphere. The freestream conditions are tabulated in Table 3.2.

Table 3.2. Freestream Conditions

Mach number	15.0
Altitude (ft)	129856.3
Dynamic pressure, $q_\infty$ (psf)	1000.0
Pressure (psf)	6.349
Temperature ( $^{\circ}$ R)	448.527
Density (lbm/ft <sup>3</sup> )	0.000265

#### 3.4 External Flow Conditions

The external flow parameters used for this study were taken from Herring's work (9) and are listed below in Table 3.3. These data were found by using the freestream conditions described previously to obtain an oblique shock solution for a calorically imperfect gas with an effective turning angle of  $8^{\circ}$ . This shock is representative of the shock(s) created by the nose and/or inlet of the hypersonic vehicle. The chemical composition was obtained from a NASA chemical equilibrium composition code, CET85 (7). This code determines the composition for a given pressure, temperature, and fuel ratio. To obtain the composition for the external conditions, a mixture of air (no Argon) and 0.0001 percent fuel ( $H_2$ ) was used, since the code would not accept a fuel ratio

of 0. This data is tabulated in Table 3.4 (7).

Table 3.3. External Flow Conditions

Mach number	9.449
Pressure (psi)	0.4115
Temperature (°R)	1113.104
Density (lbm/ft <sup>3</sup> )	0.000998
Velocity (ft/sec)	15310.9

Table 3.4. Chemical Composition for External Flow

Molecular weight	28.850
Gamma	1.372
H <sub>2</sub> O mole fraction	0.00001
N <sub>2</sub> mole fraction	0.78992
O <sub>2</sub> mole fraction	0.21007

### 3.5 Nozzle Inlet Conditions (12:32-37)

The nonuniform inlet profiles and the equivalent uniform conditions were taken from the work of Thompson and Hoffman (12). The Mach number profile was assumed to be symmetric across the nozzle inlet and was determined from the equation:

$$M = 3.5857 - 1.5857 \exp[-11.67(y-0.5)^2] \quad (3.11)$$

The stagnation temperature profile was assumed to be parabolic and is given by

$$T_t = 6000 - 4(6000 - 4000)(y - 0.5)^2 \quad (3.12)$$

The static pressure,  $p$ , was assumed to be uniform across the nozzle inlet at 25 psia. The remaining properties were calculated from these profiles using the perfect gas relations and the following constants for a thermally and calorically perfect gas:

$$R = 50.64 \text{ (ft-lbf)/(lbm-R)}$$

$$\text{Gamma} = 1.35$$

$$C_p = 0.251010 \text{ Btu/(lbm-R)}$$

The profiles for Mach number, total temperature, total pressure, static temperature, and velocity are tabulated for the lower half of the nozzle inlet in Appendix C and shown graphically in Figures 3.3 through 3.7. The equilibrium composition was determined at each point using CET85 (7). A stoichiometric fuel/air ratio of 0.029356 was used and again, the air has no Argon. The composition is tabulated in Appendix C for the lower half of the nozzle inlet.

The mass-averaged equivalent uniform flow profile was also taken from Thompson and Hoffman (12). As stated previously in Section 2.5, the base properties used to compute this profile were mass flow rate,  $\dot{m}$ , the extensive energy flow rate,  $\dot{E}$ , and the mass-averaged Mach number,  $\bar{M}$ . The uniform properties are given in Table 3.5 and are shown as straight dashed lines in Figures 3.3 through 3.7.



Table 3.5. Equivalent Uniform Flow Properties

Mach number, $M$	2.9389
Velocity, $u$ (ft/sec)	6231.4
Total Temperature, $T_t$ ( $^{\circ}R$ )	5133.34
Total Pressure, $p_t$ (psi)	817.05
Pressure, $p$ (psi)	23.4230
Temperature, $T$ ( $^{\circ}R$ )	2043.9

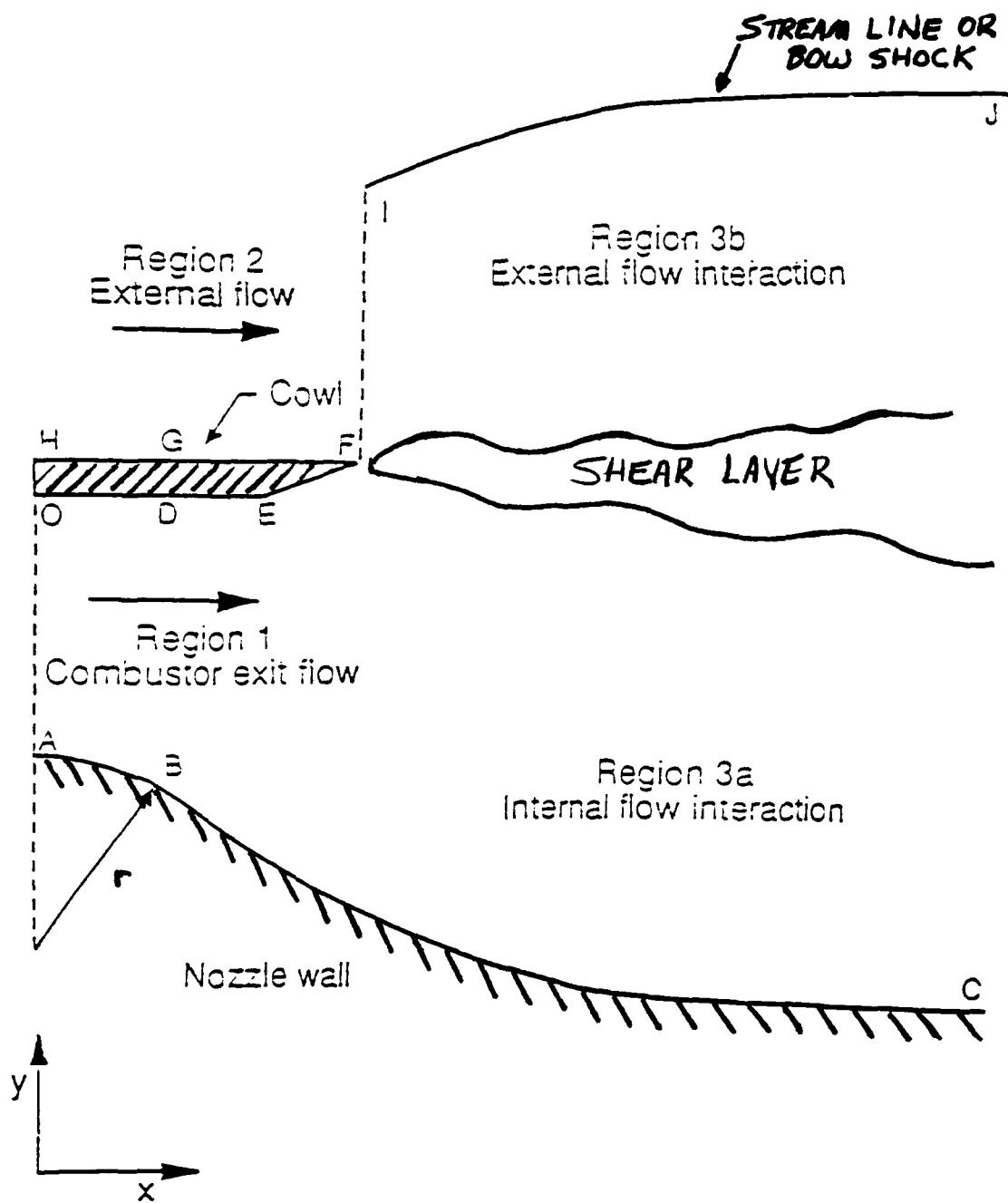


Figure 3.1. Nozzle Geometry for all Cases

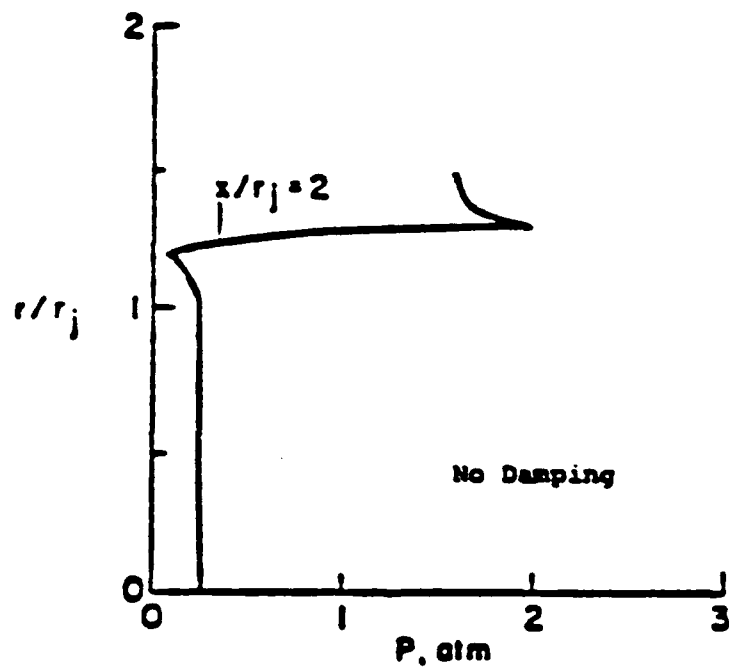
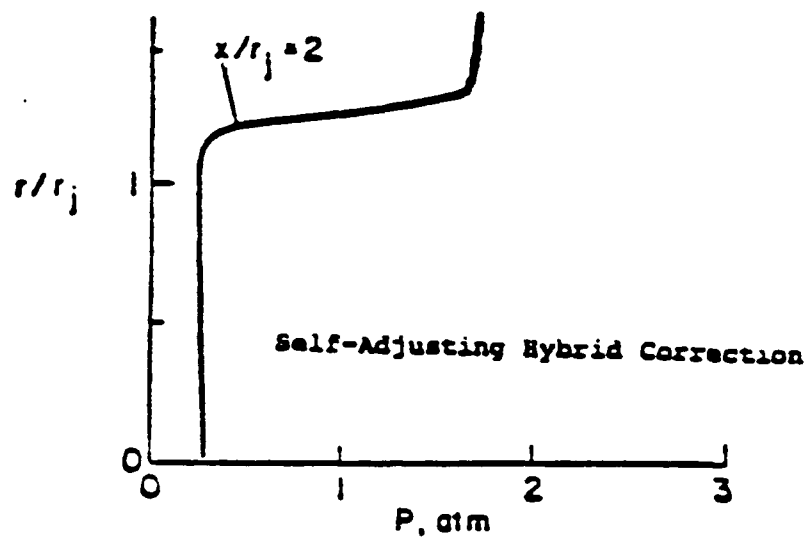


Figure 3.2. Pressure Profile Improvements in Vicinity of Captured Shock Using Harten-Zwas Self-Adjusting Damping Correction (13:25)

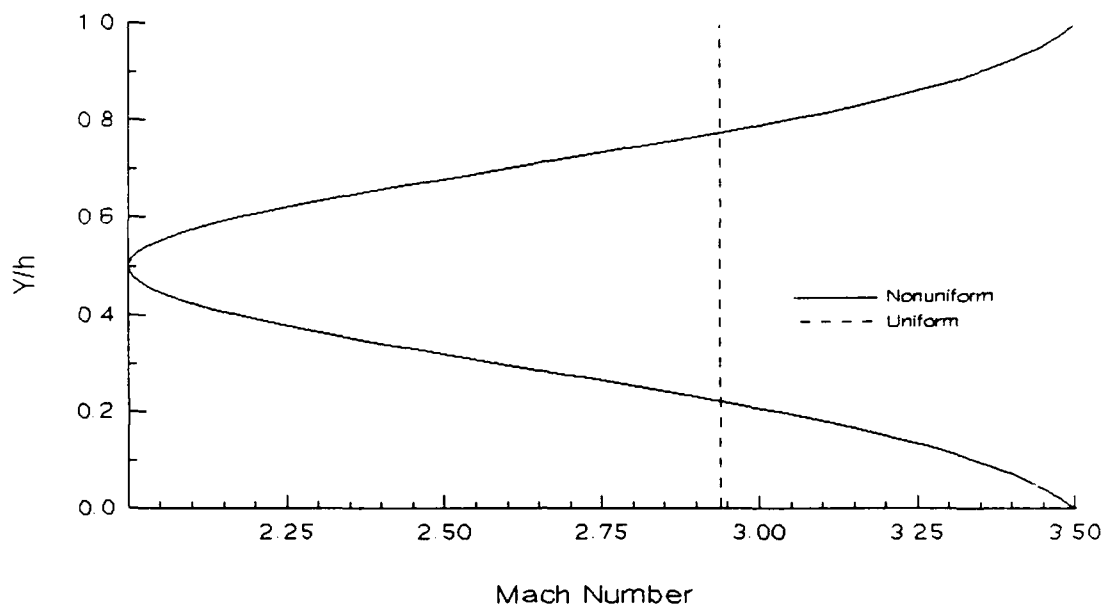


Figure 3.3. Nonuniform Mach Number Profile

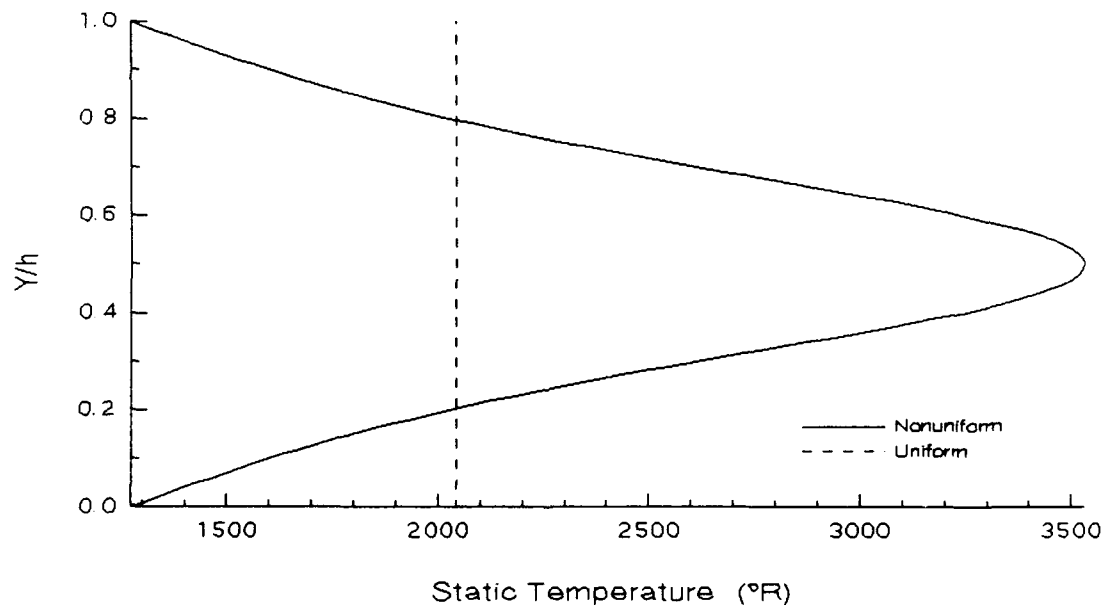
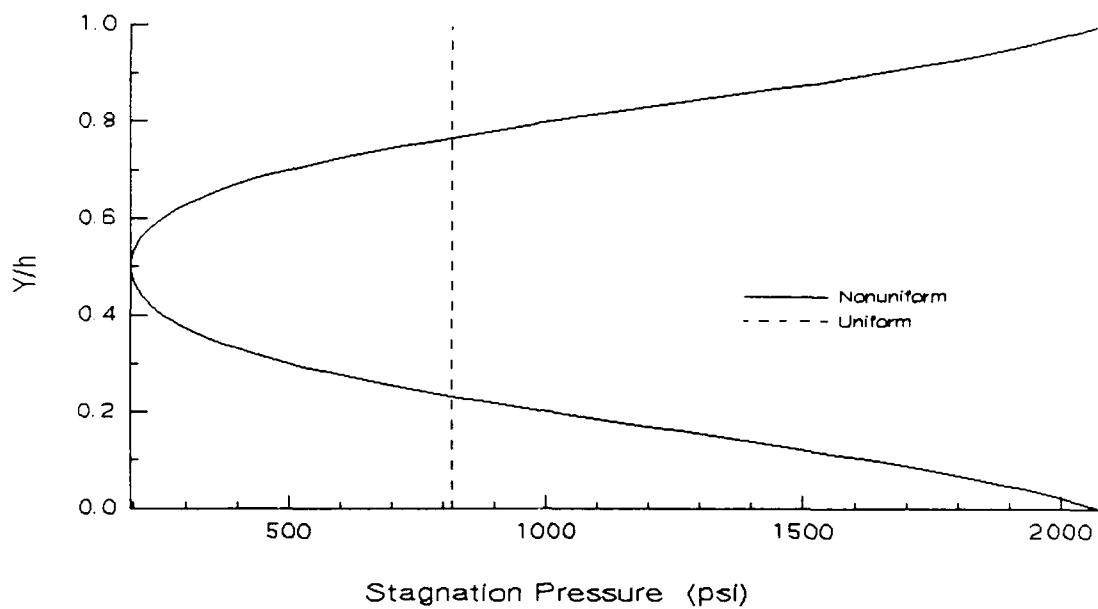
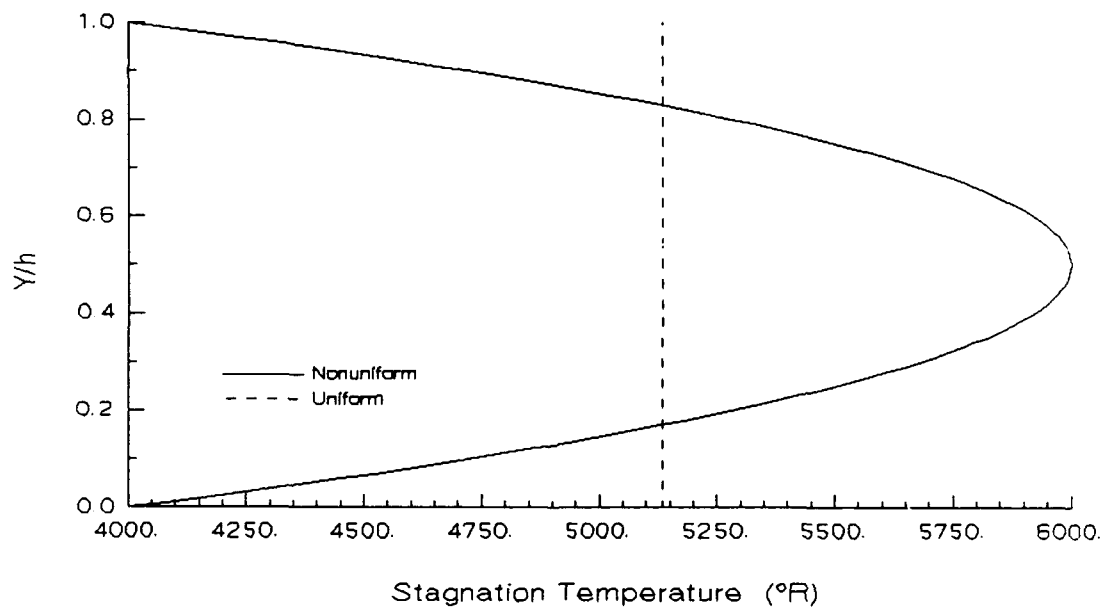


Figure 3.4. Nonuniform Static Temperature Profile



**Figure 3.5. Nonuniform Stagnation Pressure Profile**



**Figure 3.6. Nonuniform Stagnation Temperature Profile**

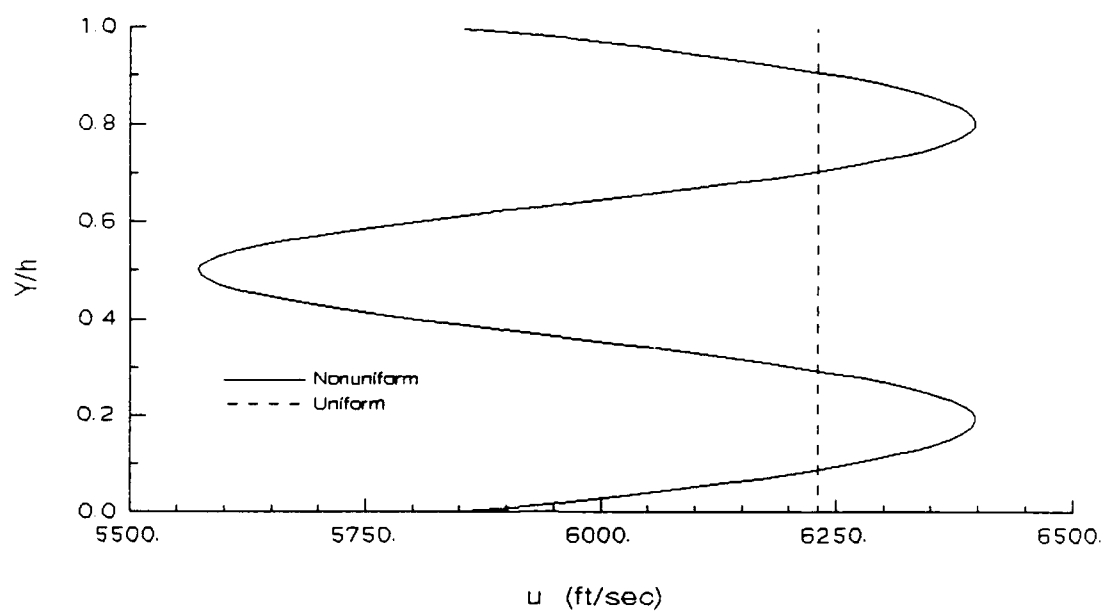


**Figure 3.7.** Nonuniform Velocity Entrance Profile

## IV. Results

### 4.1 Case Summary

Eight cases were run for this study using SCHNOZ. The first four cases used frozen flow and the last four cases used finite rate flow. Cases 1, 2, 5, and 6 used uniform flow entrance profiles and the remaining cases used nonuniform flow entrance profiles. All odd numbered cases were run using the isolated nozzle geometry and all even numbered cases were run using the combined nozzle geometry. These cases are listed in Table 1.1 and are restated in Table 4.1 for easy reference. Please note, all nozzle wall pressure plots in this section are truncated on the Y-axis so that details may be seen more clearly. Plots showing the entire range of nozzle wall pressures can be found in Appendix A.

Table 4.1. Cases Used in Study

CASE 1	Frozen	Uniform	Isolated
CASE 2	Frozen	Uniform	Combined
CASE 3	Frozen	Nonuniform	Isolated
CASE 4	Frozen	Nonuniform	Combined
CASE 5	Finite Rate	Uniform	Isolated
CASE 6	Finite Rate	Uniform	Combined
CASE 7	Finite Rate	Nonuniform	Isolated
CASE 8	Finite Rate	Nonuniform	Combined

#### 4.2 Grid Refinement

As delivered to the National Aerospace Plane Program by SAIC, SCHNOZ was dimensioned with a maximum grid size in the y direction of 50 points. Wolf et al. (13) recommended 31 points in the transverse direction (along A-O in Figure 3.1) for the internal flow and 21 points for the external flow (line I-F in Figure 3.1). When SCHNOZ combines the two domains the total number of points becomes 50. This was found to be inappropriate for the nozzle under consideration due to a combination of the severe expansion region caused by the circular arc at the beginning of the nozzle wall and the nonuniform flow profile. The code was modified to accommodate 101 points for the internal flow and 51 points for the external flow.

Figures 4.1 and 4.2 are static nozzle wall temperature plots for the coarse and fine grids for uniform flow in a combined nozzle and nonuniform flow in a combined nozzle, respectively. A comparison of the coarse grid plots to the fine grid plots in these two figures indicates that the nonuniform flowfield is more sensitive to the grid resolution than the uniform flowfield. For both the uniform and nonuniform flowfields, the expansion around the nozzle wall circular arc (A-B in Figure 3.1) is underpredicted for the coarse grid relative to the fine grid. Subsequently, the recompression along the parabolic wall (B-C in Figure 3.1) is overpredicted. The reason for these errors is that the MacCormack algorithm is unable to keep track of the rapid change in flow properties encountered at the nozzle wall due to the coarse grid. The larger change in the temperature plots for the nonuniform cases, which can be seen in Figure 4.2, is due to the large property gradients which need to be resolved across the flowfield as a result of the



nonuniformities present in the flow. Since the grid spacing is not small enough to resolve the gradients in the flow, numerically induced anomalies are introduced into the flowfield which propagate down the nozzle with the marching solution.

Also shown on Figures 4.1 and 4.2 are two different initial computational boundary locations,  $(Y/h)_{\max}$ . The location,  $(Y/h)_{\max}$ , corresponds to point I on Figure 3.1. For the initial code runs an arbitrary value of 10.0 was chosen for  $(Y/h)_{\max}$ . Once the grid was refined, small discontinuities still remained in the nozzle wall property plots for the nonuniform cases. This occurred where SCHNOZ recombines the grid for the internal and external nozzle flows at point F ( $X/h=10.0$ ). A new value for  $(Y/h)_{\max}$ , 4.5, was obtained by taking the nozzle width at that point, dividing by 101 to get the grid spacing, multiplying by 51 to get the width of the external flow and adding this to the cowl  $Y/h$  position at point F on Figure 3.1. This reduced the change in grid size at the recombination point to one which the MacCormack algorithm could tolerate, thus eliminating the discontinuities. Runs with  $(Y/h)_{\max}$  set to 4.5 for the coarse grid (see the dashed line without symbols on Figures 4.1 and 4.2) showed that the overall grid resolution was the driving factor in obtaining realistic results. Clearly a refined grid is necessary to handle the large gradients in flow properties present in this flowfield. The other property plots for these runs can be found in Section 4 of Appendix A.

#### 4.3 *Frozen Versus Finite Rate*

Frozen and finite rate flow cases for both the isolated and combined nozzles were studied to determine the effect of chemistry on

the nozzle flowfield. The nonuniform chemistry profile at the inlet immediately undergoes a severe drop in pressure and temperature resulting from the expansion around the circular arc (A-B in Figure 3.1). This has the effect of driving all reaction rates towards zero. This is demonstrated in Figures 4.3 and 4.4, where the two curves in each figure are virtually indistinguishable. This means that for the inlet conditions and geometry used in this study, the flow is basically frozen. This result held for all cases ran. The remainder of the property plots for the uniform flow in the isolated nozzle and for the nonuniform flow in the combined nozzle can be found in section 1 of Appendix A. For the remainder of this discussion, only the finite rate results will be used, keeping in mind that the frozen results are virtually identical.

#### *4.4 Isolated Nozzle Results*

Throughout the following discussion, the points on Figure 3.1 (A through J and O) will be used to reference various parts of the nozzle geometry. Figures 4.5 and 4.6 show the nozzle and cowl wall pressures for uniform and nonuniform flow for the finite rate, isolated nozzle. The expansion wave from the circular arc section of the nozzle wall (A-B) reaches the cowl wall at approximately the same position for both the uniform and nonuniform flow. This can be seen in the sudden drop of cowl pressures in Figure 4.6. The change in wall curvature just after the parabolic wall attachment point, B, generates compression waves which eventually coalesce into a shock. As can be seen in Figure 4.5, the compression for the nonuniform case is stronger than that of the uniform case. This is due to the expansion waves from the nozzle wall

circular arc, A-B, reflecting off of the nonuniformities in the flowfield in the form of additional compression waves. The reflections of the expansion waves generated by the nozzle wall circular arc from the cowl wall dominate the wall recompression and cause the nozzle wall pressure to start dropping for both the nonuniform and uniform cases at  $X/h$ 's of 3.5 and 10.5, respectively. The nozzle wall pressure for the nonuniform case starts dropping sooner than for the uniform case due to additional expansion waves which are generated by reflections of the nozzle-wall-generated compression waves from the nonuniformities in the flowfield. The nonuniform pressure drops further than the uniform pressure because of these same additional expansion waves. The influence of the nonuniformities becomes negligible at about an  $X/h$  of 50.0.

Figure 4.6 shows a pressure rise on the cowl wall for the nonuniform flow case at an  $X/h$  of approximately 57.0. This same pressure rise occurs on the cowl wall for the uniform flow case at an  $X/h$  of 70.0. This is due to the shock wave generated by the nozzle wall hitting the cowl wall sooner for the nonuniform flow than for the uniform flow. This effect is shown more clearly in Figures 4.7 and 4.8, which are pressure contour plots of these two cases. The bending of the shock wave in the contour plot for uniform flow is due to interactions between the shock and the nozzle-wall-generated expansion waves reflecting off the cowl surface. The bending of the shock in the nonuniform case is more the product of direct interaction with the nonuniformities in the flow. The interaction of the shock wave with the reflected expansion waves for the nonuniform case has been weakened by passage of the expansion waves through the nonuniformities. This

results in a sharp bend in the shock wave for the nonuniform case as compared to the gradual bend of the shock wave for the uniform case. As can be seen from the two contour plots, the shock wave is hitting the cowl wall sooner for the nonuniform case than for the uniform case. The remainder of the property plots show the same trends as the pressure plots. These plots can be found in Section 3.1 of Appendix A. Uniform and nonuniform flow pressure contour plots for both frozen and finite rate flow for the isolated nozzles are contained in section 1 of Appendix B.

#### *4.5 Isolated Versus Combined Nozzle Plots*

Figures 4.9 and 4.10 are representative of the finite rate, uniform flow property plots for the isolated and combined nozzles. There are two major difference between the combined nozzle flow and the isolated nozzle flow. The first difference is the presence of expansion waves in the combined nozzle flow that are generated from the circular arc in the cowl surface at point E. The second difference is the presence of expansion waves caused by the external flow interacting with the internal flow at point F. These expansion waves intersect the nozzle wall at approximately  $X/h = 50.0$  as shown by the drop in temperature for the combined nozzle in Figure 4.9 and the rise in X-component wall velocity in Figure 4.10. Figures 4.11 and 4.12 are the equivalent nonuniform flow property plots. These figures also show a drop in temperature and increase in X-component velocity indicating the presence of expansion waves from the cowl and the external flow, but they are much weaker. This is shown in Figure 4.12 where the X-component velocity for the combined nozzle is barely changed from that

of the isolated nozzle. This is due to the expansion waves from the cowl circular arc (point E on Figure 3.1) and the expansion waves from the internal/external flow interaction (point F on Figure 3.1) encountering the shock wave from the compression on the nozzle wall at a steeper angle than for the uniform case. The remainder of the property plots for these cases show similar trends and can be found in Section 2 of Appendix A.

#### 4.6 Combined Nozzle

Figures 4.13 and 4.14 illustrate the nozzle and cowl wall pressures, respectively, for both uniform and nonuniform finite rate flow in the combined nozzle. Note that the scale on the X-axis of the cowl wall pressure plot is larger than that of the nozzle wall pressure plot. The nozzle pressure plot, Figure 4.13, is virtually identical to the isolated case from Section 4.3, Figure 4.3, and thus will not be rediscussed here. The cowl pressure plot, Figure 4.14, clearly shows the initially undisturbed flow accelerating because of the expansion waves generated by the nozzle wall circular arc (A-B). The initial expansion point for the nonuniform flow is slightly earlier than that for the uniform flow. This is most likely due to the expansion waves from the nozzle wall being bent slightly by interaction with the flow nonuniformities. At an  $X/h$  of approximately 8.5 the cowl wall becomes a circular arc around which the flow expands (see point E of Figure 3.1). This is manifested as another sharp drop in the cowl wall pressure which then levels into quasi-uniform flow along the 3rd section of the cowl surface, E-F. The remaining property plots are found in Section 3.2 of Appendix A.

Figures 4.15 and 4.16 are pressure contour plots for the finite rate, combined nozzle for uniform and nonuniform flow, respectively. These plots are divided into two zones for the plotting routine. The first zone is internal nozzle flow, with 101 grid points in the transverse direction of the nozzle (i.e. along the line A-O). The second zone is combined flow, with 149 grid points from the nozzle surface to the external computational boundary (i.e. along the line connecting points I and F and the nozzle wall). The shock wave generated from the compression on the nozzle wall exhibits the same behavior as the isolated case for each flowfield. Again, the nonuniform flow shock bends away from the nozzle wall at a sharp angle while the uniform flow shock bends away from the nozzle wall more gradually. An expansion wave is generated by the pressure difference between the internal and external flow at point F and can be seen coming down through the shock wave towards the nozzle wall. At the same time, a shock is generated which goes up into the external flow. This effect can be seen in the upper left corner of zone 2. The shock wave generated by the nozzle wall for the nonuniform flow case bends the expansion waves toward the nozzle wall more than the uniform flow shock wave does due to the larger angle of intersection between the nonuniform shock and the external compression wave. The region just past the intersection of the shock wave from the nozzle wall and the expansion waves from the cowl and the external flow is a region of quasi-simple wave flow. This region is bounded above first by the shock wave from the nozzle wall and then by additional expansion waves created by the reflection of the shock wave from the shear layer. These additional expansion waves never intersect the nozzle wall and thus do not affect

any of the nozzle wall properties.

#### 4.7 Thrust and Moment

The thrust calculated by SCHNOZ is the thrust produced by pressure on the diverging nozzle walls, hereafter referred to as wall thrust, and does not include momentum thrust. Figure 4.17 is the cumulative wall thrust plot for the isolated nozzle, finite rate flow cases. The nonuniform flow produces a higher wall thrust than the uniform flow for all nozzle lengths longer than  $X/h$  of 7.0. The increase in thrust for the nonuniform case relative to the thrust for the uniform case is due to the higher pressure rise on the nozzle wall produced by the expansion waves from the nozzle wall reflecting off the nonuniformities in the flow as compression waves as was shown in Figure 4.5. The difference in thrust between the uniform and nonuniform flow is close to constant past  $X/h$  of 25.

The total moment produced in the isolated nozzle is the sum of the moment on the nozzle wall (A-B-C) and the moment on the cowl wall (O-D-E-F), with the origin at point A on Figure 3.1. As is shown in Figure 18, the total moment is positive for both the uniform and nonuniform flowfields. This equates to a pitch-down moment for the hypersonic vehicle (SCHNOZ calculates the sign of the pitching moment as if the nozzle being run in the study is inverted back to "real world" geometry). The moment produced by the nonuniform flow at the end of the nozzle is significantly less than that of the uniform flow. Both flows start out at the beginning of the nozzle with negative moments due to the higher pressure on the cowl than on the nozzle (recall the flow near the nozzle wall is expanding due to the circular arc section of the

nozzle, A-B on Figure 3.1). However, the recompression on the nozzle wall due to the changing curvature combined with the expansion waves from the nozzle wall intersecting the cowl wall serves to increase the moment relative to the moment values at earlier  $X/h$  stations. The moment for the nonuniform flow is higher due to the higher pressure rise on the nozzle wall as shown in Figure 4.5. From an  $X/h$  of approximately 14.0 on, the moment of the uniform flow starts to overtake the moment of the nonuniform flow. This is due to the slight difference in nozzle wall pressure between the uniform flow and nonuniform flow cases becoming more effective at producing pitching moment as the moment arm increases. This is apparent out to about  $X/h = 50.0$  where the pressures are approximately equivalent and the slopes of the two lines become about equal (See Figures 4.5 and 4.6). Both moments eventually level out, the uniform flow at about  $X/h = 70.0$  and the nonuniform flow at about  $X/h = 52.0$ . These locations coincide with the locations of the intersection between the recompression shock wave and the cowl wall as shown in Figures 4.7 and 4.8. This shock wave and the resulting reflected shock wave cause a pressure increase on the cowl wall which is shown in Figure 4.6, making it almost the same as the pressure on the nozzle wall.

The combined nozzle thrust plots are presented in Figure 4.19. The thrust plots are essentially identical to those for the isolated nozzle. The reason for this is that the thrust contributions from the cowls on the isolated and combined nozzles are zero and insignificant, respectively. The pressure on the isolated nozzle cowl wall contributes nothing to the thrust because the wall is parallel to the thrust direction. The cowl wall on the combined nozzle has only a short



section (the circular arc at point E and the straight section from E to F on Figure 3.1) which contributes to the thrust and the pressures on this surface are low and approximately the same for both the uniform and nonuniform flows (see Figure 4.14). Figure 4.20 shows a comparison of the thrust for the isolated versus combined nozzles for the nonuniform case. The additional thrust produced by the cowl in the combined nozzle is offset eventually by the expansion waves from the cowl and from the pressure difference between the external flow and the internal flow which lowers the wall pressure. Thus, the isolated nozzle ends up producing slightly higher thrust than the combined nozzle for these flow conditions and geometry.

The moment plots for the combined nozzle are presented in Figure 4.21. The trends here are again the same as for the isolated nozzle for the first half of the nozzle. The combined nozzle does not have the abrupt leveling off of moment that the isolated nozzle does in the second half because there is no cowl wall for the shock wave originating from the nozzle wall to hit. The moment plot has a higher slope for the combined case than for the isolated case due to the lack of cowl wall on the upper side of the nozzle. Figure 4.22 shows a comparison of the moments produced in the isolated and combined nozzles for the nonuniform case. The moments for these nozzles are about the same until an  $X/h$  of 8.5, where the combined nozzle cowl wall becomes a circular arc at point E in Figure 3.1. The expansion on the cowl wall around this circular arc causes a decrease in pressure on the cowl wall, resulting in a higher moment for the combined nozzle than for the isolated nozzle. The abrupt ending of the cowl at  $X/h = 10.0$  causes the moment for the combined nozzle to be much higher than that for the isolated nozzle

because there is no longer a negative moment being produced by pressure on the cowl wall.

The results for total thrust and moment for all eight cases are presented in Table 4.2.

Table 4.2. Total Thrust and Moment for All Cases

Case	Thrust (lbf)	Moment (ft-lb)
1	$5.52 \times 10^3$	$2.67 \times 10^5$
2	$5.37 \times 10^3$	$3.57 \times 10^5$
3	$5.76 \times 10^3$	$1.96 \times 10^5$
4	$5.60 \times 10^3$	$3.42 \times 10^5$
5	$5.52 \times 10^3$	$2.67 \times 10^5$
6	$5.37 \times 10^3$	$3.57 \times 10^5$
7	$5.76 \times 10^3$	$1.96 \times 10^5$
8	$5.61 \times 10^3$	$3.43 \times 10^5$

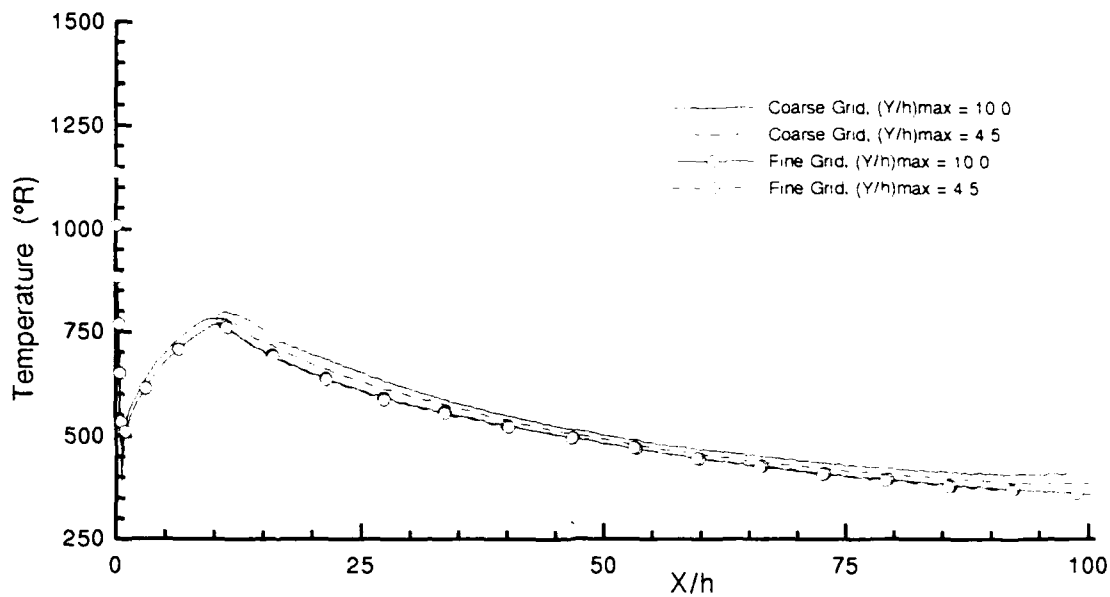


Figure 4.1. Nozzle Wall Temperatures for Grid and  $(Y/h)_{\max}$  Changes for Uniform, Finite Rate Flow in the Combined Nozzle

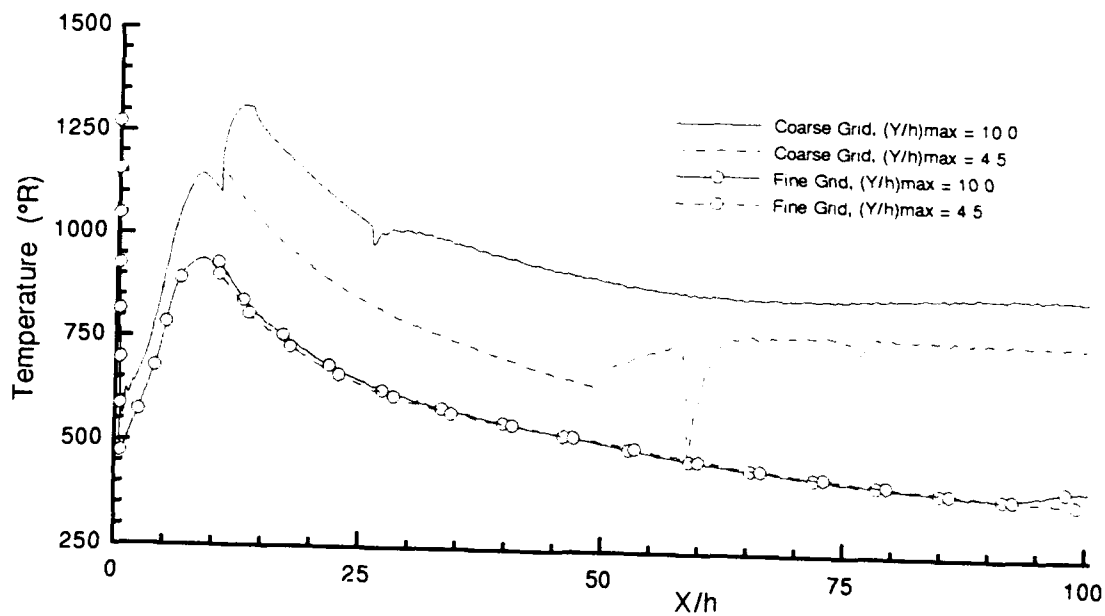
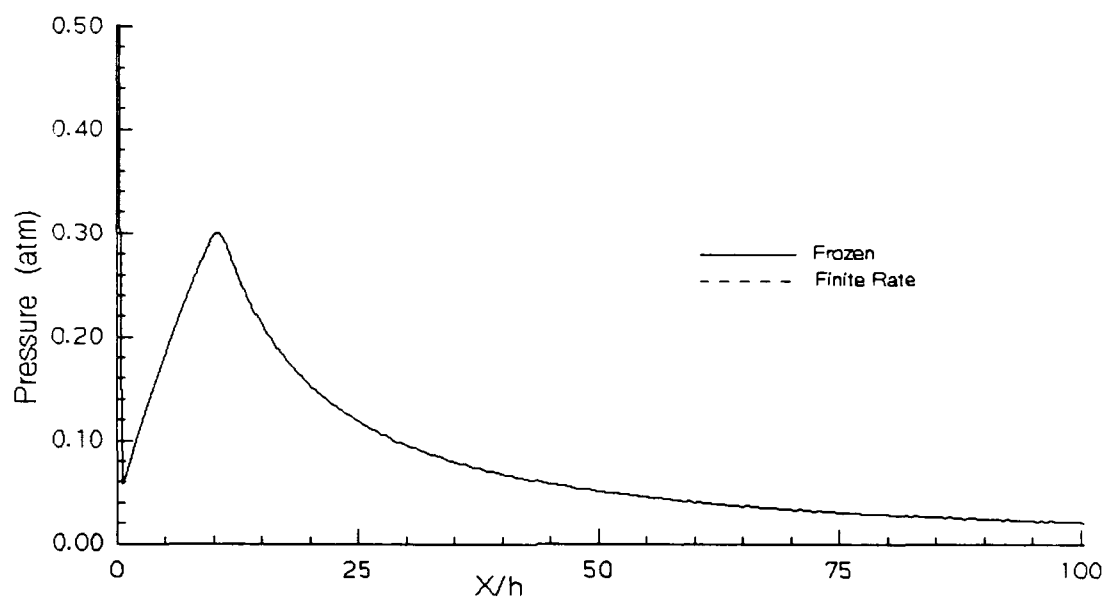
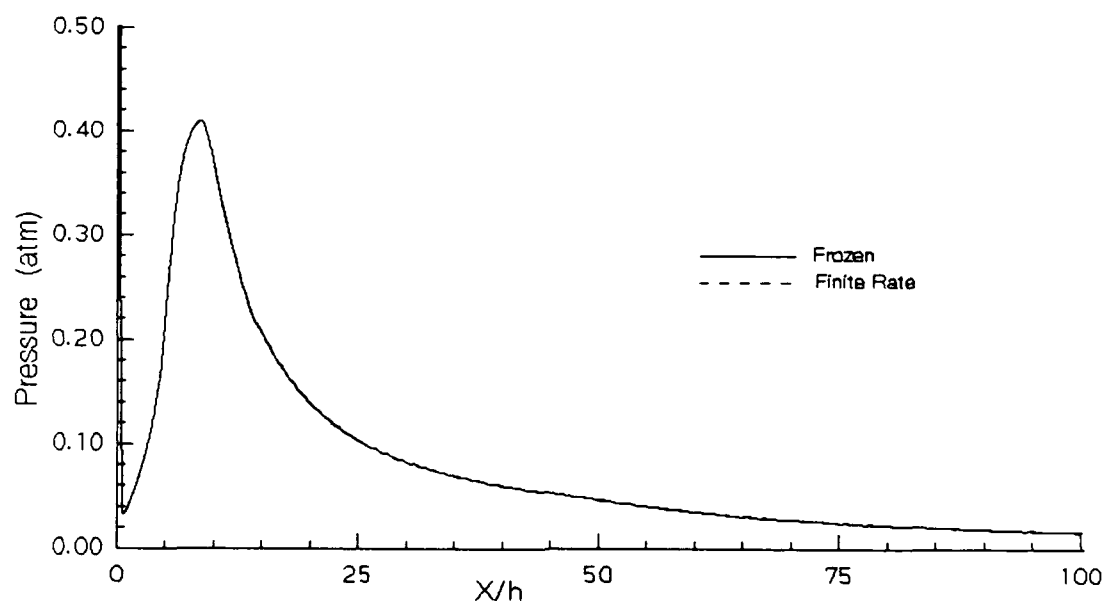


Figure 4.2. Nozzle Wall Temperatures for Grid and  $(Y/h)_{\max}$  Changes for Nonuniform, Finite Rate Flow in the Combined Nozzle



**Figure 4.3.** Nozzle Wall Pressures for Frozen and Finite Rate Flow in the Isolated Nozzle



**Figure 4.4.** Nozzle Wall Pressures for Frozen and Finite Rate Flow in the Combined Nozzle

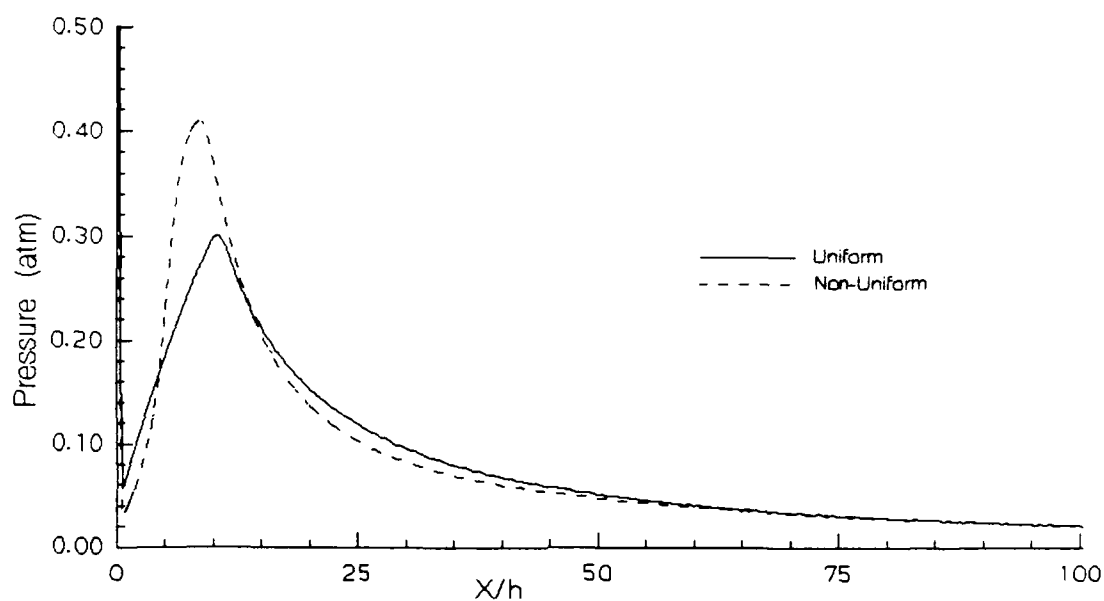


**Figure 4.5.** Nozzle Wall Pressures for Uniform and Nonuniform Flow for the Finite Rate, Isolated Nozzle

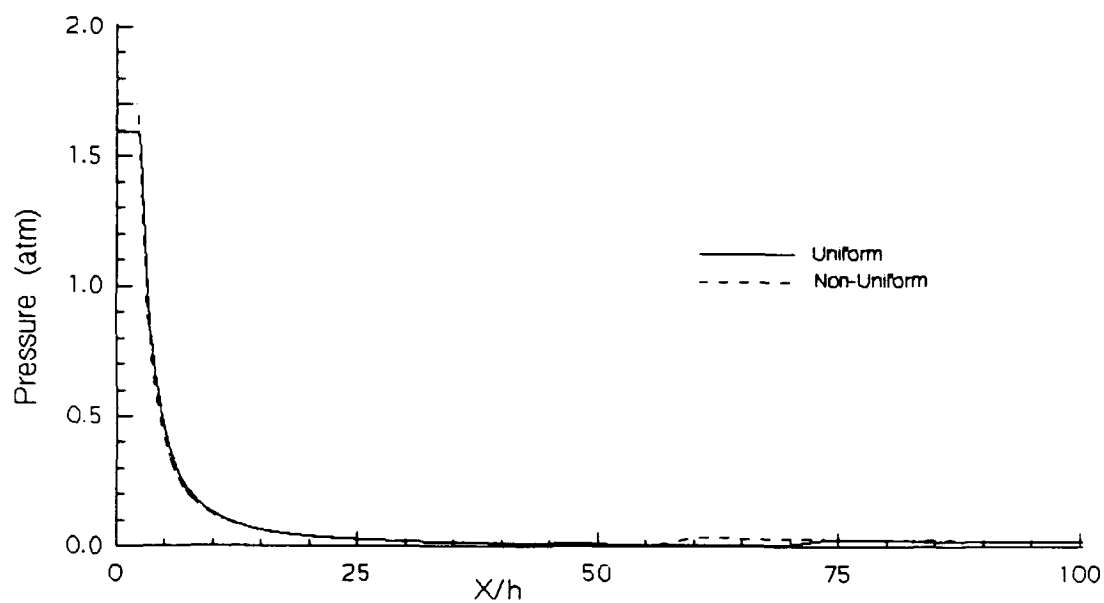


**Figure 4.6.** Cowl Wall Pressures for Uniform and Nonuniform Flow for the Finite Rate, Isolated Nozzle

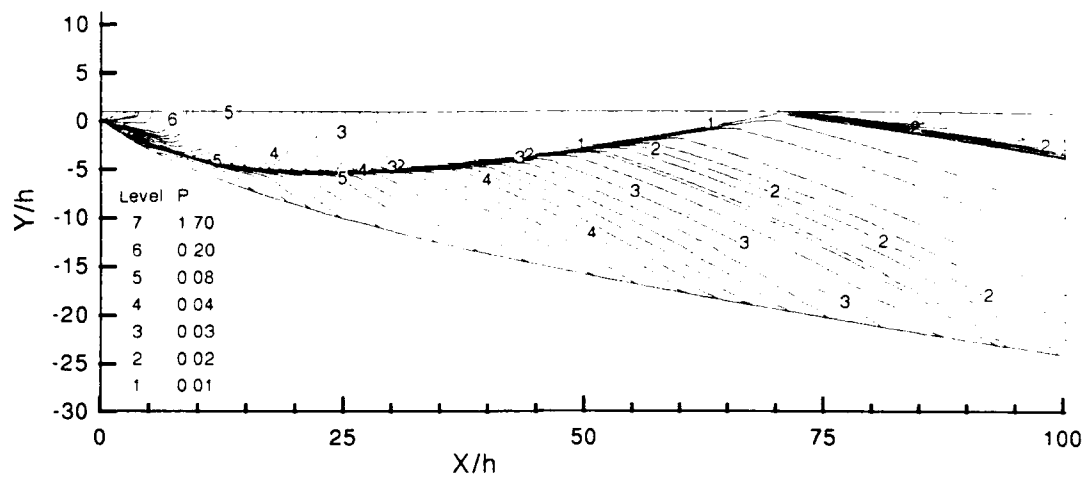


Figure 4.7. Pressure Contour Plot (atm) for Uniform, Finite Rate Flow in an Isolated Nozzle

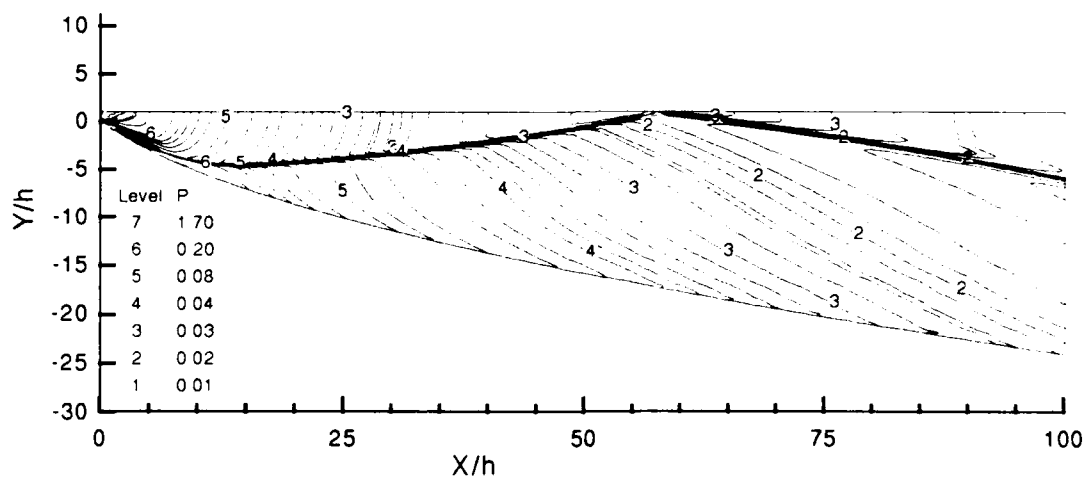
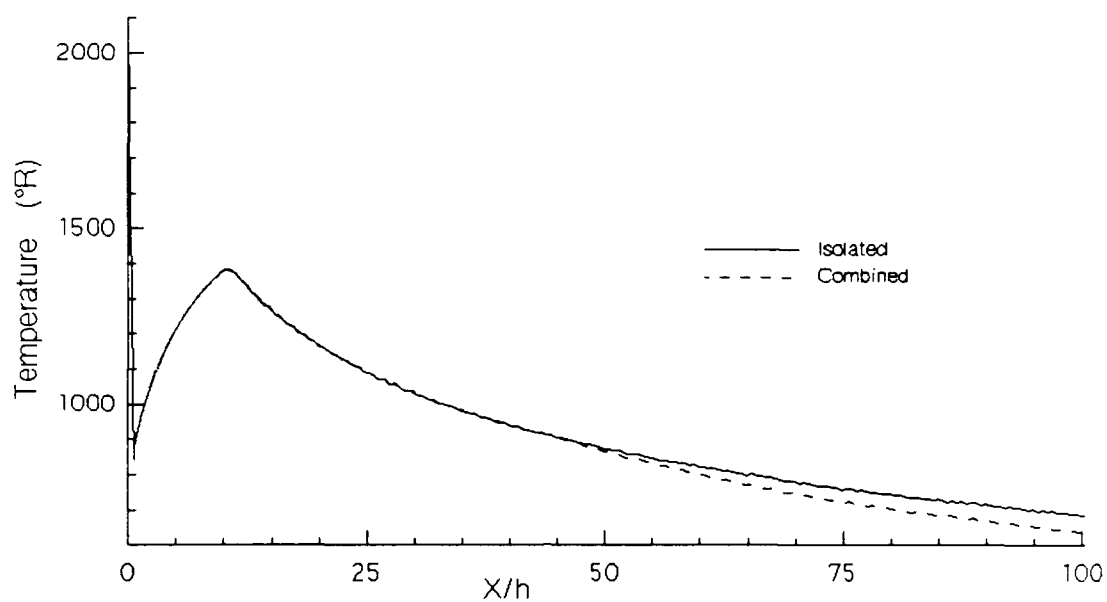
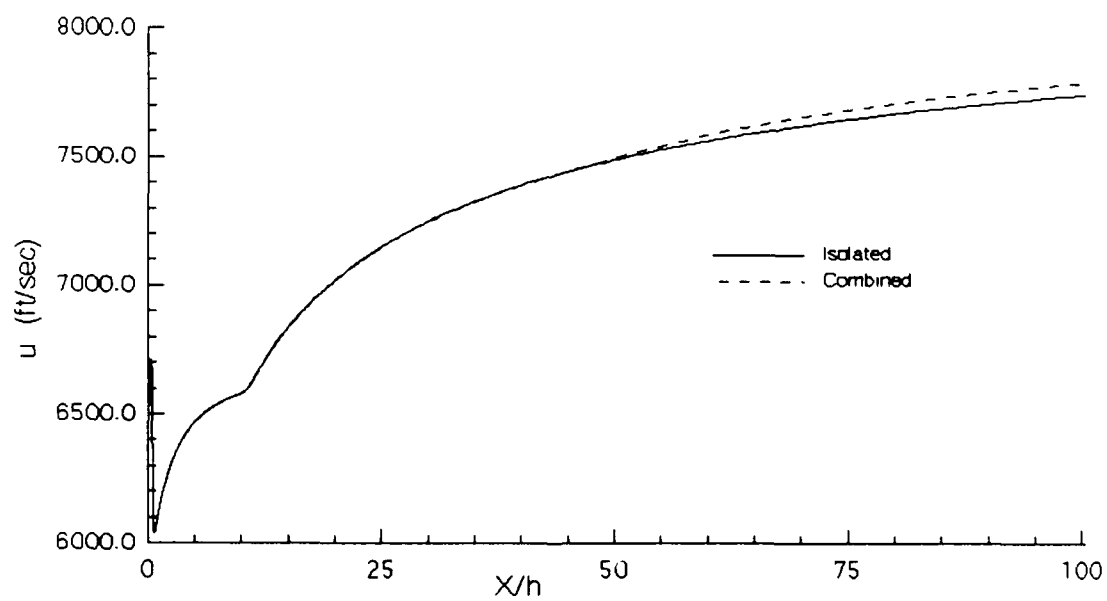


Figure 4.8. Pressure Contour Plot (atm) for Nonuniform, Finite Rate Flow in an Isolated Nozzle



**Figure 4.9.** Nozzle Wall Temperature for Finite Rate, Uniform Flow for the Isolated and Combined Nozzles



**Figure 4.10.** Nozzle Wall X-Component Velocities for Finite Rate, Uniform Flow for the Isolated and Combined Nozzles

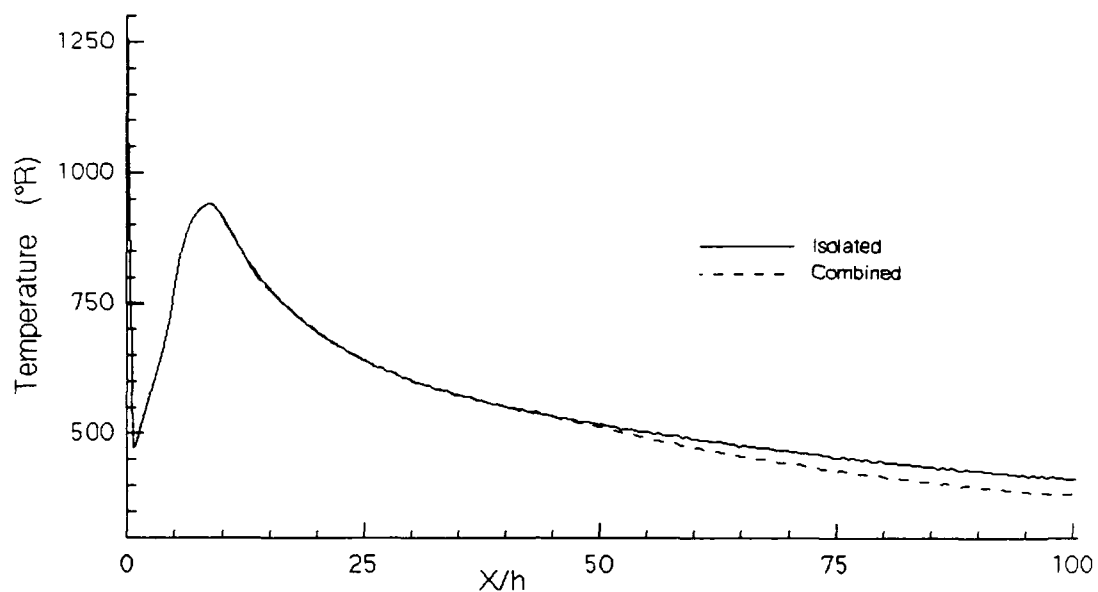


Figure 4.11. Nozzle Wall Temperatures for Finite Rate, Nonuniform Flow for the Isolated and Combined Nozzles

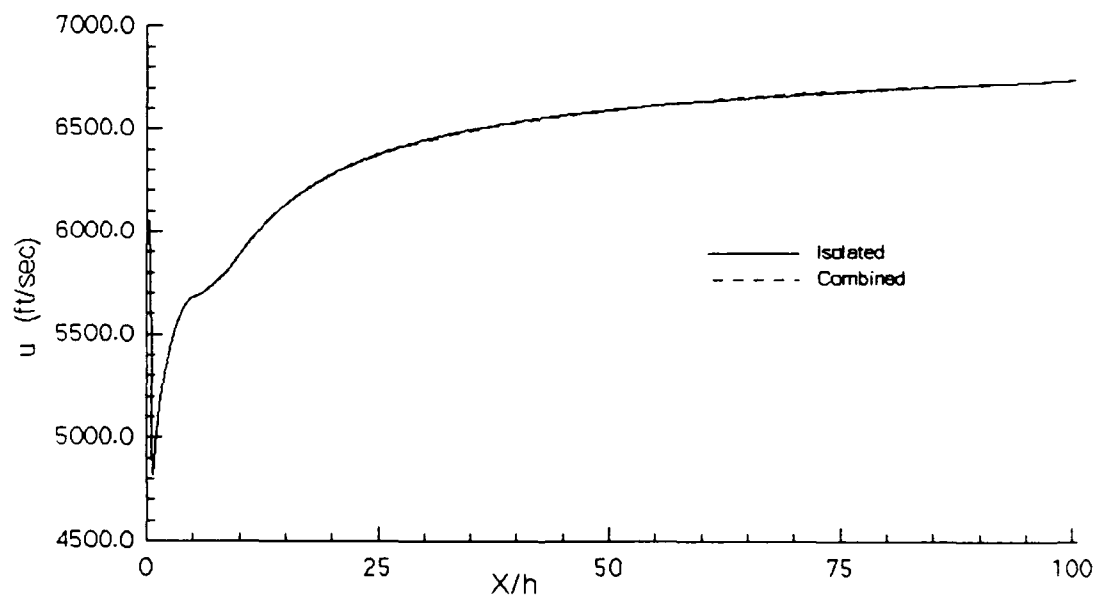
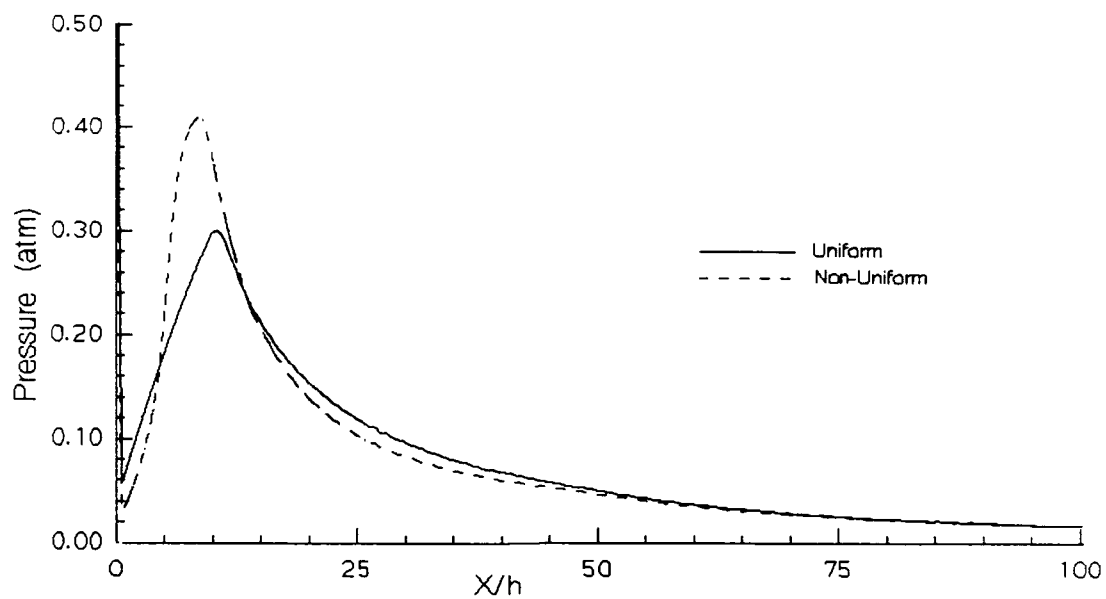
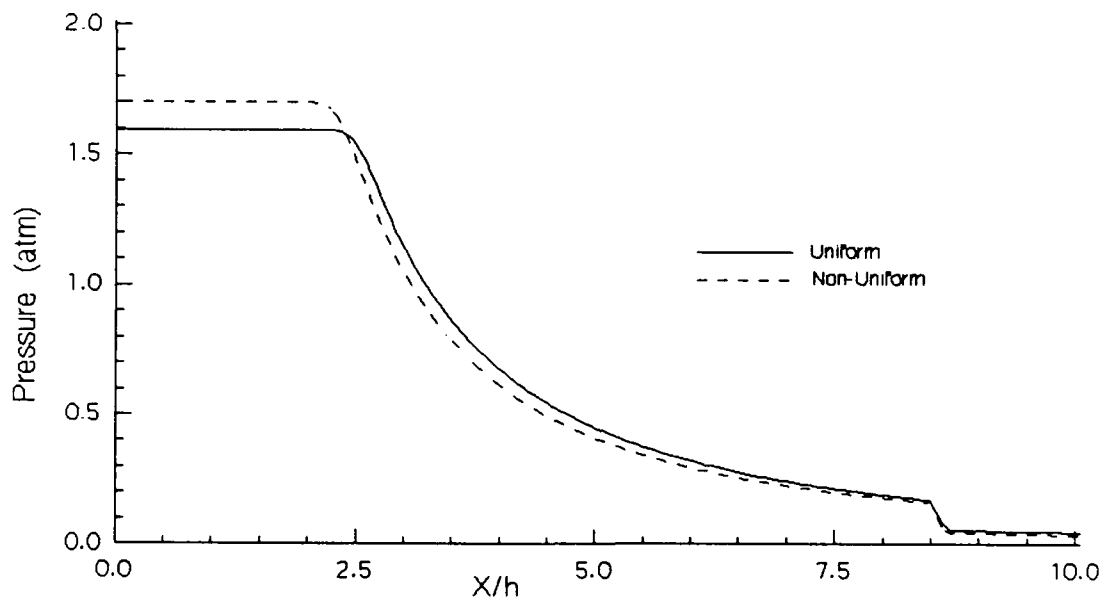


Figure 4.12. Nozzle Wall X-Component Velocities for Finite Rate, Nonuniform Flow for the Isolated and Combined Nozzles





**Figure 4.13.** Nozzle Wall Pressures for Uniform and Nonuniform Flow for the Finite Rate, Combined Nozzle



**Figure 4.14.** Cowl Wall Pressures for Uniform and Nonuniform Flow for the Finite Rate, Combined Nozzle

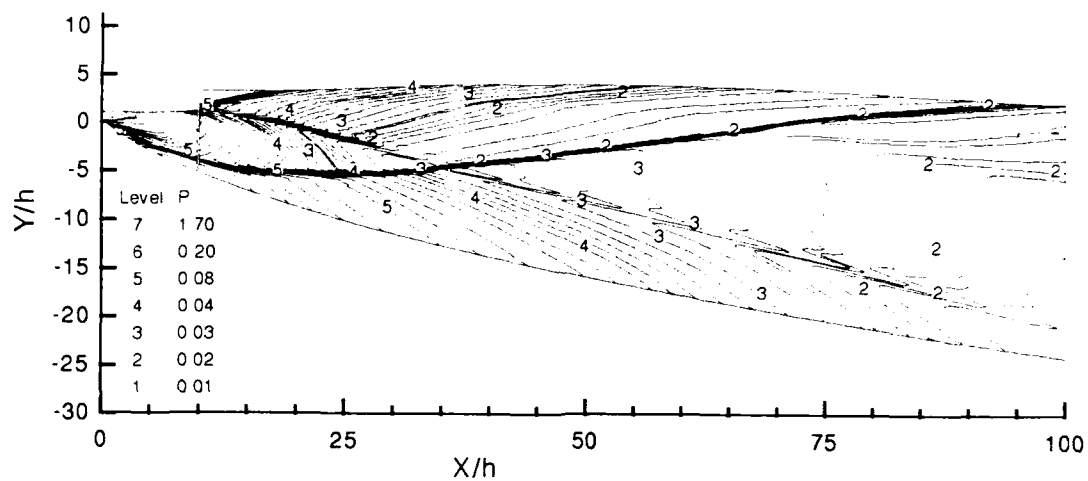


Figure 4.15. Pressure Contour Plot (atm) for Uniform, Finite Rate Flow in a Combined Nozzle

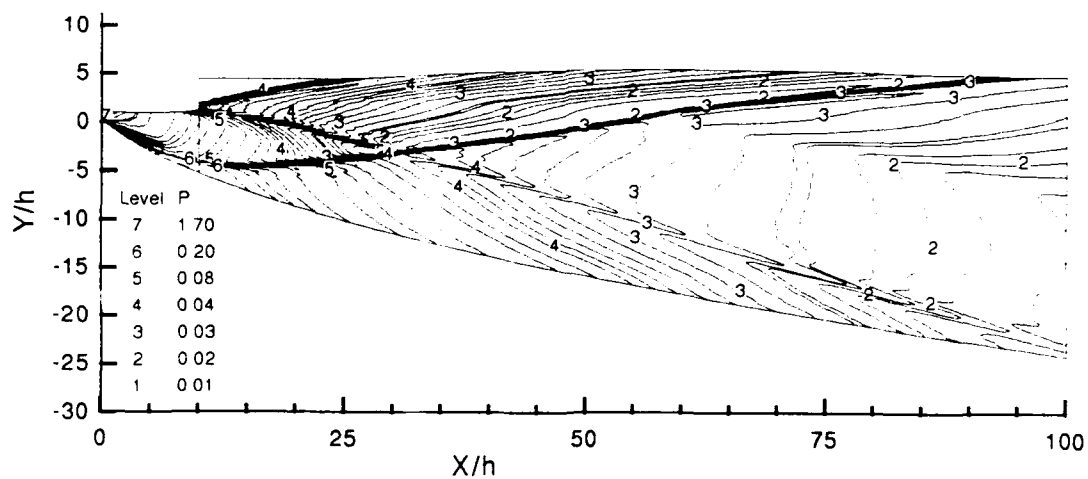


Figure 4.16. Pressure Contour Plot (atm) for Non-Uniform, Finite Rate Flow in a Combined Nozzle

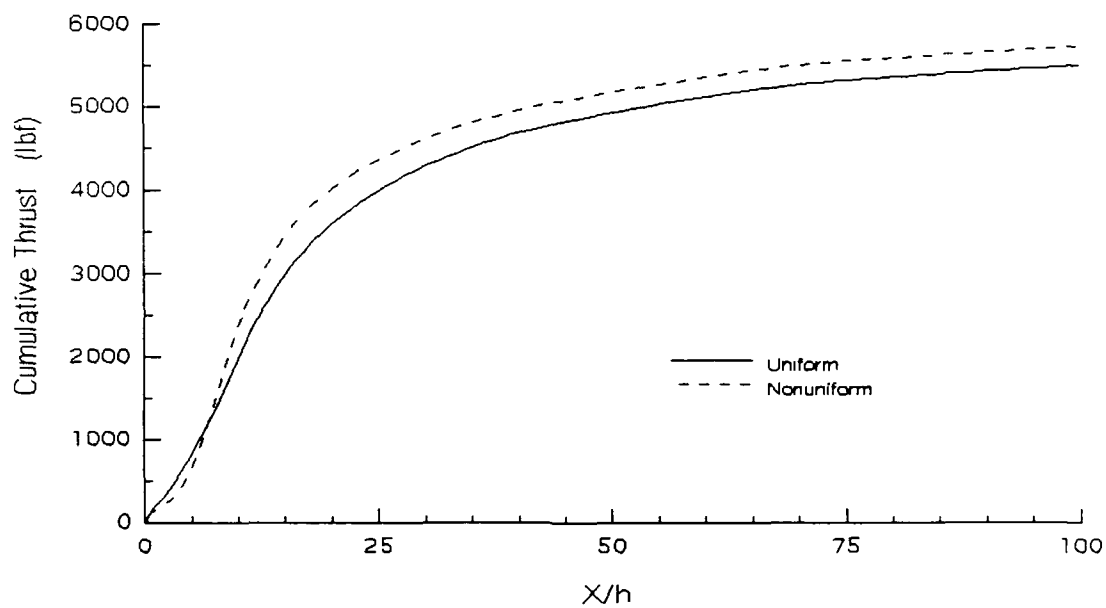


Figure 4.17. Cumulative Thrust Produced in the Finite Rate Isolated Nozzle for Uniform and Nonuniform Flow

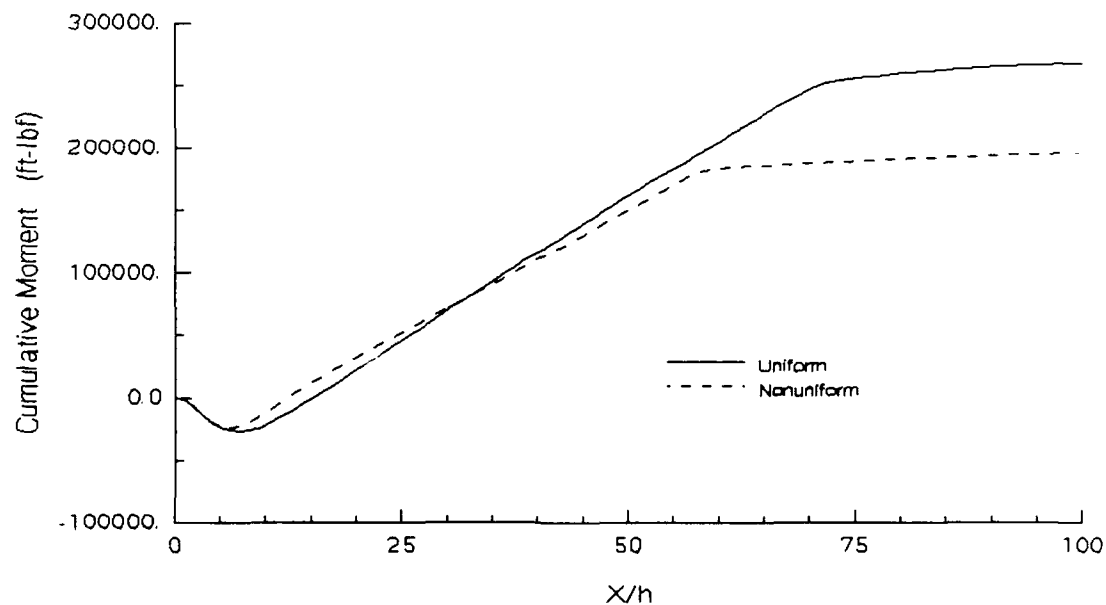
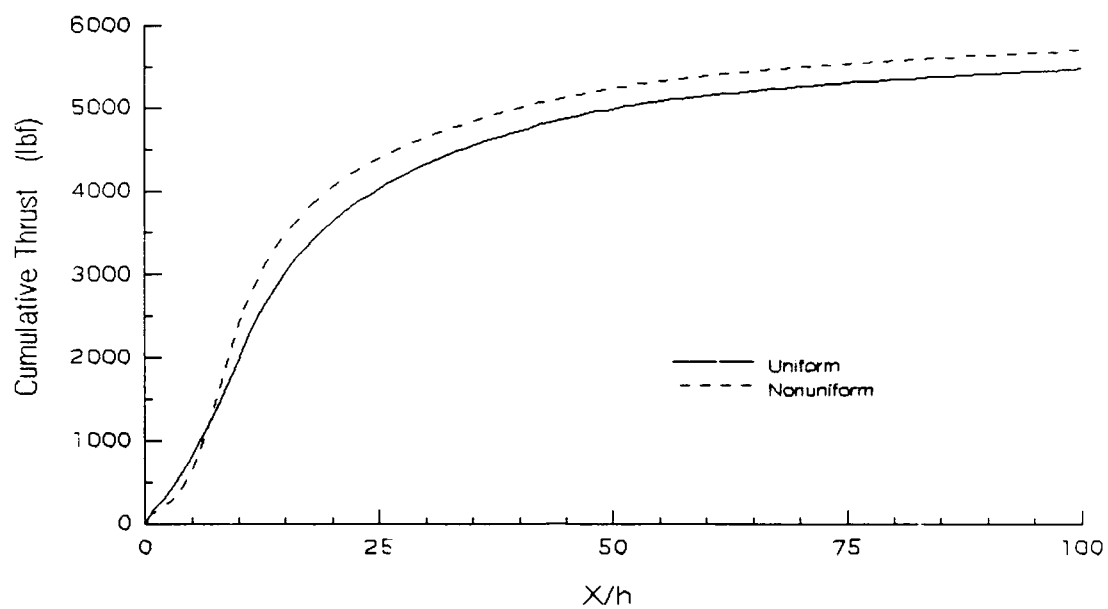
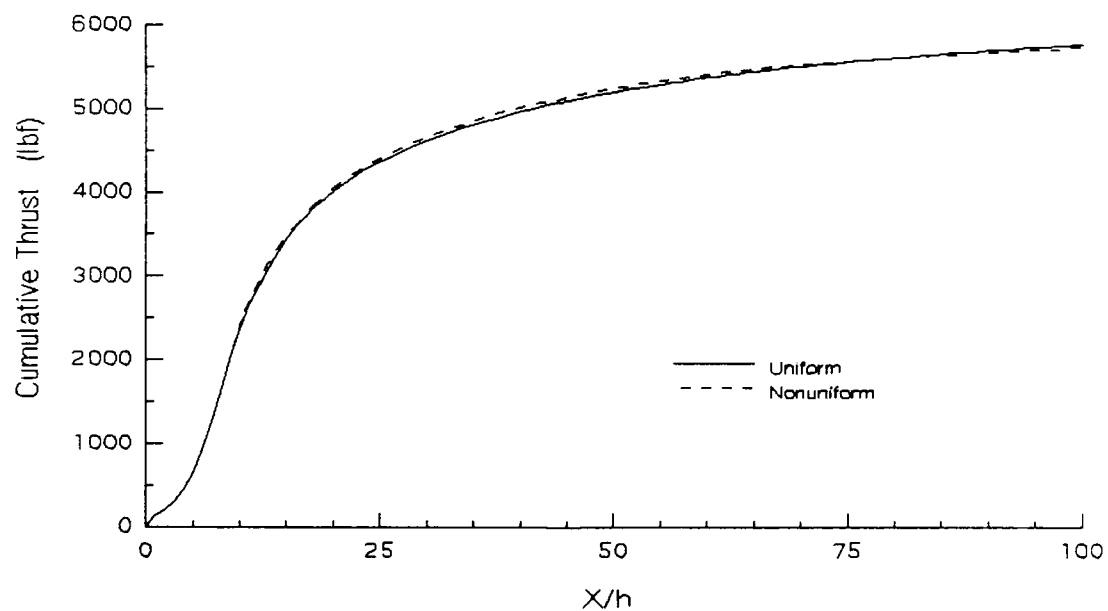


Figure 4.18. Cumulative Moment Produced in the Finite Rate, Isolated Nozzle for Uniform and Nonuniform Flow



**Figure 4.19.** Cumulative Thrust for the Finite Rate, Combined Nozzle for Uniform and Nonuniform Flow



**Figure 4.20.** Cumulative Thrust for Nonuniform Finite Rate Flow for the Isolated and Combined Nozzles

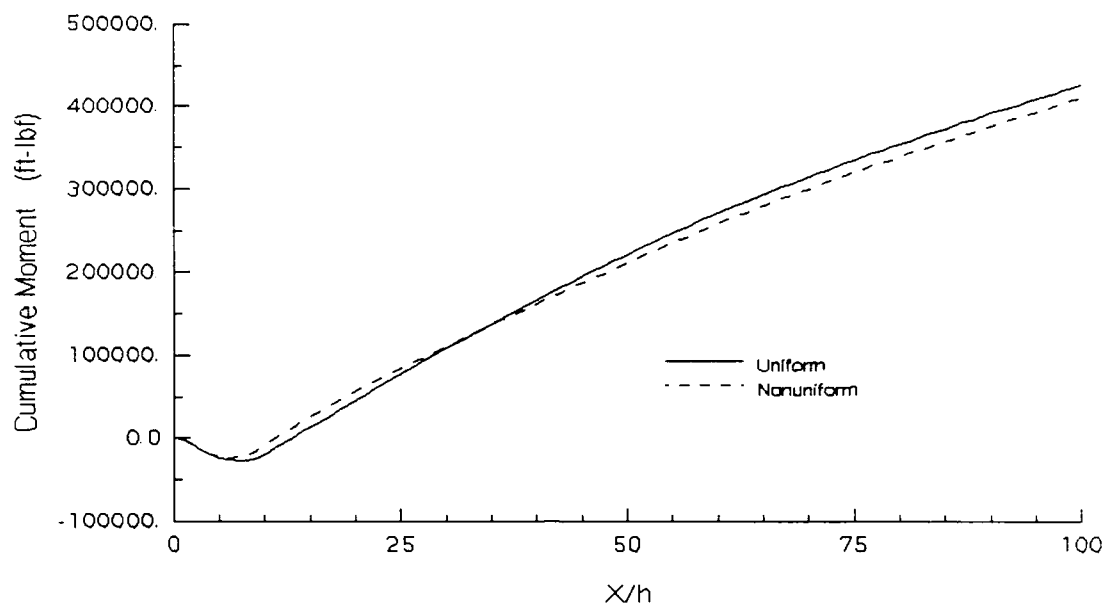


**Figure 4.21.** Cumulative Moment for the Finite Rate, Combined Nozzle for Uniform and Nonuniform Flow

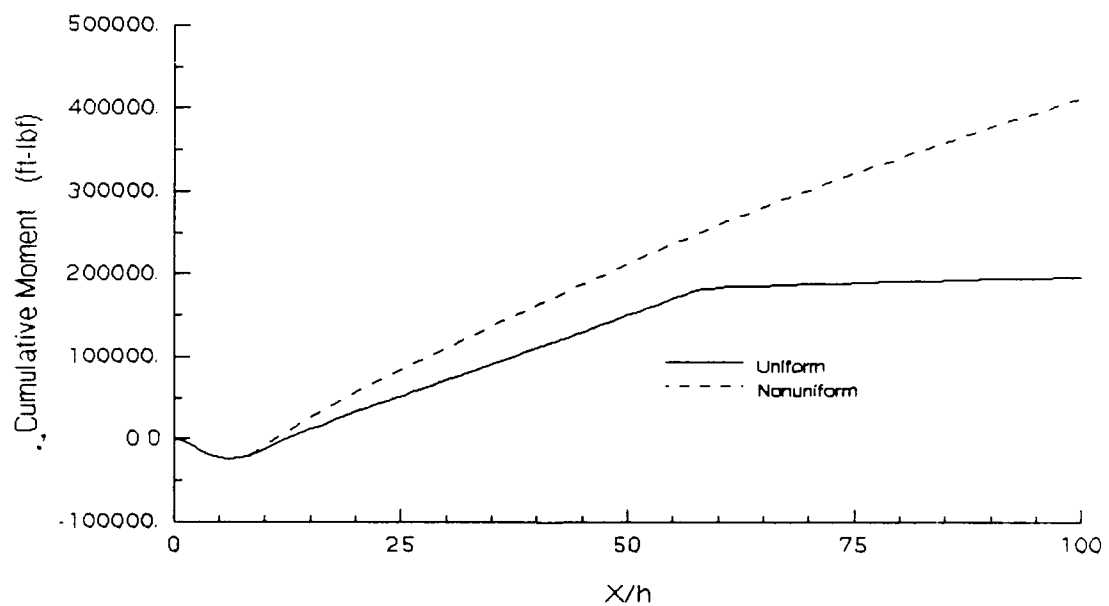


**Figure 4.22.** Cumulative Moment for Nonuniform, Finite Rate Flow for the Isolated and Combined Nozzle

## *V. Conclusions/Recommendations*

### *5.1 Conclusions*

The effects of nonuniformities in the flowfield were an increase in the overall vehicle thrust and a decrease in the overall vehicle moment for the inlet conditions and nozzle geometry used in this study. The increased thrust for the nonuniform case is due to higher compression on the nozzle wall caused by expansion waves from the nozzle wall reflecting off the nonuniformities in the flowfield as compression waves. The decreased moment for the nonuniform case is due to lower pressure on the nozzle wall than the uniform case for the aft portion of the nozzle combined with the longer moment arm canceling out the effect of the higher compression region. The lower pressure on the nozzle wall is the result of compression waves from the nozzle wall reflecting off the nonuniformities in the flowfield as expansion waves. Therefore, a vehicle flying at a trim point designed using uniform flow conditions would have a tendency to pitch up for the nonuniform flow conditions used in this study.

Comparisons were made between frozen flow and finite rate flow. The flow was shown to be essentially frozen at this inlet Mach number due to decreasing pressure and temperature. Therefore, realistic results can be obtained without spending the computational time on finite rate kinetics for this type of inlet conditions and nozzle geometry.

### *5.2 Recommendations*

According to the user manual (13) there is a later version of

SCHNOZ which should have been developed by now. This may or may not have a more refined grid available. If it does not, then future studies should be run on a modified version of SCHNOZ or on a completely different computer code.

Experimental nozzle data for comparisons to these runs are currently not available for unclassified use. When this data is declassified, new runs should be made to verify the results. Runs should also be made at different Mach numbers to establish the dependence of the pitching moment effects on Mach number. Also, if actual combustor data is available, runs should be made to verify the validity of the inlet conditions used here.

The nozzle inlet profile used here was symmetric across the inlet, typical of central fuel injection. Studies could also be made using a profile typical of a hydrogen cooling injection at the wall. A study varying fuel injection placement and angle should be made to determine the effect of these variations on vehicle pitching moment. If this effect is significant, then this might be an alternative means of balancing the vehicle moment rather than using trim tabs.

## Bibliography

- 1) Abbett, M.J., "Boundary Condition Calculation Procedures for Inviscid Supersonic Flowfields", *Proceedings of AIAA Computational Fluid Dynamics Conference*, July 1973, pp. 153-172
- 2) Anderson, John D. Jr., *Hypersonic and High Temperature Gas Dynamics*, New York: McGraw-Hill Book Company, 1989
- 3) Dash, Sanford M. and Wolf, David E., *Fully-Coupled Analysis of Jet Mixing Problems, Part I: Shock-Capturing Model*, SCIPVIS, NASA CR3761, Jan 1984
- 4) Doty, John H., *Performance Prediction and Design of Maximum Thrust Planar Supersonic Nozzles Using a Flux-Difference-Splitting Technique*, PHD Dissertation. Purdue University, Aug 1991
- 5) Doty, John H., Thompson, H. Doyle, and Hoffman, Joe D., *Optimum Thrust Airframe Integrated Scramjet Nozzles*, Paper #83, Seventh National Aero-Space Plane Technology Symposium, Oct 1989
- 6) Doty, John H., Thompson, H. Doyle, and Hoffman, Joe D., *Optimum Thrust Two-Dimensional NASP Nozzle Study*, NASP CR1069, Nov 1989
- 7) Gordon, Sanford and McBride, Bonnie J., *Computer Program for Calculation of Complex Chemical Equilibrium Compositions, Rocket Performance, Incident and Reflected Shocks, and Chapman-Jouguet Detonations*, NASA SP-273 (Interim Revision), March 1976
- 8) Harten, A. and Zwas, G., "Self-Adjusting Hybrid Schemes for Shock Capturing", *Journal of Computational Physics*, June 1972
- 9) Herring, David, *Design of an Optimum Thrust Nozzle for a Typical Hypersonic Trajectory Through Computational Analysis*, MS Thesis, AFIT/GAE/ENY/91D-?, School of Engineering, Air Force Institute of Technology (AU), Wright-Patterson AFB, OH (In Preparation)
- 10) Launder, B. and Spalding, D.B., *Lectures in Mathematical Models of Turbulence*, Academic Press, London, England, 1972
- 11) Sislian, J.P., *Equations of Motion and Two-Equation Turbulence Model for Plane or Axisymmetric Turbulent Flows in Body-Oriented Orthogonal Curvilinear coordinates and Mass-Averaged Dependent Variables*, NASA CR3025, Aug 1978
- 12) Thompson, H.D. and Hoffman, J.D., *Ramjet and Scramjet Nozzle Analysis*, Report PHD-89-1. PHD Technology, Inc., West Lafayette, IN, March 1990



- 13) Wolf, David E., Lee, Robert A. and Dash, Sanford M., *Analysis of Aerospace Vehicle Scramjet Propulsive Flowfields: 2D Nozzle Development -- Phase 1*, NASP CR1005, Aug 1987

## Appendix A. Line Plots

### A.1 Frozen vs. Finite Rate Plots

#### A.1.1 Isolated Nozzle

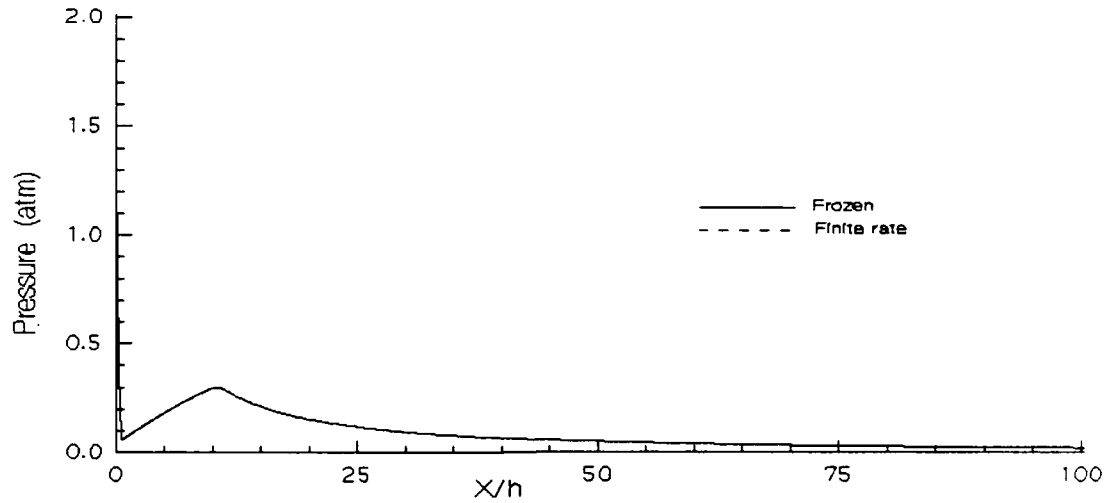


Figure A.1. Nozzle Wall Pressures for Frozen and Finite Rate, Uniform Flow in the Isolated Nozzle

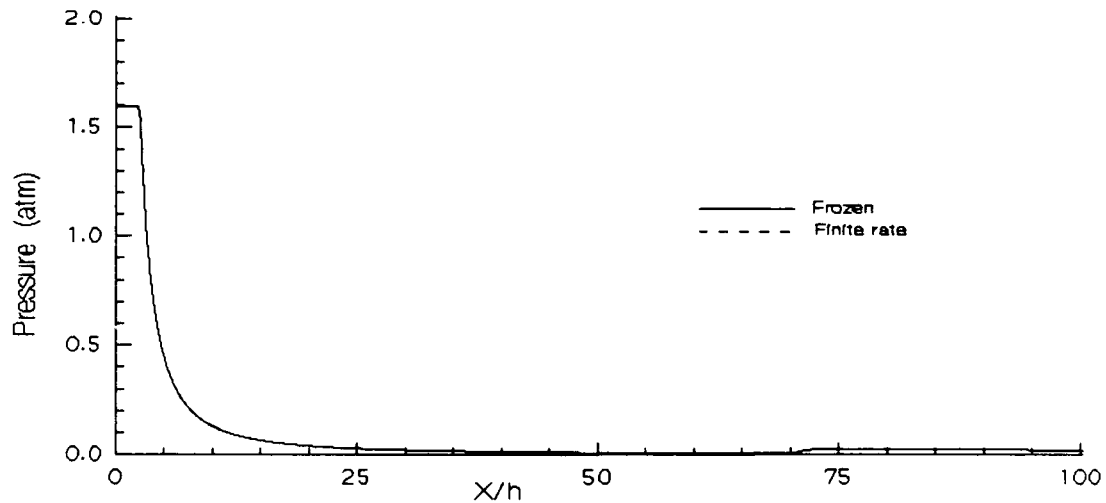


Figure A.2. Cowl Wall Pressures for Frozen and Finite Rate, Uniform Flow in an Isolated Nozzle

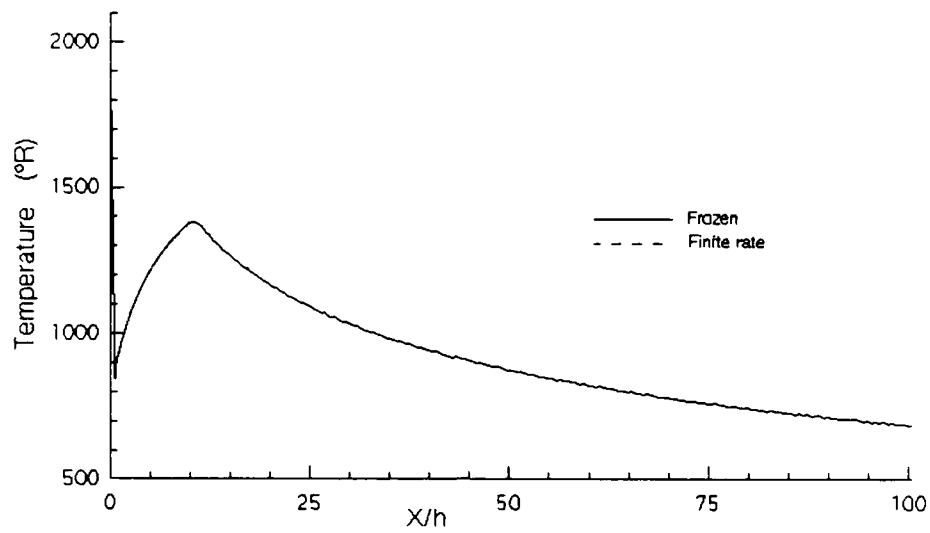


Figure A.3. Nozzle Wall Temperatures for Frozen and Finite Rate, Uniform Flows in the Isolated Nozzle

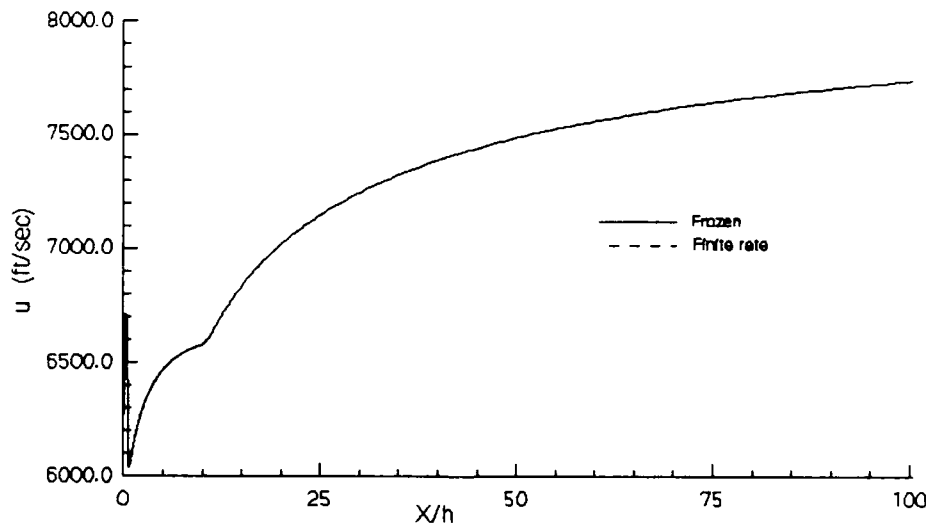


Figure A.4. Nozzle Wall X-Component Velocities for Frozen and Finite Rate, Uniform Flow in the Isolated Nozzle

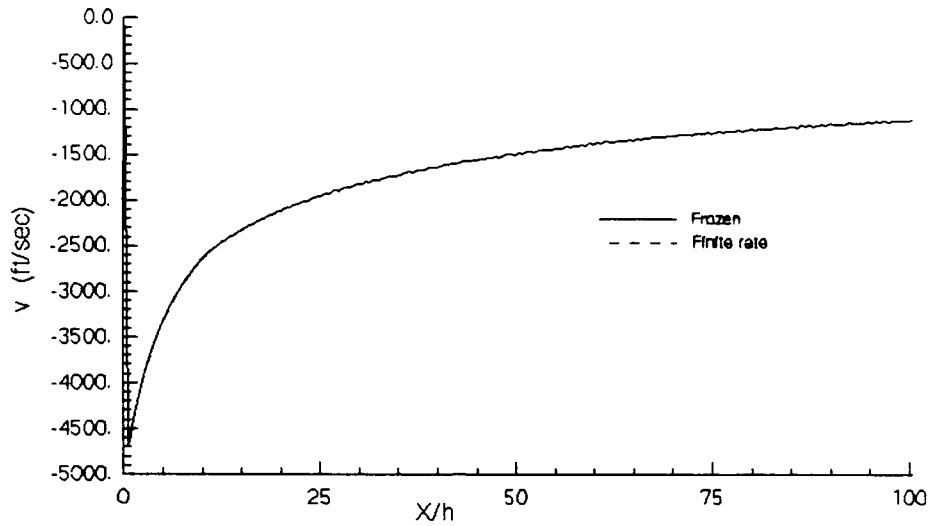


Figure A.5. Nozzle Wall Y-Component Velocities for Frozen and Finite Rate, Uniform Flow in the Isolated Nozzle

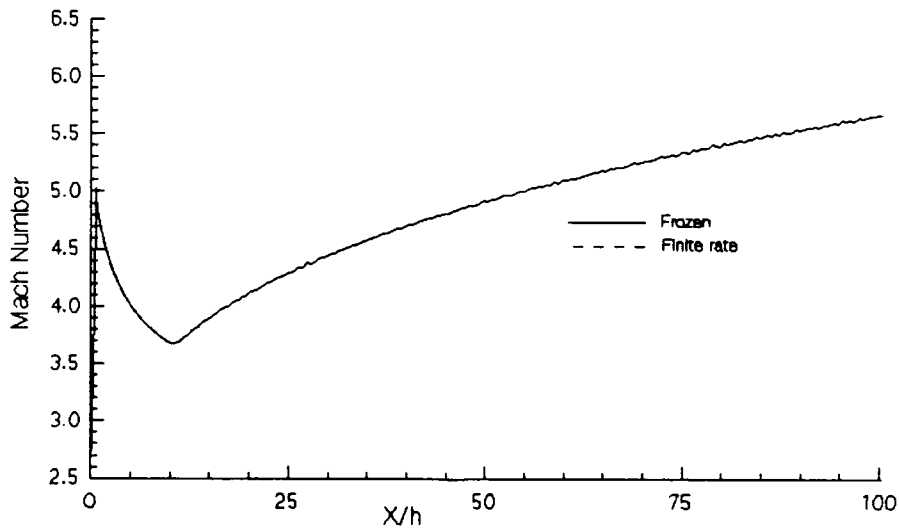
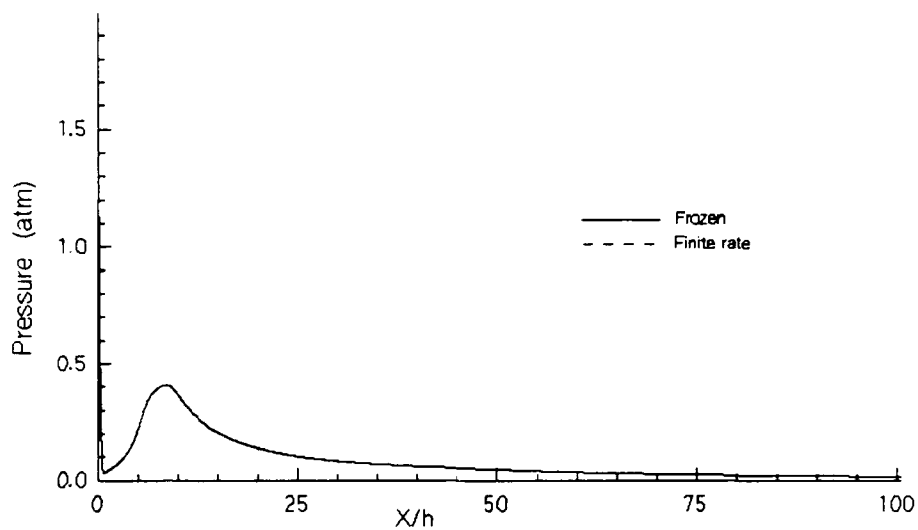
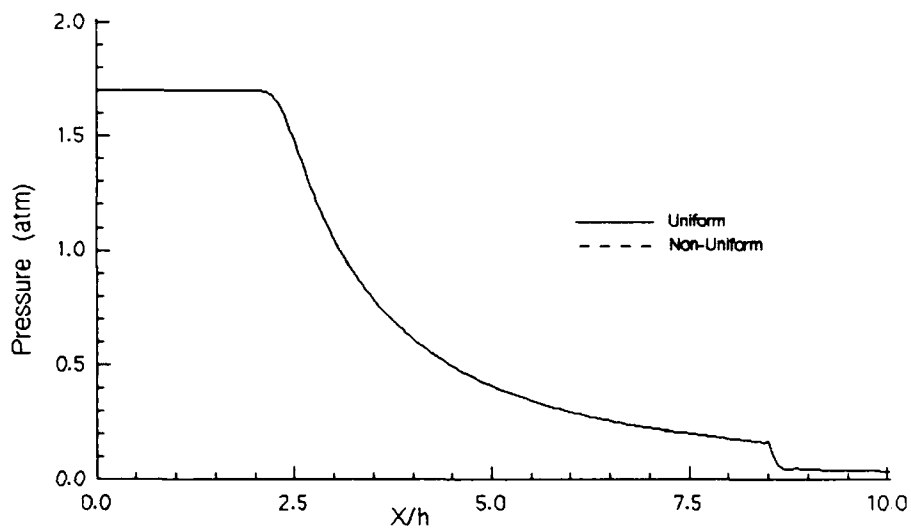


Figure A.6. Nozzle Wall Mach Numbers for Frozen and Finite Rate, Uniform Flow in the Isolated Nozzle

### A.1.2 Combined Nozzle



**Figure A.7.** Nozzle Wall Pressures for Frozen and Finite Rate, Nonuniform Flow in the Combined Nozzle



**Figure A.8.** Cowl Wall Pressures for Frozen and Finite Rate, Nonuniform Flow in the Combined Nozzle

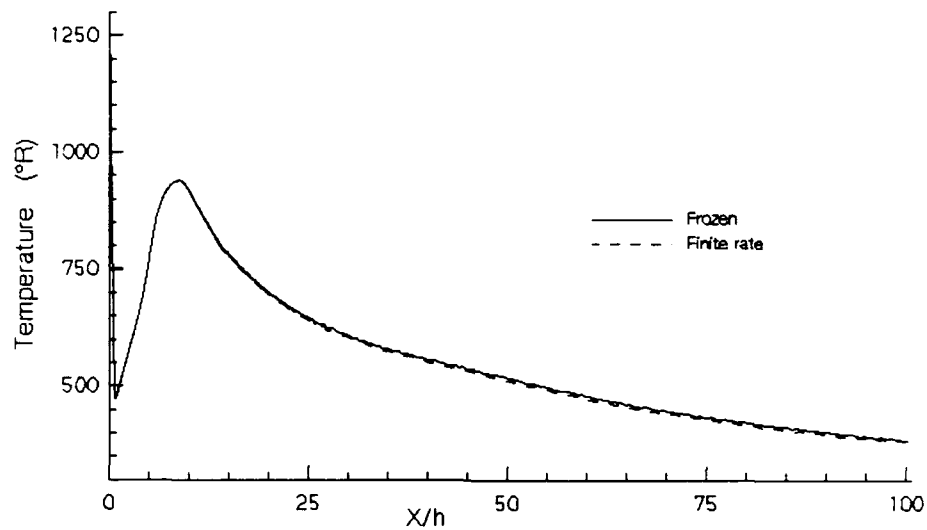


Figure A.9. Nozzle Wall Temperatures for Frozen and Finite Rate, Nonuniform Flow in the Combined Nozzle

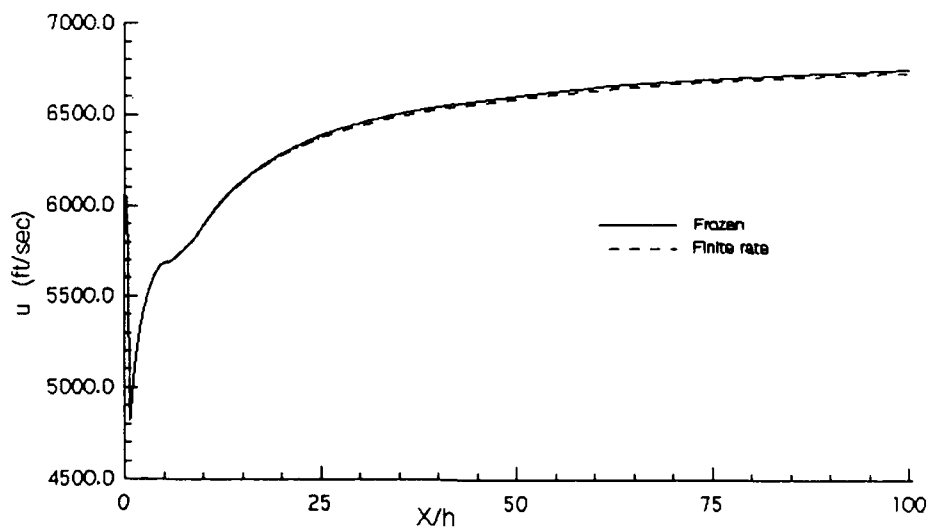


Figure A.10. Nozzle Wall X-Component Velocities for Frozen and Finite Rate, Nonuniform Flow in the Combined Nozzle

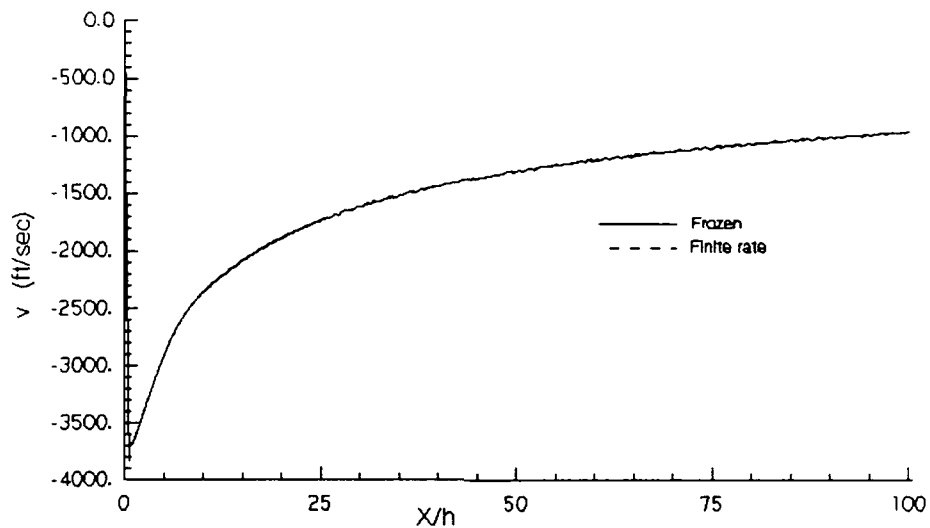


Figure A.11. Nozzle Wall Y-Component Velocities for Frozen and Finite Rate, Nonuniform Flow in the Combined Nozzle

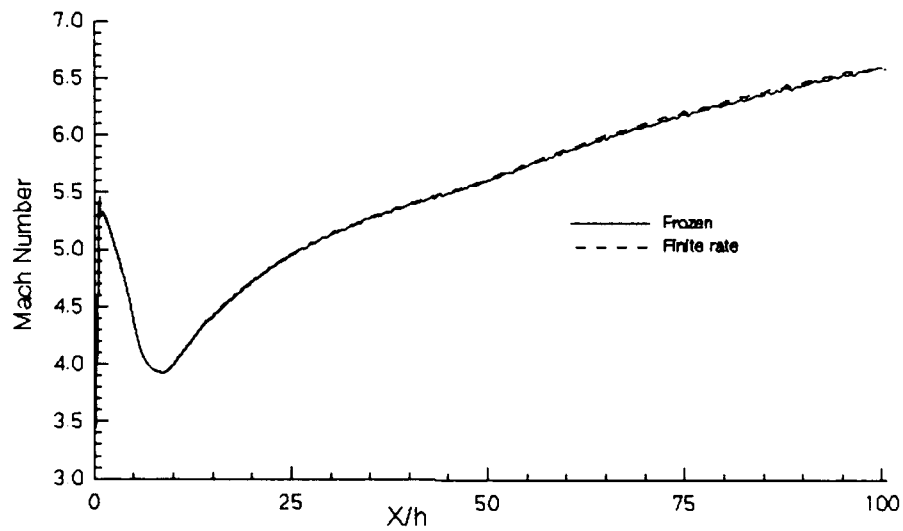


Figure A.12. Nozzle Wall Mach Numbers for Frozen and Finite Rate, Nonuniform Flow in the Combined Nozzle

## A.2 Isolated Nozzle vs. Combined Nozzle Plots

### A.2.1 Uniform, Finite Rate Flow

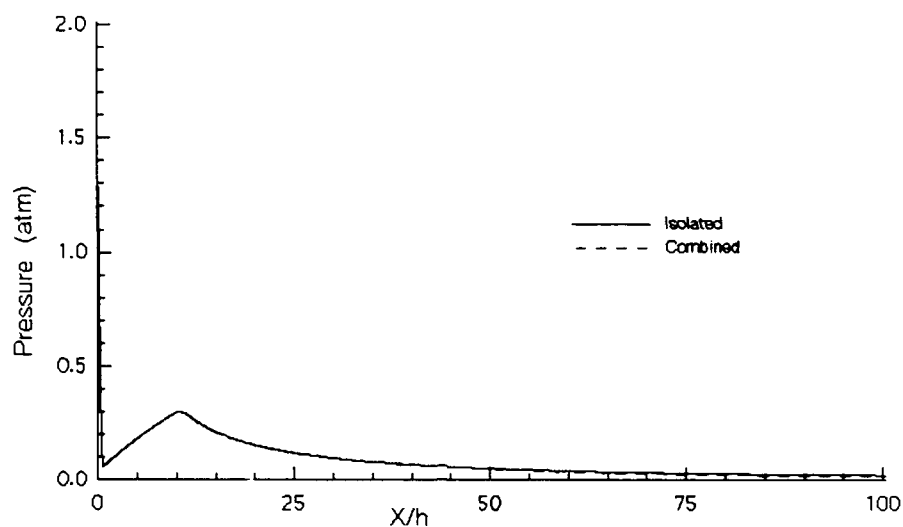


Figure A.13. Nozzle Wall Pressures for Uniform, Finite Rate Flow for the Isolated and Combined Nozzles

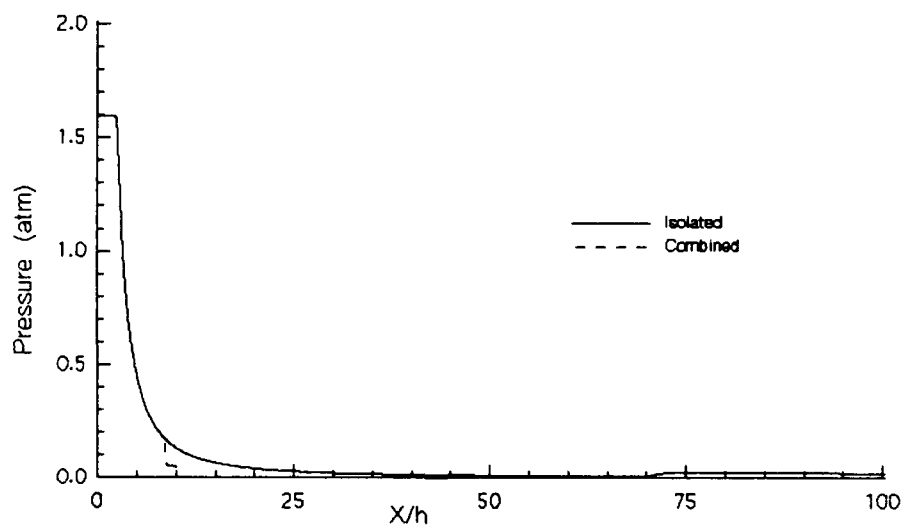


Figure A.14. Cowl Wall Pressures for Finite Rate, Uniform Flow for the Isolated and Combined Nozzles



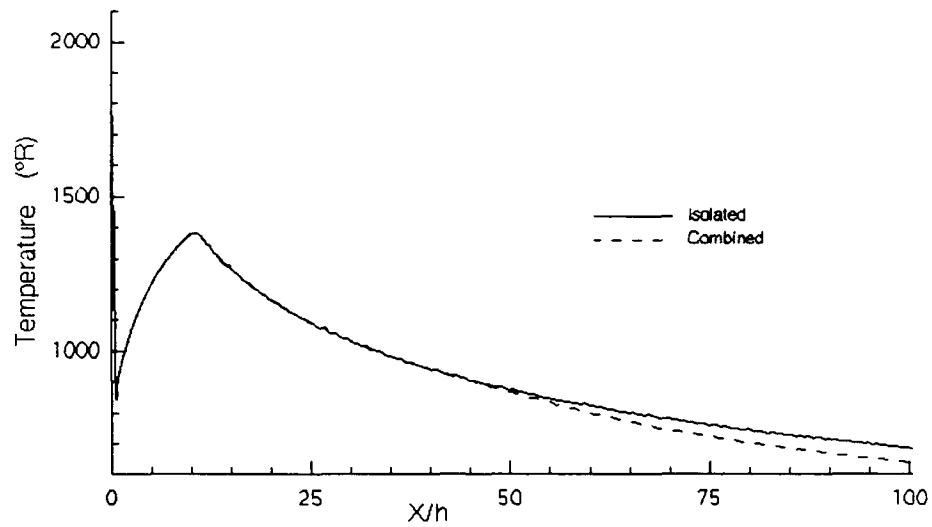


Figure A.15. Nozzle Wall Temperatures for Finite Rate, Uniform Flow for the Isolated and Combined Nozzles

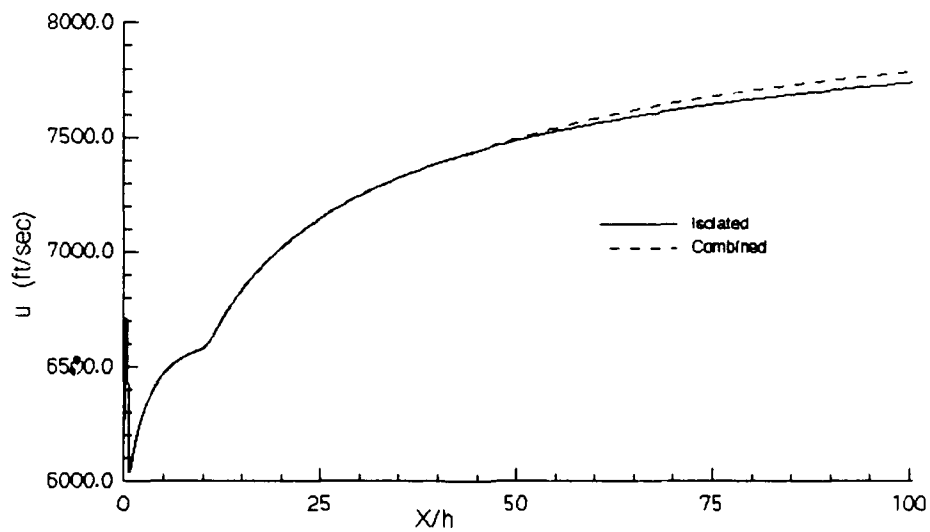


Figure A.16. Nozzle Wall X-Component Velocities for Finite Rate, Uniform Flow for the Isolated and Combined Nozzles

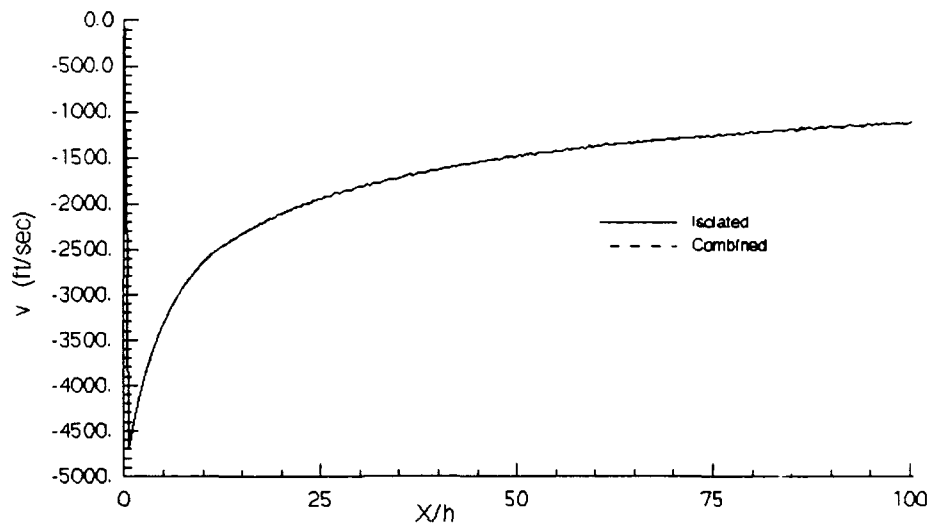


Figure A.17. Nozzle Wall Y-Component Velocities for Finite Rate, Uniform Flow for the Isolated and Combined Nozzles

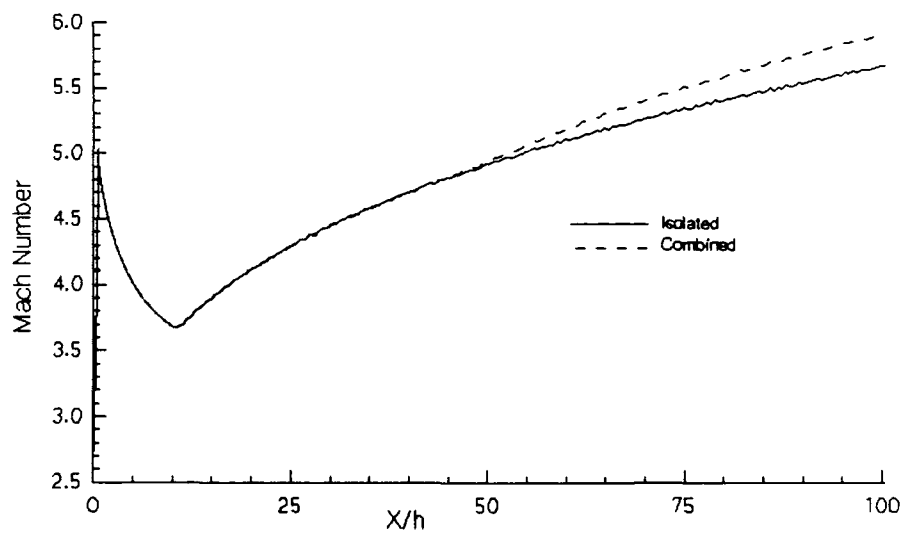


Figure A.18. Nozzle Wall Mach Numbers for Finite Rate, Uniform Flow for the Isolated and Combined Nozzles

A.2.2 Nonuniform, Finite Rate Flow

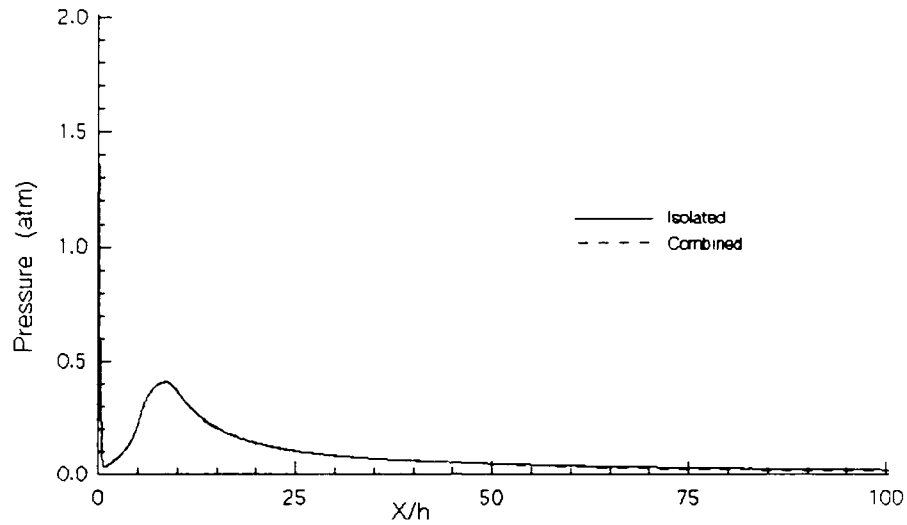


Figure A.19. Nozzle Wall Pressures for Finite Rate, Nonuniform Flow for the Isolated and Combined Nozzles

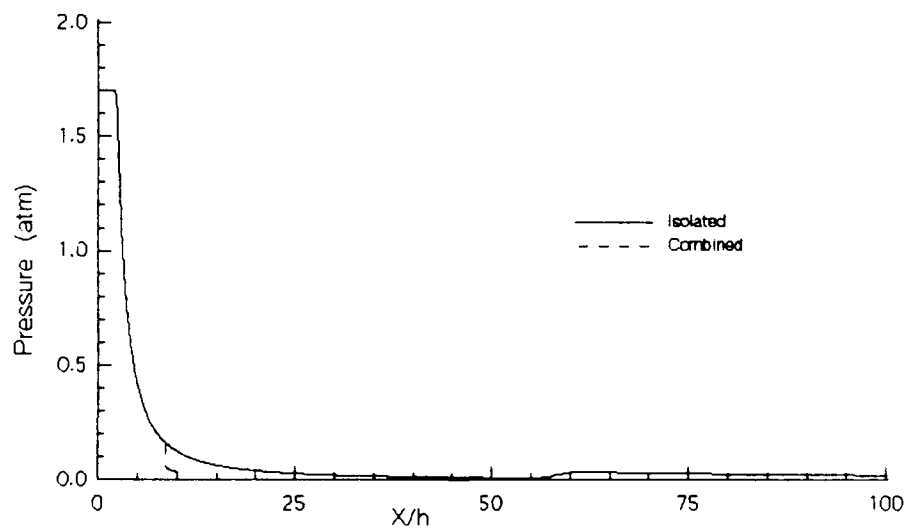


Figure A.20. Cowl Wall Pressures for Finite Rate, Nonuniform Flow for the Isolated and Combined Nozzles

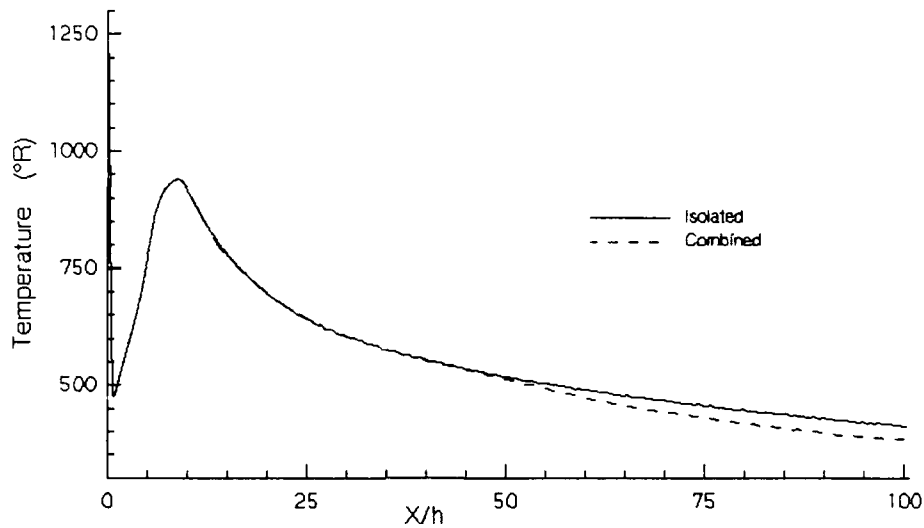


Figure A.21. Nozzle Wall Temperatures for Finite Rate, Nonuniform Flow for the Isolated and Combined Nozzles

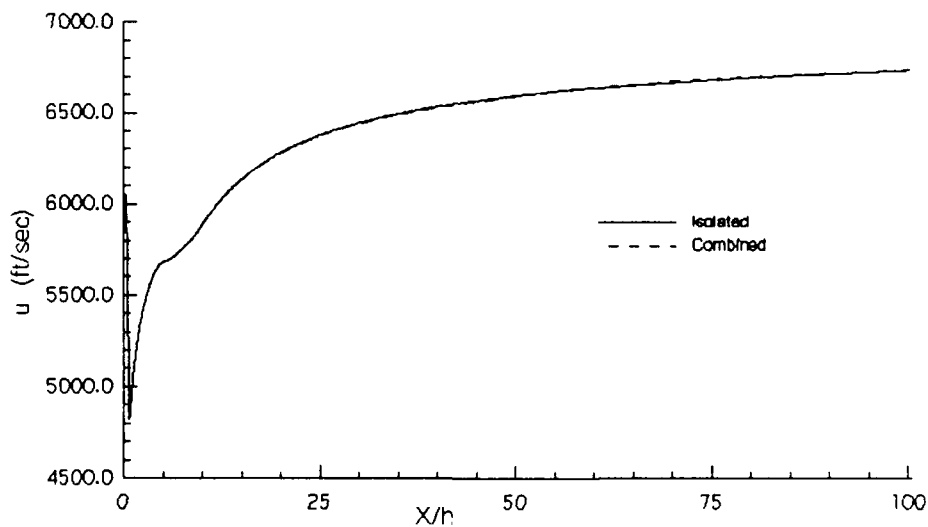


Figure A.22. Nozzle Wall X-Component Velocities for Finite Rate, Nonuniform Flow for the Isolated and Combined Nozzles

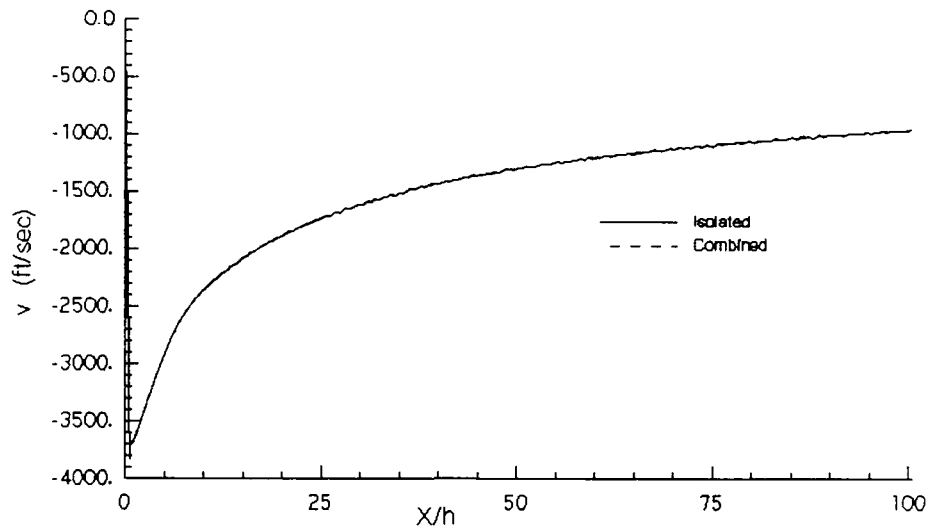


Figure A.23. Nozzle Wall Y-Component Velocities for Finite Rate, Nonuniform Flow for the Isolated and Combined Nozzles

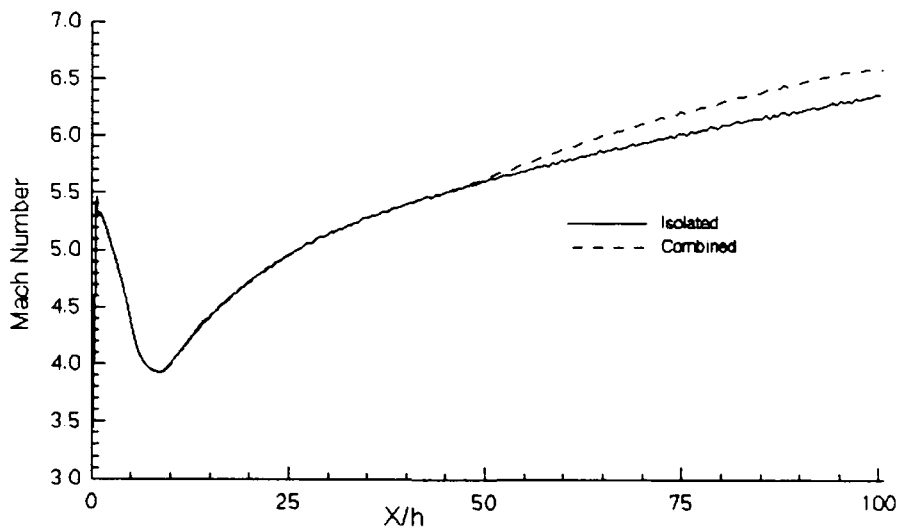


Figure A.24. Nozzle Wall Mach Numbers for Finite Rate, Nonuniform Flow for the Isolated and Combined Nozzles

### A.3 Uniform vs. Nonuniform Plots

#### A.3.1 Finite Rate, Isolated Nozzle

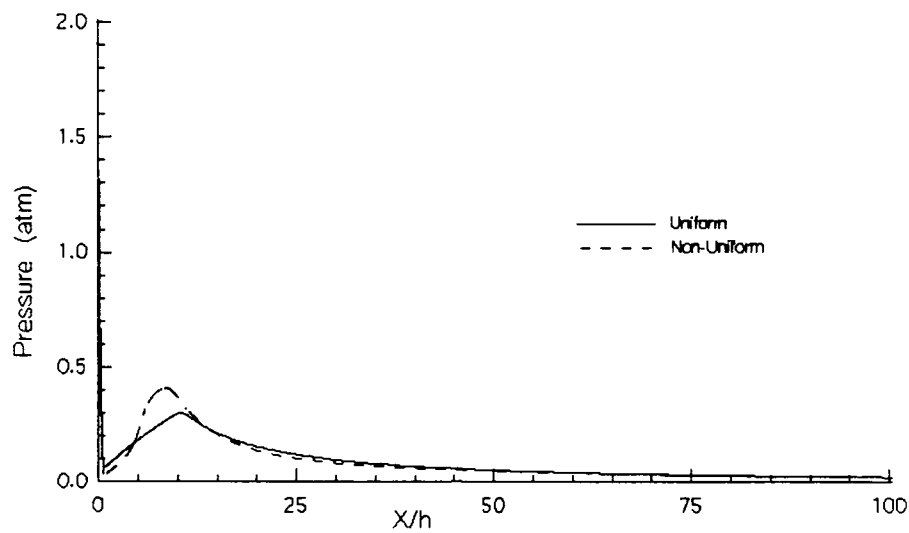


Figure A.25. Nozzle Wall Pressures for Uniform and Nonuniform Flow for the Finite Rate, Isolated Nozzle

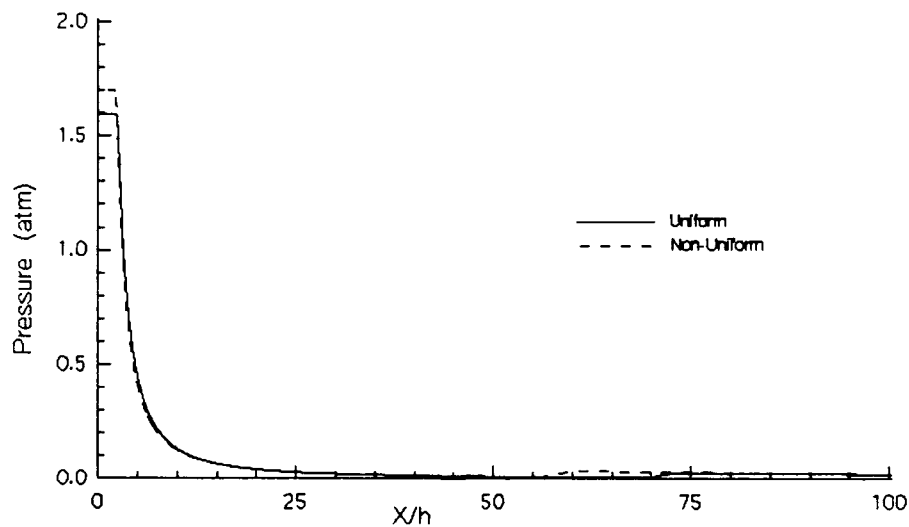


Figure A.26. Cowl Wall Pressures for Uniform and Nonuniform Flow for the Finite Rate, Isolated Nozzle

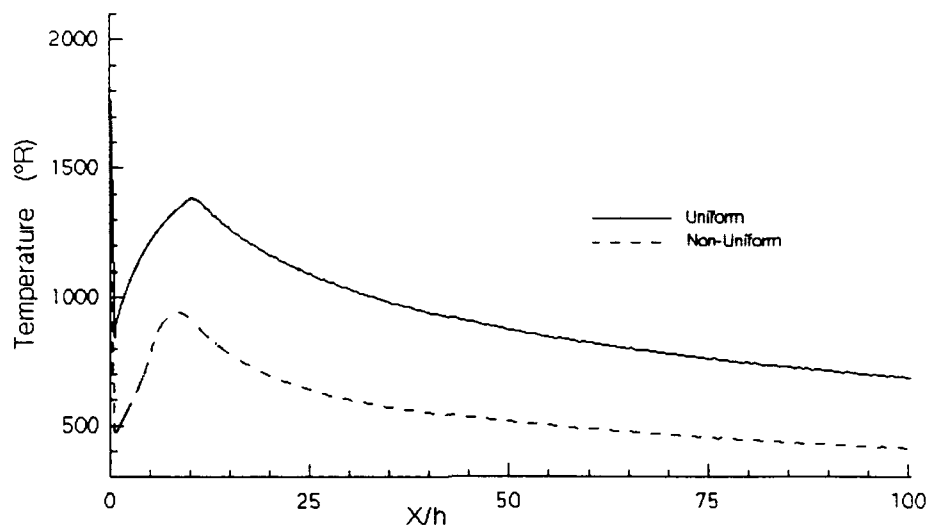


Figure A.27. Nozzle Wall Temperatures for Uniform and Nonuniform Flow for the Finite Rate Isolated Nozzle

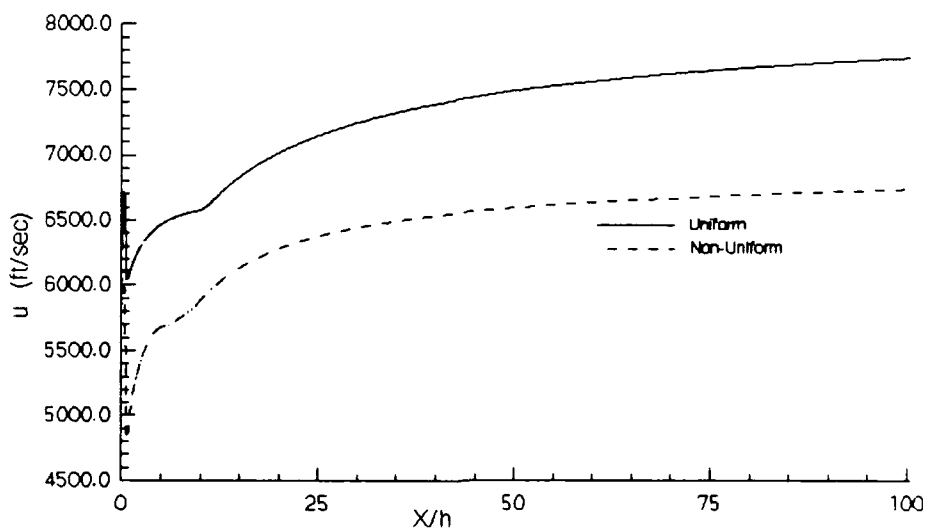


Figure A.28. Nozzle Wall X-Component Velocities for Uniform and Nonuniform Flow for the Finite Rate, Isolated Nozzle

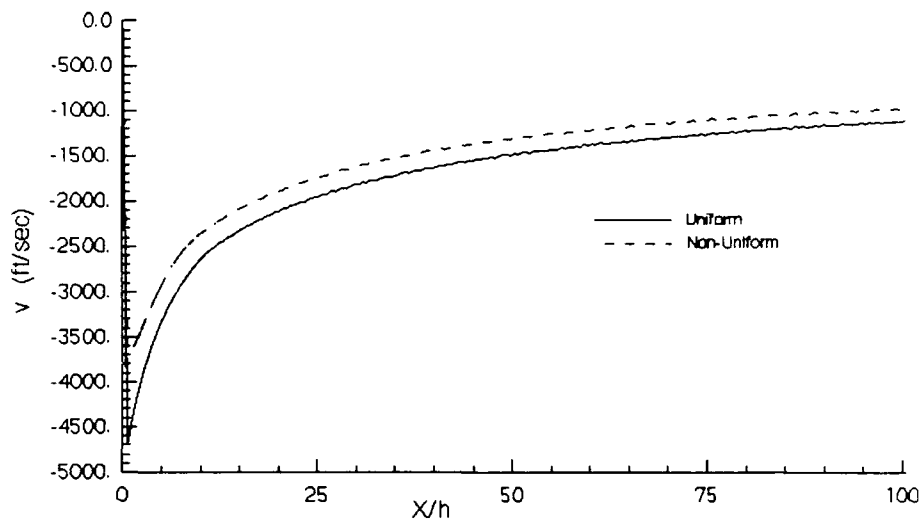


Figure A.29. Nozzle Wall Y-Component Velocities for Uniform and Nonuniform Flow for the Finite Rate, Isolated Nozzle

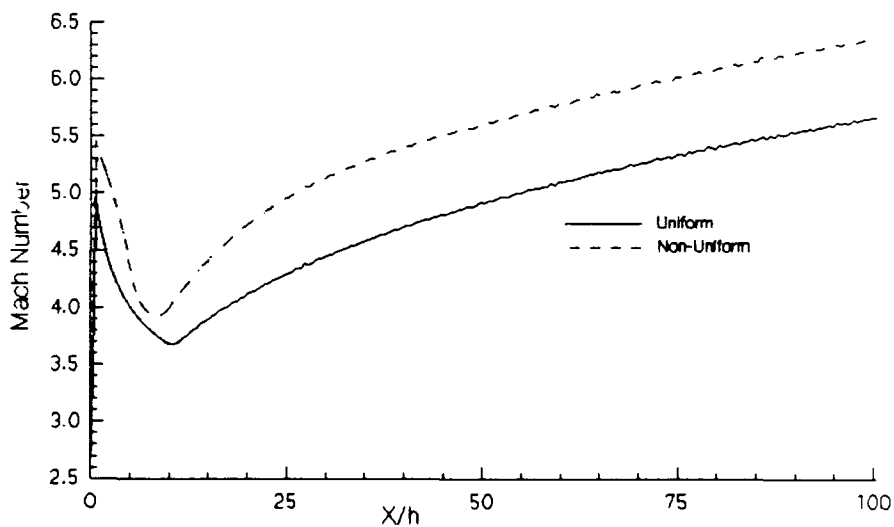


Figure A.30. Nozzle Wall Mach Numbers for Uniform and Nonuniform Flow for the Finite Rate, Isolated Nozzle



### A.3.2 Finite Rate, Combined Nozzle

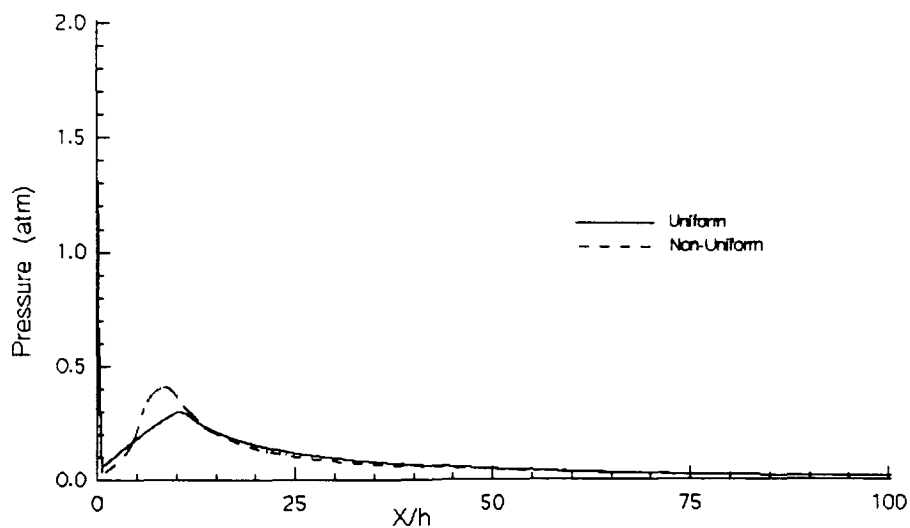


Figure A.31. Nozzle Wall Pressures for Uniform and Nonuniform Flow for the Finite Rate, Combined Nozzle

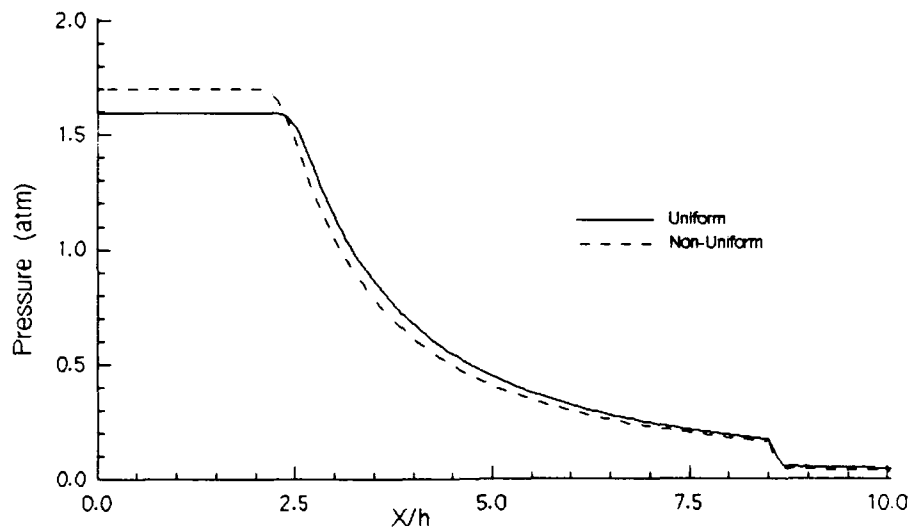


Figure A.32. Cowl Wall Pressures for Uniform and Nonuniform Flow for the Finite Rate, Combined Nozzle

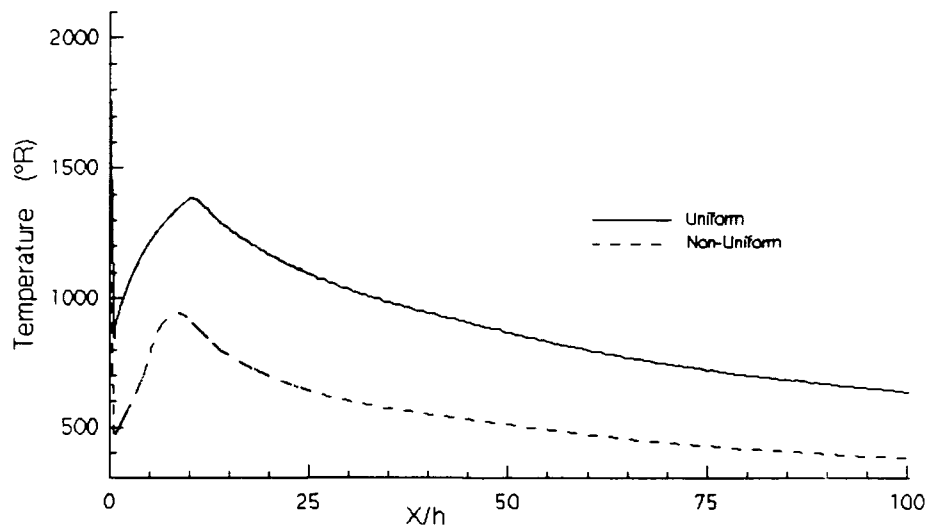


Figure A.33. Nozzle Wall Temperatures for Uniform and Nonuniform Flow for the Finite Rate, Combined Nozzle

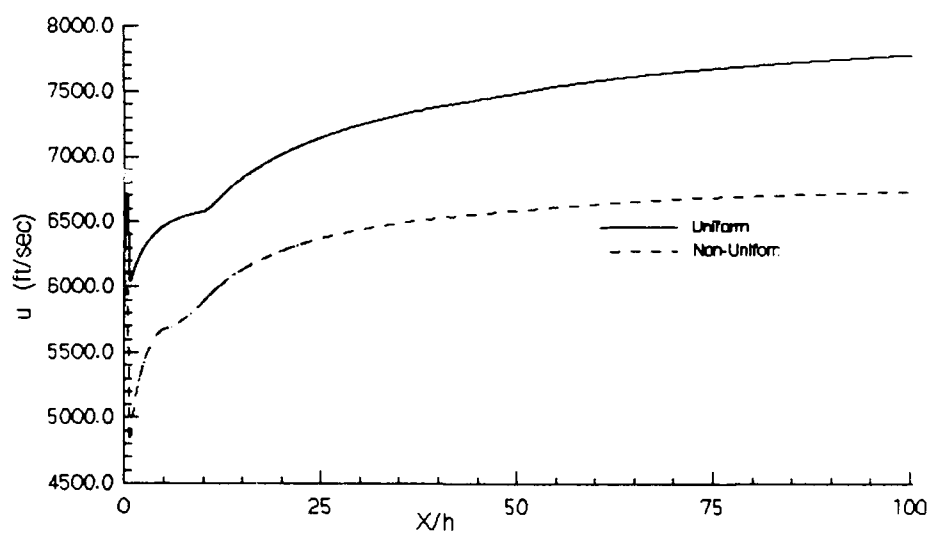


Figure A.34. Nozzle Wall X-Component Velocities for Uniform and Nonuniform Flow for the Finite Rate, Combined Nozzle

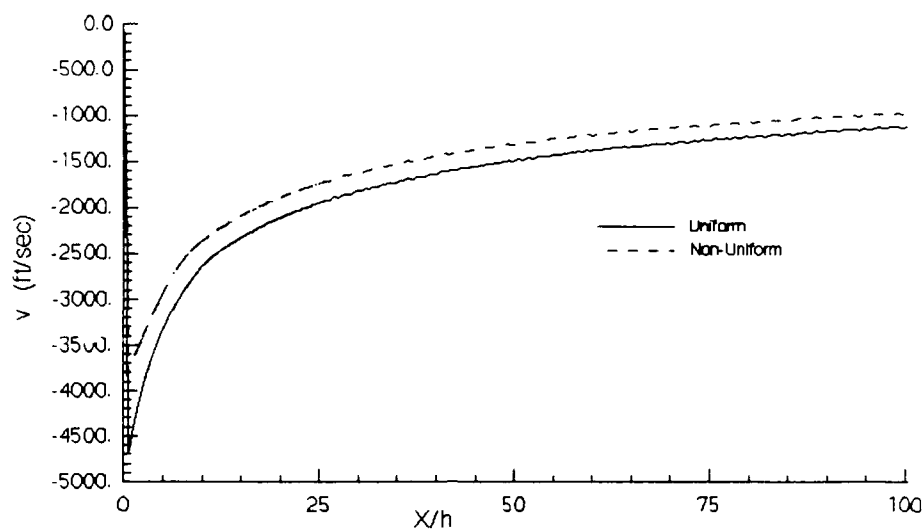


Figure A.35. Nozzle Wall Y-Component Velocities for Uniform and Nonuniform Flow for the Finite Rate, Combined Nozzle

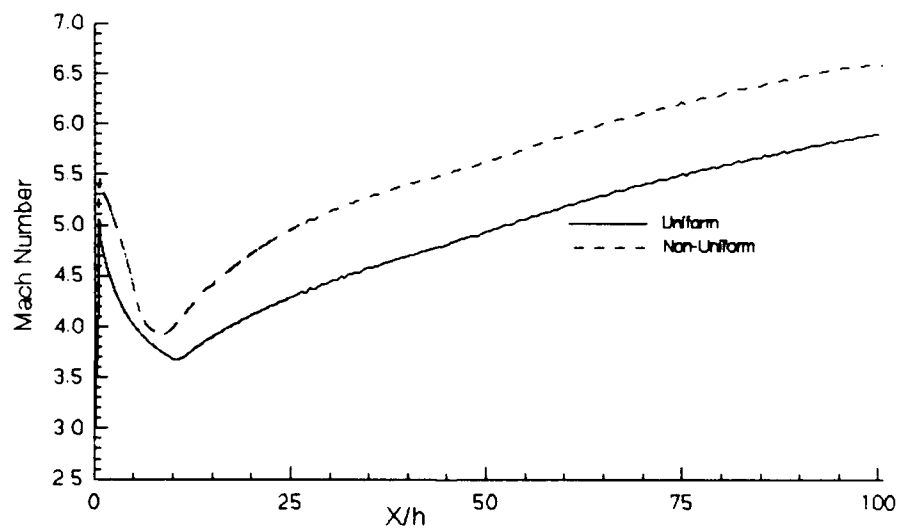


Figure A.36. Nozzle Wall Mach Numbers for Uniform and Nonuniform Flow for the Finite Rate, Combined Nozzle

#### A.4 Grid Resolution Plots

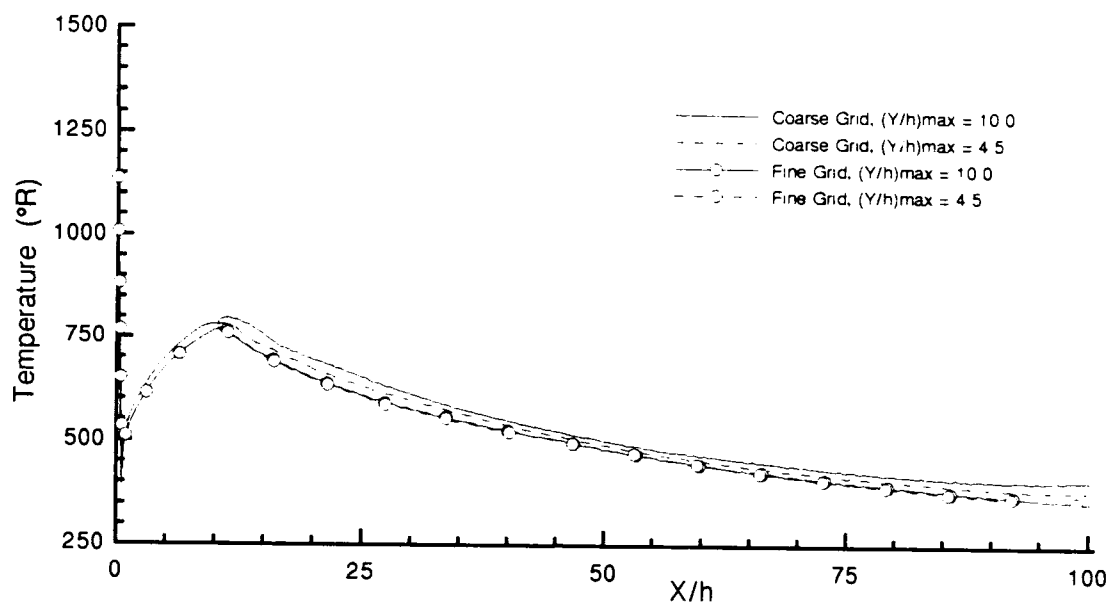


Figure A.37. Nozzle Wall Temperatures for Grid Changes for Uniform, Finite Rate Flow in the Combined Nozzle

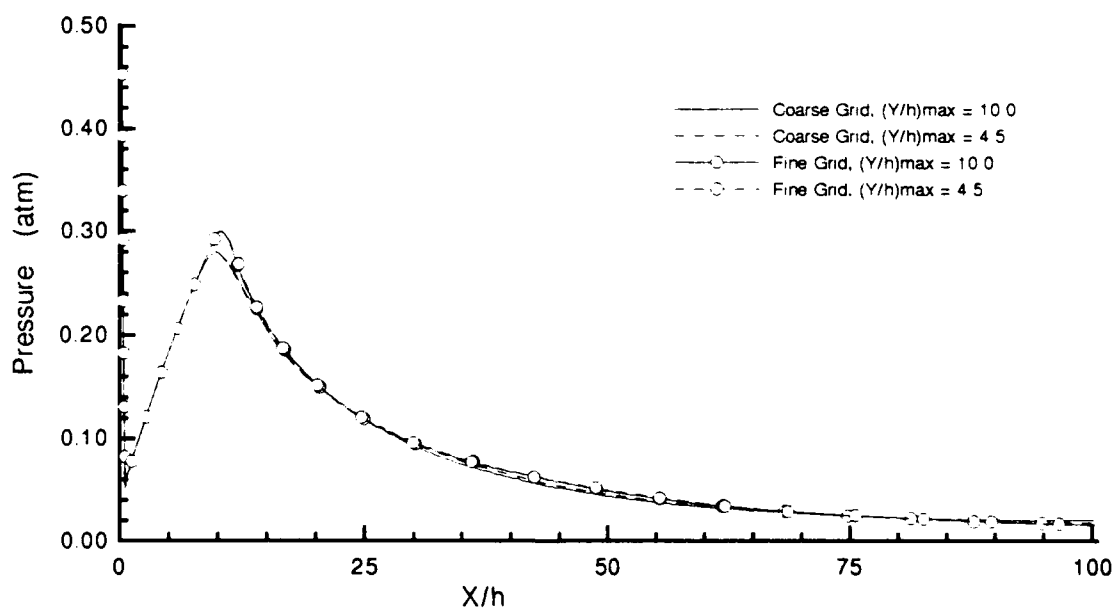


Figure A.38. Nozzle Wall Pressure for Grid Changes for Uniform, Finite Rate Flow in the Combined Nozzle

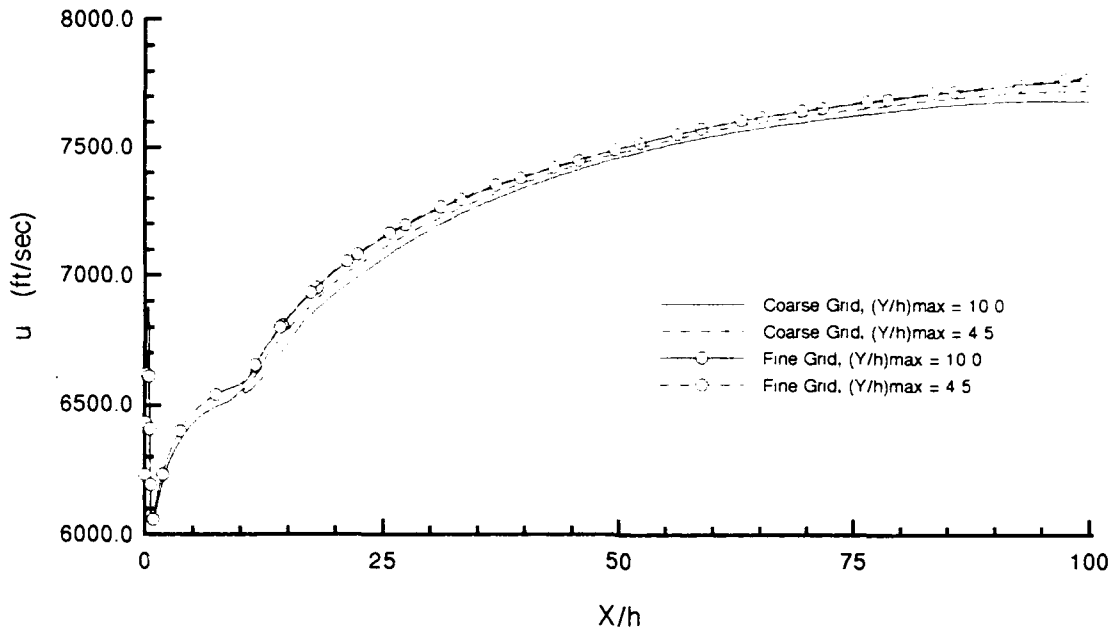


Figure A.39. Nozzle Wall X-Component Velocity for Grid Changes for Uniform, Finite Rate Flow in the Combined Nozzle

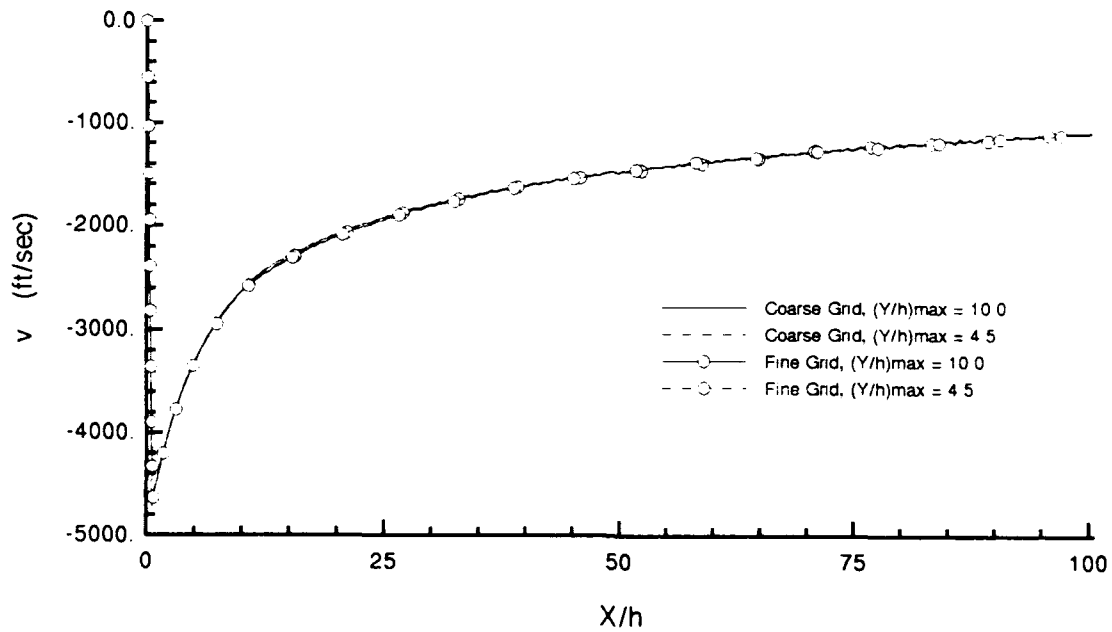


Figure A.40. Nozzle Wall Y-Component Velocity for Grid Changes for Uniform Flow, Finite Rate Flow in the Combined Nozzle

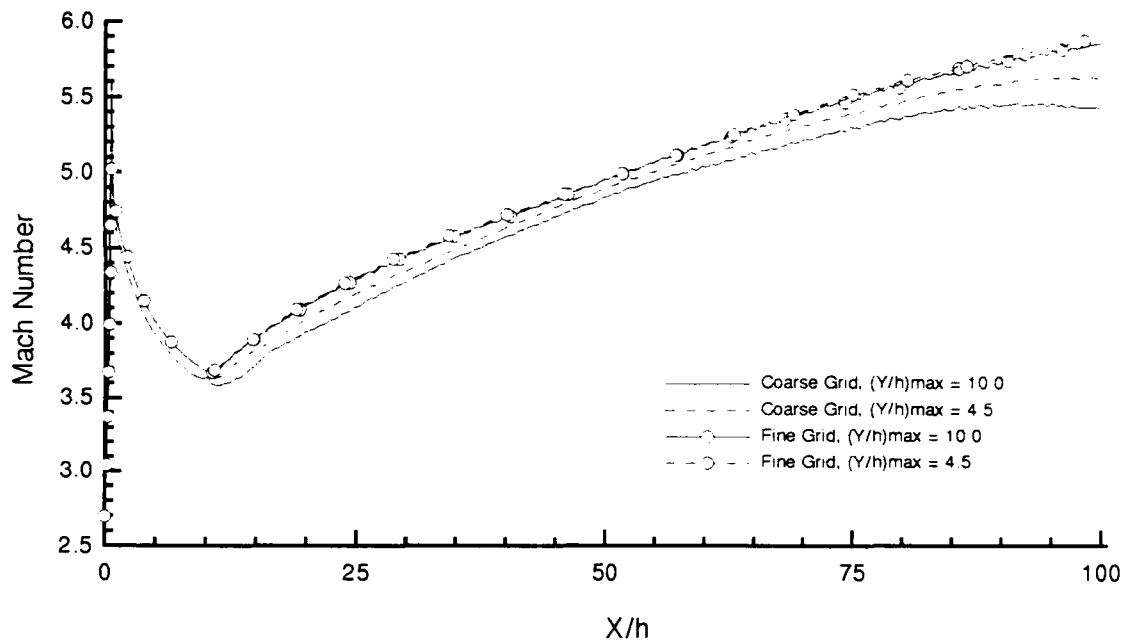


Figure A.41. Nozzle Wall Mach Number for Grid Changes for Uniform, Finite Rate Flow in the Combined Nozzle

#### A.4.2 Nonuniform Flow Plots

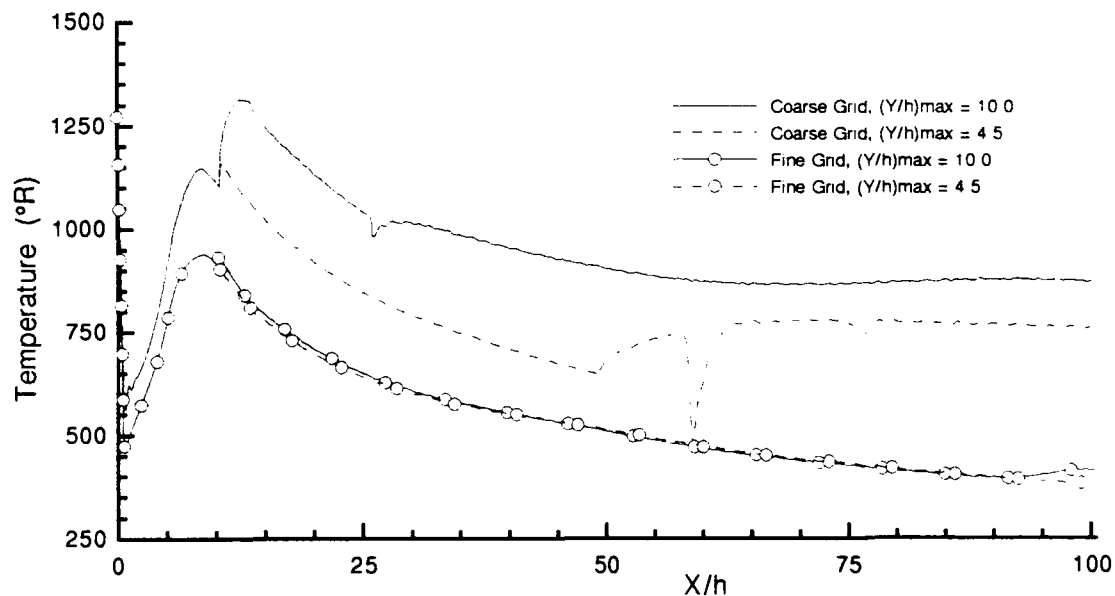


Figure A.42. Nozzle Wall Temperature for Grid Changes for Nonuniform, Finite Rate Flow in the Combined Nozzle

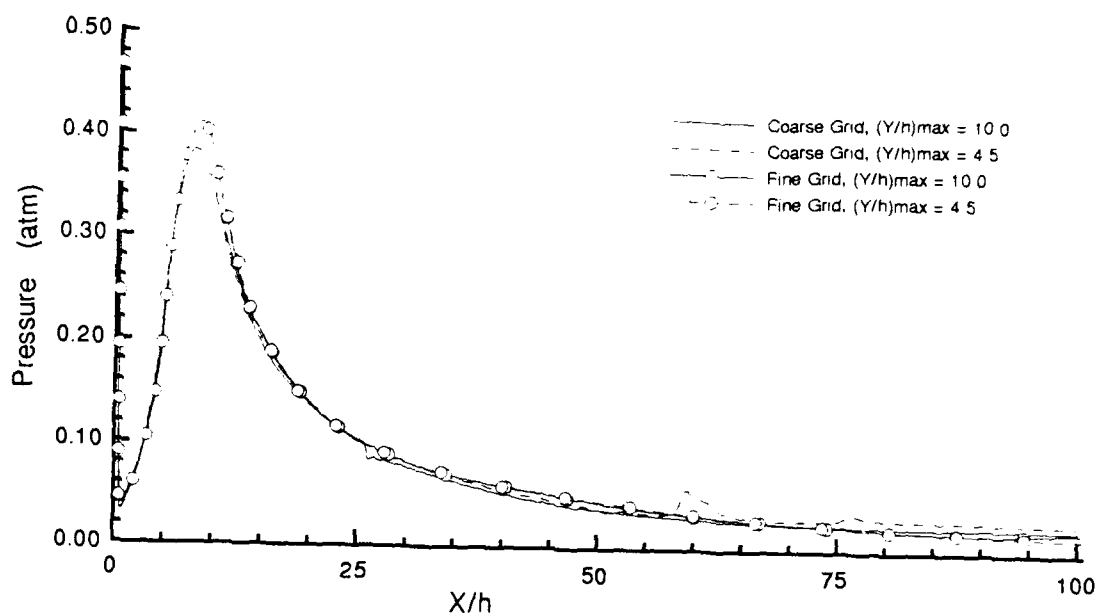


Figure A.43. Nozzle Wall Pressure for Grid Changes for Nonuniform, Finite Rate Flow in the Combined Nozzle

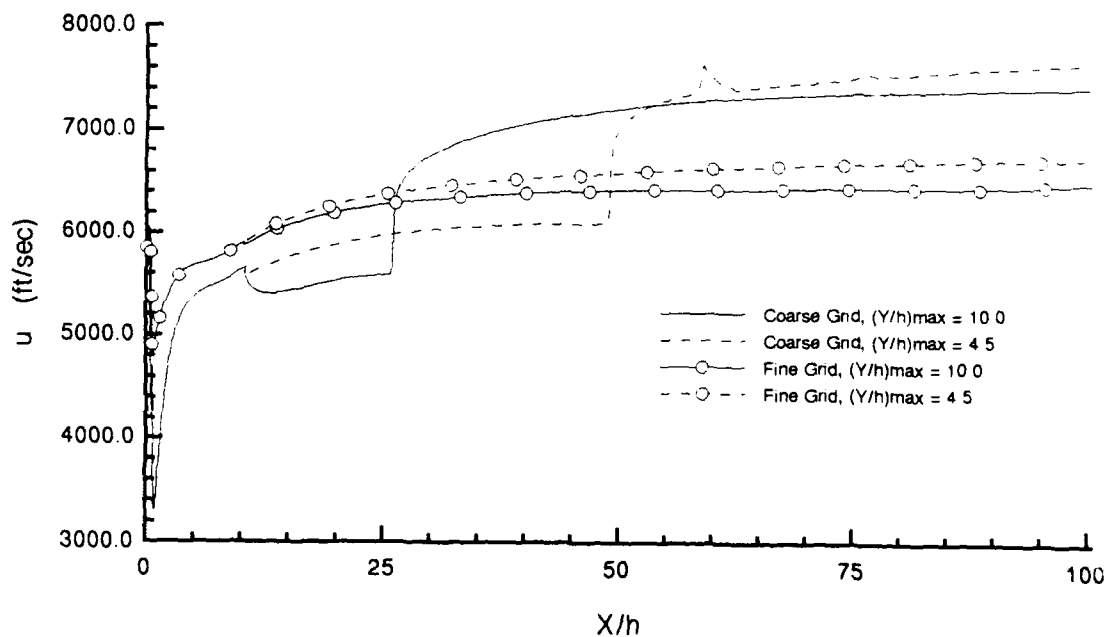


Figure A.44. Nozzle Wall X-Component Velocity for Grid Changes for Nonuniform, Finite Rate Flow in the Combined Nozzle

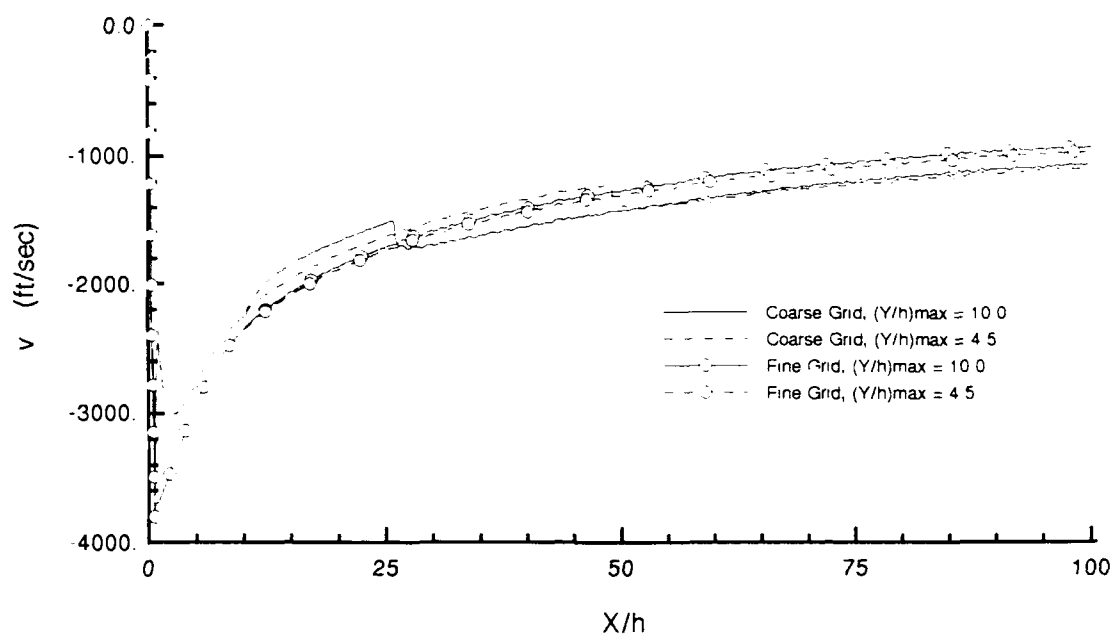


Figure A.45. Nozzle Wall Y-Component Velocity for Grid Changes for Nonuniform, Finite Rate Flow in the Combined Nozzle

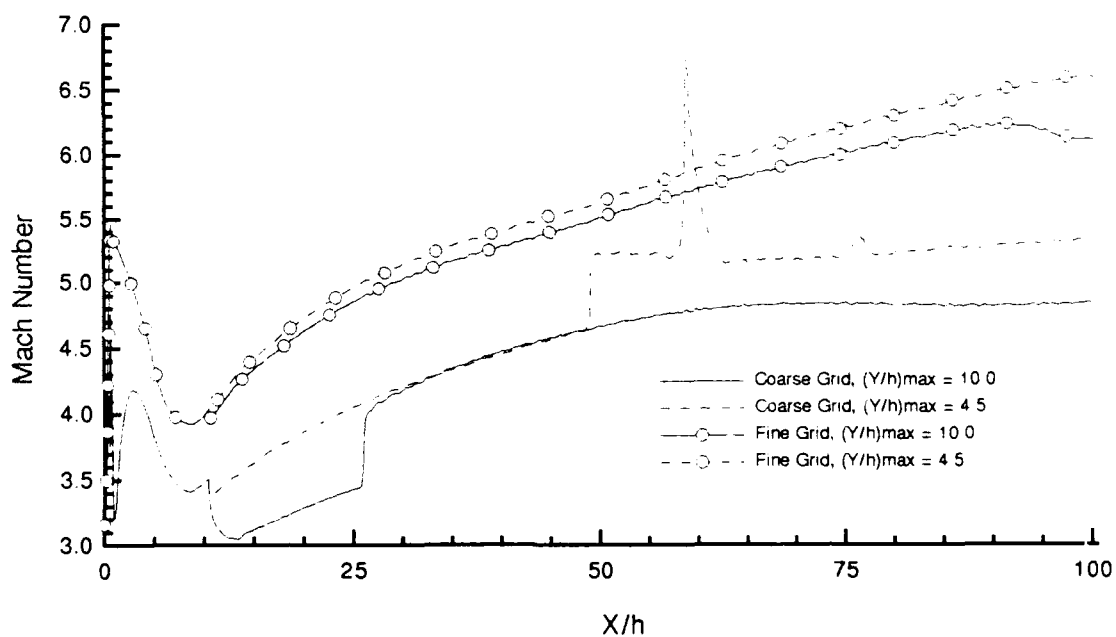


Figure A.46. Nozzle Wall Mach Number for Grid Changes for Nonuniform, Finite Rate Flow in the Combined Nozzle



## Appendix B. Contour Plots

### B.1 Isolated Nozzle Plots

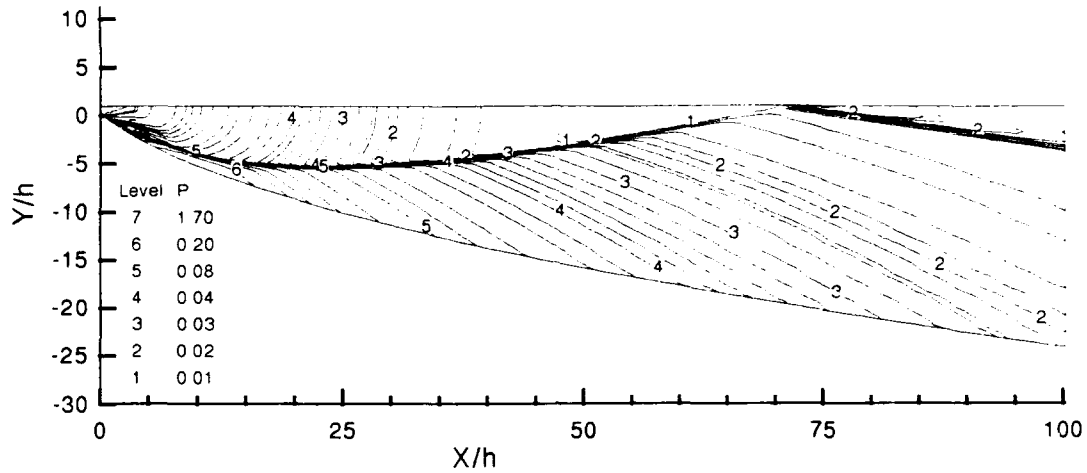


Figure B.1. Pressure Contour Plot (atm) for Uniform, Frozen Flow in an Isolated Nozzle

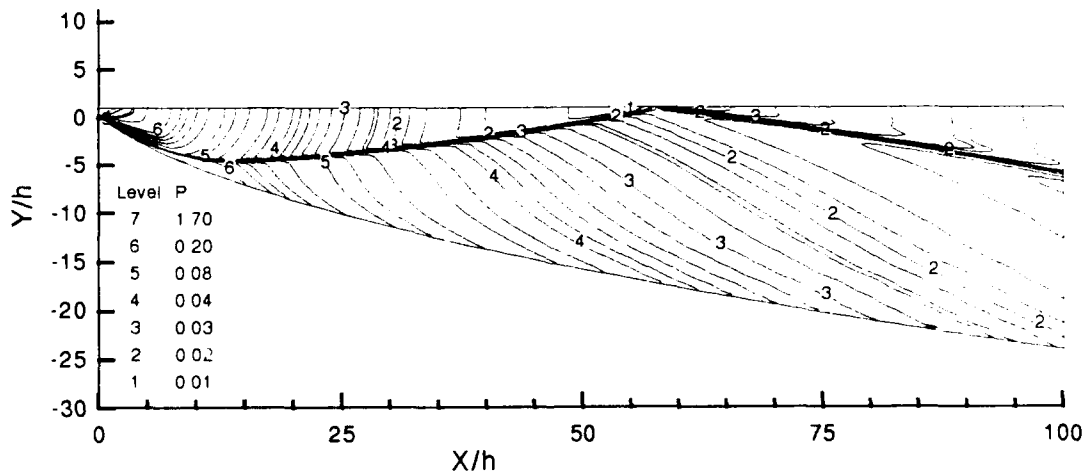


Figure B.2. Pressure Contour Plot (atm) for Non-Uniform, Frozen Flow in an Isolated Nozzle

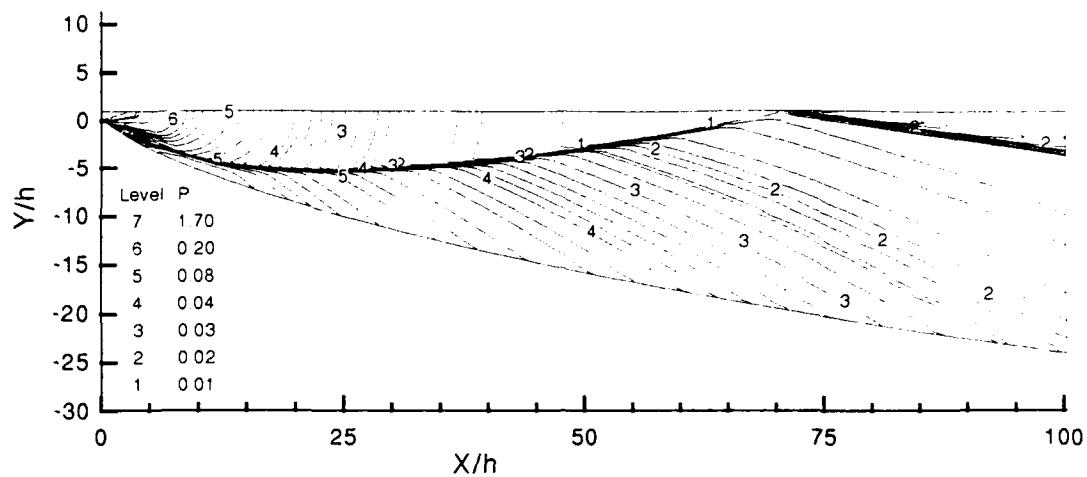


Figure B.3. Pressure Contour Plot (atm) for Uniform, Finite Rate Flow in an Isolated Nozzle

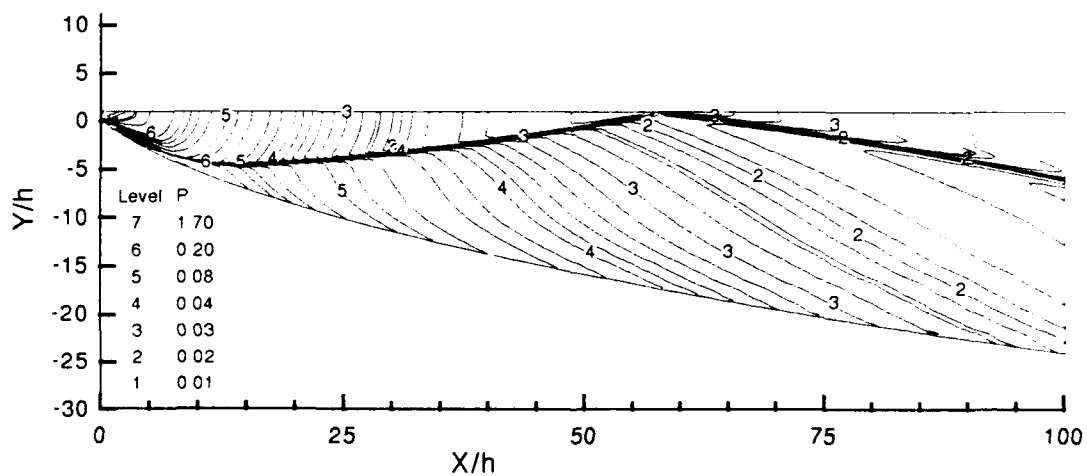


Figure B.4. Pressure Contour Plot (atm) for Non-Uniform, Finite Rate Flow in an Isolated Nozzle

## B.2 Combined Nozzle Plots

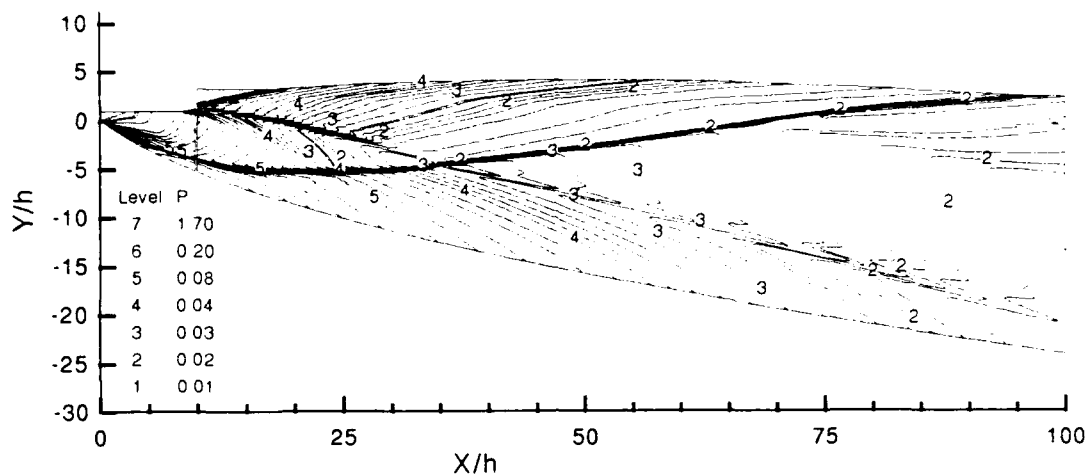


Figure B.5. Pressure Contour Plot (atm) for Uniform, Frozen Flow in a Combined Nozzle

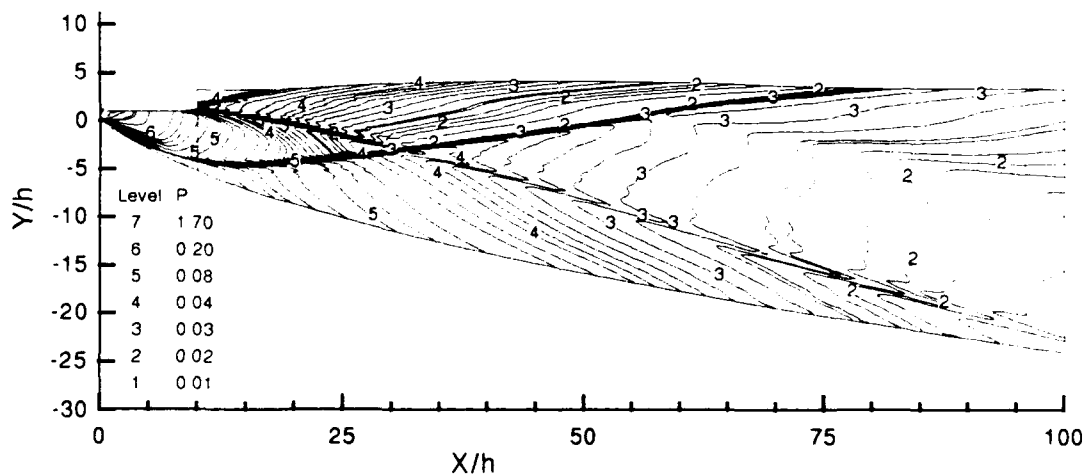


Figure B.6. Pressure Contour Plot (atm) for Non-Uniform, Frozen Flow in a Combined Nozzle

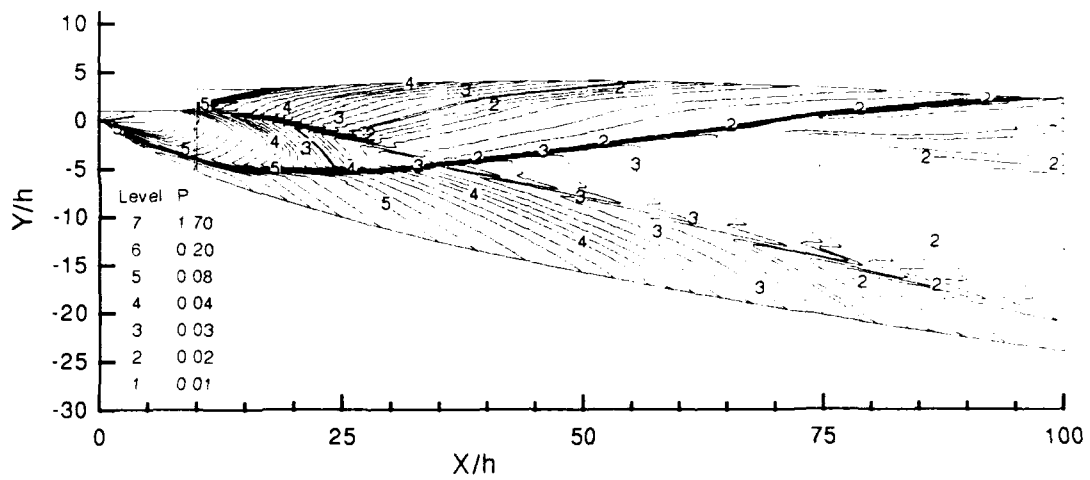


Figure B.7. Pressure Contour Plot (atm) for Uniform, Finite Rate Flow in a Combined Nozzle

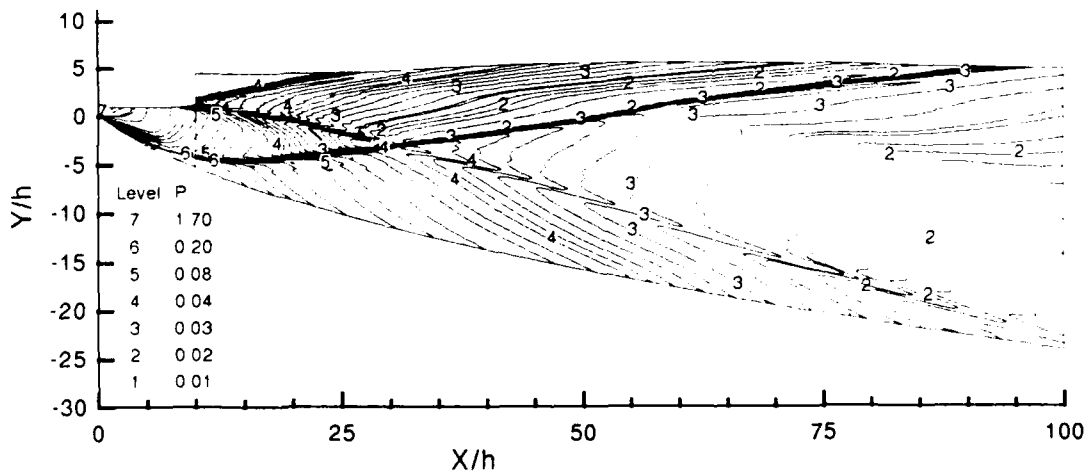


Figure B.8. Pressure Contour Plot (atm) for Non-Uniform, Finite Rate Flow in a Combined Nozzle

### Appendix C. Input Data

Table C.1 contains variables which changed during the study.

Table C.2 contains variables which did not vary during the study. Table

C.3 contains the nonuniform profile for the bottom half of the nozzle.

Table C.4 contains the nonuniform equilibrium chemical composition.

**Table C.1. SCHNOZ Variables which Change with Each Case and the Values Used for Each Case**

Variable	1	2	3	4	5	6	7	8
ICHEM	1	1	1	1	2	2	2	2
IREAD	2	2	101	101	2	2	101	101
IMAX	101	101	101	101	101	101	101	101
XMIBUC	100	10	100	10	100	10	100	10
IREADA	2	2	51	51	2	2	51	51
NWS2	NA	101	NA	101	NA	101	NA	101
INTBU	NA	0	NA	0	NA	0	NA	0
XBU	0.0	NA	0.0	NA	0.0	NA	0.0	NA
ABU	0.0	NA	0.0	NA	0.0	NA	0.0	NA
BBU	0.0	NA	0.0	NA	0.0	NA	0.0	NA
CBU	0.0	NA	0.0	NA	0.0	NA	0.0	NA
DBU	1.0	NA	1.0	NA	1.0	NA	1.0	NA
THJR2	NA	0.0	NA	0.0	NA	0.0	NA	0.0
THER2	NA	10.0	NA	10.	NA	10.	NA	10.
IREAD	NA	2	NA	51	NA	2	NA	51
IMAX	NA	51	NA	51	NA	51	NA	51

Table C.2. SCHNOZ Program Variables Which Remain Constant for This Study

IFLOW	0	IBL	0
IBU	0	IEXT	0
INT	1	IDOM	0
ICHNG	0	IPIT	0
NDOM	0	IVIS	1
ITURB	1	ICOMP	1
ILXY	0	IWDSN	0
IINTG	0	ISAHS	1
ISHL	1	IRCMB	0
XSTART	0.0	XSTOP	100.0
DXPRNT	10.0	XCHNG	$1 \times 10^6$
XPRNEW	10.0	RX	1.0
DRX	0.0	DXSHRI	0.3125
XCG	0.0	YCG	0.0
EPSIL	0.1	IPLTRD	0
IPLTAX	1	ICNTRP	1
IPRFBL	0	DCPRNT	5.0
WJET	0.0	GAMJ	0.0
PINF	0.003	EMINF	15.0
TINF	2491.8	RJ	0.083333
XMD	$1 \times 10^6$	THTINF	0.0
XK	1.0	XE	1.0
INTBL	0	NWS1	276
THJR1	0.0	THER1	-8.04
ISTCHM	1	TKINET	4000.0

Table C.3. Property Profiles for Nonuniform Inlet

Y (in)	M	Tt (R)	Pt (lbf/in <sup>2</sup> )	T (R)	u (ft/sec)
0.00	3.500	4000.0	2073.2	1272.4	5855.2
0.01	3.489	4079.2	2040.7	1302.9	5907.2
0.02	3.478	4156.8	2005.6	1333.7	5956.8
0.03	3.465	4232.8	1967.8	1364.8	6004.0
0.04	3.451	4307.2	1927.2	1396.3	6048.7
0.05	3.436	4380.0	1883.9	1428.3	6090.9
0.06	3.420	4451.2	1837.9	1460.8	6130.7
0.07	3.402	4520.8	1789.2	1494.0	6167.9
0.08	3.383	4588.8	1738.0	1528.0	6202.5
0.09	3.363	4655.2	1684.4	1562.7	6234.5
0.10	3.341	4720.0	1628.5	1598.4	6263.8
0.11	3.317	4783.2	1570.6	1635.1	6290.3
0.12	3.292	4844.8	1511.0	1672.8	6314.1
0.13	3.265	4904.8	1449.8	1711.8	6335.0
0.14	3.236	4963.2	1387.5	1752.0	6353.0
0.15	3.206	5020.0	1324.3	1793.6	6368.0
0.16	3.174	5075.2	1260.6	1836.7	6380.0
0.17	3.141	5128.8	1196.7	1881.2	6388.9
0.18	3.106	5180.8	1133.1	1927.4	6394.6
0.19	3.069	5231.2	1070.1	1975.2	6397.1
0.20	3.031	5280.0	1008.1	2024.8	6396.4
0.21	2.991	5327.2	947.4	2076.1	6392.4
0.22	2.951	5372.8	888.2	2129.1	6385.1
0.23	2.908	5416.8	831.0	2183.9	6374.5
0.24	2.865	5459.2	776.0	2240.4	6360.5
0.25	2.821	5500.0	723.4	2298.6	6343.3
0.26	2.776	5539.2	673.3	2358.5	6322.8
0.27	2.730	5576.8	626.0	2419.8	6299.2
0.28	2.684	5612.8	581.4	2482.5	6272.5
0.29	2.638	5647.2	539.7	2546.4	6242.9
0.30	2.591	5680.0	500.9	2611.2	6210.6
0.31	2.545	5711.2	464.9	2676.8	6175.7
0.32	2.499	5740.8	431.8	2742.7	6138.6
0.33	2.454	5768.8	401.4	2808.8	6099.5
0.34	2.410	5795.2	373.6	2874.6	6058.8
0.35	2.366	5820.0	348.4	2939.7	6016.8
0.36	2.324	5843.2	325.6	3003.7	5974.0
0.37	2.284	5864.8	305.0	3066.1	5930.9
0.38	2.245	5884.8	286.7	3126.5	5888.0
0.39	2.209	5903.2	270.3	3184.4	5845.7
0.40	2.175	5920.0	255.9	3239.2	5804.7
0.41	2.143	5935.2	243.2	3290.6	5765.4
0.42	2.114	5948.8	232.2	3338.0	5728.4
0.43	2.088	5960.8	222.8	3381.0	5694.3
0.44	2.065	5971.2	214.8	3419.1	5663.6
0.45	2.046	5980.0	208.1	3452.1	5636.7
0.46	2.029	5987.2	202.8	3479.5	5614.1
0.47	2.017	5992.8	198.7	3501.2	5596.1
0.48	2.007	5996.8	195.8	3516.8	5583.0
0.49	2.002	5999.2	194.1	3526.3	5575.1
0.50	2.000	6000.0	193.6	3529.4	5572.5

Table C.4. Equilibrium Chemical Composition for Nonuniform Entrance Profile

Y/h	H	H <sub>2</sub>	H <sub>2</sub> O	N <sub>2</sub>	O	OH	O <sub>2</sub>
0.00	0.00000	0.00000	0.34721	0.65279	0.00000	0.00000	0.00000
0.01	0.00000	0.00000	0.34721	0.65279	0.00000	0.00000	0.00000
0.02	0.00000	0.00000	0.34721	0.65279	0.00000	0.00000	0.00000
0.03	0.00000	0.00000	0.34721	0.65279	0.00000	0.00000	0.00000
0.04	0.00000	0.00000	0.34721	0.65279	0.00000	0.00000	0.00000
0.05	0.00000	0.00000	0.34721	0.65279	0.00000	0.00000	0.00000
0.06	0.00000	0.00000	0.34721	0.65279	0.00000	0.00000	0.00000
0.07	0.00000	0.00000	0.34721	0.65279	0.00000	0.00000	0.00000
0.08	0.00000	0.00000	0.34721	0.65279	0.00000	0.00000	0.00000
0.09	0.00000	0.00000	0.34721	0.65279	0.00000	0.00000	0.00000
0.10	0.00000	0.00000	0.34721	0.65279	0.00000	0.00000	0.00000
0.11	0.00000	0.00000	0.34721	0.65279	0.00000	0.00000	0.00000
0.12	0.00000	0.00000	0.34721	0.65279	0.00000	0.00000	0.00000
0.13	0.00000	0.00000	0.34721	0.65279	0.00000	0.00000	0.00000
0.14	0.00000	0.00000	0.34721	0.65279	0.00000	0.00000	0.00000
0.15	0.00000	0.00000	0.34721	0.65279	0.00000	0.00000	0.00000
0.16	0.00000	0.00000	0.34721	0.65279	0.00000	0.00000	0.00000
0.17	0.00000	0.00000	0.34721	0.65279	0.00000	0.00000	0.00000
0.18	0.00000	0.00000	0.34721	0.65279	0.00000	0.00000	0.00000
0.19	0.00000	0.00000	0.34721	0.65279	0.00000	0.00000	0.00000
0.20	0.00000	0.00000	0.34721	0.65279	0.00000	0.00000	0.00000
0.21	0.00000	0.00000	0.34721	0.65279	0.00000	0.00000	0.00000
0.22	0.00000	0.00000	0.34721	0.65279	0.00000	0.00000	0.00000
0.23	0.00000	0.00000	0.34721	0.65279	0.00000	0.00000	0.00000
0.24	0.00000	0.00000	0.34720	0.65279	0.00000	0.00000	0.00000
0.25	0.00000	0.00001	0.34720	0.65279	0.00000	0.00000	0.00000
0.26	0.00000	0.00001	0.34720	0.65278	0.00000	0.00000	0.00001
0.27	0.00000	0.00002	0.34719	0.65278	0.00000	0.00000	0.00001
0.28	0.00000	0.00003	0.34718	0.65278	0.00000	0.00000	0.00001
0.29	0.00000	0.00004	0.34717	0.65278	0.00000	0.00001	0.00002
0.30	0.00000	0.00005	0.34715	0.65277	0.00000	0.00001	0.00002
0.31	0.00000	0.00007	0.34712	0.65276	0.00000	0.00001	0.00003
0.32	0.00000	0.00010	0.34708	0.65275	0.00000	0.00002	0.00005
0.33	0.00000	0.00014	0.34703	0.65274	0.00000	0.00003	0.00006
0.34	0.00000	0.00018	0.34697	0.65272	0.00000	0.00004	0.00008
0.35	0.00000	0.00025	0.34689	0.65270	0.00000	0.00006	0.00011
0.36	0.00000	0.00032	0.34679	0.65267	0.00000	0.00008	0.00014
0.37	0.00000	0.00041	0.34667	0.65264	0.00000	0.00011	0.00018
0.38	0.00000	0.00052	0.34652	0.65260	0.00000	0.00014	0.00022
0.39	0.00001	0.00064	0.34635	0.65255	0.00000	0.00018	0.00028
0.40	0.00001	0.00077	0.34616	0.65249	0.00000	0.00023	0.00033
0.41	0.00001	0.00092	0.34595	0.65243	0.00000	0.00028	0.00039
0.42	0.00001	0.00108	0.34573	0.65237	0.00000	0.00034	0.00046
0.43	0.00002	0.00124	0.34550	0.65231	0.00000	0.00040	0.00053
0.44	0.00002	0.00140	0.34527	0.65224	0.00001	0.00047	0.00059
0.45	0.00003	0.00156	0.34505	0.65218	0.00001	0.00053	0.00065
0.46	0.00003	0.00169	0.34486	0.65212	0.00001	0.00058	0.00071
0.47	0.00004	0.00181	0.34469	0.65208	0.00001	0.00063	0.00075
0.48	0.00004	0.00189	0.34457	0.65204	0.00001	0.00067	0.00079
0.49	0.00004	0.00194	0.34449	0.65202	0.00001	0.00069	0.00081
0.50	0.00004	0.00196	0.34446	0.65201	0.00001	0.00070	0.00081



REPORT DOCUMENTATION PAGE			Form Approved OMB No. 0704-0188	
Public reporting burden for this collection of information is estimated to average 1 hour per response, including the time for reviewing instructions, searching existing data sources, gathering and maintaining the data needed, and completing and reviewing the collection of information. Send comments regarding this burden estimate or any other aspect of this collection of information, including suggestions for reducing this burden, to Washington Headquarters Services, Directorate for Information Operations and Reports, 1215 Jefferson Davis Highway, Suite 1204, Arlington, VA 22202-4302, and to the Office of Management and Budget, Paperwork Project (0704-0188), Washington, DC 20503.				
1. AGENCY USE ONLY (leave blank)	2. REPORT DATE December 1991	3. REPORT TYPE AND DATES COVERED Master's Thesis		
4. TITLE AND SUBTITLE  EFFECT OF NONUNIFORM ENTRANCE FLOW PROFILE ON HYPERSONIC PITCHING MOMENT			5. FUNDING NUMBERS	
6. AUTHOR(S)  Snelling, Sandra L., Captain, USAF				
7. PERFORMING ORGANIZATION NAME(S) AND ADDRESS(ES)  Air Force Institute of Technology, WPAFB OH 45433-6583			8. PERFORMING ORGANIZATION REPORT NUMBER  AFIT/GA/ENY/91D-13	
9. SPONSORING MONITORING AGENCY NAME(S) AND ADDRESS(ES)  Mr. Donald Stava WL/FIMM WPAFB, OH 45433			10. SPONSORING MONITORING AGENCY REPORT NUMBER	
11. SUPPLEMENTARY NOTES				
12a. DISTRIBUTION AVAILABILITY STATEMENT  Approved for public release; distribution unlimited			12b. DISTRIBUTION CODE	
13. ABSTRACT (Maximum 200 words) The Scramjet Hypersonic Nozzle (SCHNOZ) parabolized Navier-Stokes computer code was used to model turbulent, chemically reacting flow present in a hypersonic nozzle. Two nozzle configurations were considered, an isolated nozzle (no external flow) and a nozzle with a finite length cowl. A single nonuniform entrance flow profile was generated and an equivalent uniform flow profile calculated for input into the nozzle code. Uniform and nonuniform cases for each nozzle were run using both frozen and finite rate chemistry. An increased grid resolution in the computer code was necessary to eliminate numerically induced anomalies in the results of the nonuniform cases for both nozzle configurations. Comparisons between the finite rate and frozen flow cases showed that chemistry was essentially frozen for the finite rate cases, indicating that for the nozzle conditions and geometry used in this study, the extra computational time spent on finite rate kinetics was unnecessary. The effects of the nonuniform flowfield used in this study included an increase in the overall vehicle thrust and a decrease in the overall vehicle moment.				
14. SUBJECT TERMS Hypersonic Nozzle, Scramjet, NASP, Nozzle Performance, Nonuniform Flow, Hypersonic Propulsion			15. NUMBER OF PAGES 106	
			16. PRICE CODE	
17. SECURITY CLASSIFICATION OF REPORT Unclassified	18. SECURITY CLASSIFICATION OF THIS PAGE Unclassified	19. SECURITY CLASSIFICATION OF ABSTRACT Unclassified	20. LIMITATION OF ABSTRACT  UL	